The Pennsylvania State University

The J. Jeffrey and Ann Marie Fox Graduate School

COMPOSITIONALLY COMPLEX PEROVSKITE OXIDES: DIELECTRIC, FERROELECTRIC, ELECTROCALORIC, AND ENERGY STORAGE PROPERTIES

A Dissertation in

Materials Science and Engineering

by

Yeongwoo Son

Submitted in Partial Fulfillment
of the Requirements
for the Degree of

Doctor of Philosophy

December 2024

The dissertation of Yeongwoo Son was reviewed and approved by the following:

Susan Trolier-McKinstry
Evan Pugh University Professor and Flaschen Professor of Ceramic Science and Engineering and Electrical Engineering
Dissertation Advisor
Chair of Committee

Clive A. Randall
Evan Pugh University Professor of Materials Science and Engineering

Jon-Paul Maria
Professor of Materials Science and Engineering

Qiming Zhang
Distinguished Professor of Electrical Engineering

John C. Mauro
Graduate Program Head, Dorothy Pate Enright Professor of Materials Science and Engineering

ABSTRACT

This thesis investigates the structural, dielectric, ferroelectric, electrocaloric, and energy storage properties of high entropy-like formulations. Eight different high entropy perovskite oxides (HEPO) were explored in terms of synthesizability, phase development, and structural characteristics in both powders and thin films. Five different compositions with compositional disorder on the B-site of the perovskite structure; $Pb(Hf_{0.2}Zr_{0.2}Ti_{0.2}Nb_{0.2}M_{0.2})O_3$ (M=Al, Cr, Fe, Mn, Sc) and three different compositions with compositional disorder on the A-site of the perovskite: $(Bi_{0.2}Ba_{0.2}Sr_{0.2}Ca_{0.2}Na_{0.2})TiO_3$, $(Bi_{0.2}Ba_{0.2}Sr_{0.2}Ca_{0.2}K_{0.2})TiO_3$, $(Bi_{0.2}Ba_{0.2}Sr_{0.2}Na_{0.2}Pb_{0.2})TiO_3$. It was found that the Goldschmidt tolerance factor was an effective predictor of phase development. Metastable HEPO phases were accessible experimentally by pulsed laser deposition (PLD).

It was shown that relative dielectric permittivity of HEPO films ranged from 180 to 2000 at frequencies from 100 Hz to 100 kHz at room temperature, depending on the composition. It was found that some of HEPO were prone to be electrically leaky due to charge hopping between multivalent ions.

Configurational entropy induced dielectric relaxation below the temperature or the permittivity maximum (T_{max}) at 105°C for the Al-based HEPO (Al_P). A maximum polarization (P_{max}) of 45.4 μC cm^{-2} and a remanent polarization (P_{rem}) of 22.1 μC cm^{-2} were achieved for Al_P at 10 kHz at an applied electric field of 1100 kV cm^{-1}. However, the Sc-based HEPO (Sc_P) was found to be more like a normal ferroelectric with no observed dielectric relaxation below T_{max} of 225°C. P_{max} of 52.5 μC cm^{-2} and P_{rem} of 24.6 μC cm^{-2} were obtained at 10 kHz at an applied field of 1100 kV cm^{-1}. It was found that T_{max}

increases with an increase in the average B-site cation size, consistent with structural characteristics.

Indirect measurements employing Maxwell relations were utilized to quantify the electrocaloric response of the films. Polarization-temperature curves (P-T curve) were extracted from temperature dependent Polarization-Electric field loops (P-E loop) from - 35°C to 275°C. In HEPO composition with multivalent ions such as Fe and Mn, bloated “banana”-like P-E loops were measured with increasing temperature, which was indicative of leakage. The temperature rise from the electrocaloric effect (ECE) of Al_P was determined to be 7.39 K and 5.82 J Kg^{-1} K^{-1}at 135°C for an applied electric field of 1100 kV cm^{-1}. ScP exhibited an electrocaloric temperature change of 5.74 K and an entropy change of 5.77 J Kg^{-1} K^{-1} for an applied electric field of 1100 kV cm^{-1} at 50°C. Apparent negative temperature of Fe-based HEPO (Fe_P) were attributed to leakage-induced artifacts.

Polarization stability was studied for HEPO films by employing a Positive-Up-Negative-Down (PUND) measurement protocol. By varying the pulse delay between measurement from 0.1 ms to 100,000ms, the polarization decay was estimated for Sc_P, Al_P, and 2 % Nb doped-$Pb(Zr_{0.52}Ti_{0.48})O_3$ (PZT) films. It was found that the magnitude of polarization drop ($\Delta dP = dP_{1\ ms} - dP_{100,000\ ms}$) was approximately 3.2 μC cm^{-2} for Sc_P and 10.3 μC cm^{-2} for Al_P, while that of PZT was only 1.5 μC cm^{-2}. This result implied that Al breaks the long-range polar order, leading to rapid decay of polarization in Al_P, compared to a normal ferroelectric such as PZT. In contrast, Sc_P underwent a relatively smaller drop of polarization, suggesting preservation of long-range polar order despite the existence of compositional disorder on the B site. A combination of PUND data and powder X-ray diffraction results suggests that Sc_P has field-induced phase transition from rhombohedral to tetragonal ferroelectric phases. The activation energy for the depolarization in Al_P was estimated to be $\approx 87\pm5$ meV for Al_P, compared to $\approx 152\pm2$ meV for PZT. By customizing the PUND profile to introduce 2 s of rest between measurement pulses, an enhanced ECE of 14.9 K was obtained for an Al_P film at an applied electric field of 1120 kV cm^{-1}.

Finally, the energy storage properties of antiferroelectric $(Pb_{0.87}Sr_{0.05}Ba_{0.05}La_{0.02})(Zr_{0.52}Sn_{0.40}Ti_{0.08})O_3$ (M-PZO) thin film capacitors were explored. Excellent crystallinity (FWHM of 0.021°) could be obtained on $SrRuO_3/SrTiO_3$ substrates by pulsed laser deposition (PLD). The out of plane lattice parameter of M-PZO was determined to be 4.110 ± 0.001 Å. The average maximum recoverable energy density was 88 ± 17 J cm^{-3} with an efficiency of 85 ± 6 % at 1 kHz and 80 ± 15 J cm^{-3} with an efficiency of 92 ± 4 % at room temperature. The capacitors could be cycled $>10^6$ at an applied electric field of 2 MV cm^{-1} before shoring significant loss of the energy storage density. This material is promising for high efficiency and low loss dielectric energy storage applications.

TABLE OF CONTENTS

LIST OF FIGURES

LIST OF TABLES

ACKNOWLEDGEMENTS

First and foremost, I would like to express my deepest gratitude to my advisor Professor Susan Trolier-McKinstry for giving me the opportunity to study. I would not have been able to complete my PhD without her dedication, support, generosity, and guidance. Her energy, enthusiasm, and hard work have continuously encouraged me to move forward and reach the final stage of my PhD journey. I would sincerely thank for her patience, assistance, feedback, and encouragement, particularly for my writing. I truly cannot thank enough for what she has done for me. I feel incredibly fortunate to have had her as an advisor and am proud to be a member of the STM group.

I would also sincerely thank my committee members: Professor Clive A. Randall, Jon-Paul Maria, and Qiming Zhang for their support, discussion, and directions to improve the quality of this work.

I also thank the members of the STM group, past and present, for their kindness and support. I have enjoyed every discussion and experiment with them: Song-Won Ko, Jung-In Yang, Beth Jones, Wanlin Zhu, Smitha Shetty, Betul Akkopru Akgun, Fan He, Stanislav Udovenko, Sandie Elder, Christopher Cheng, Gavin Hennessey, Travis Peters, Yiwen Song, Pannawit Tipsawat, Leonard Jacques, Anthony Diaz-Huemme, Ryan Hawks, Haley Jones, Kuyhwe Kang, Reilly Knox, Roger Ma, Kae Nakamura, Erdem Ozdemir, Madeleine Petschnigg, Pedram Yousefian, Tianming Zhao, and Nathan Halford.

Special gratitude to the Materials Research Institute and Nanofabrication staff, past and present, for their support, help, comments and discussion. In particular, I thank Bill Drawl, Sarah Eichfeld, Jacob Lyons, Nathan Dotts, Damian Richards, Bruce Walker for

helping me set-up and maintain the pulsed laser deposition system in N-135A. Chad Eichfeld, Guy Lavallee, Kathleen Gehoski, Michael Labella, Bangzhi Liu, Andrew Fitzgerald, Bill Mahoney, Shane Miller, Jaime Reish helped me with tool training and discussion for process development in the Nanofab. Nichole Wondering, Anthony Richardella, Gino Tambourine, Julie Anderson, Tim Tighe, Sarah Kiemle, Jeff Long, Mike Norrell aided me with tool training and support for characterization tools. Without their help, I could not complete my study.

I would like to thank my collaborators. Dr. Christina Rost and John Barber for obtaining temperature-dependent X-ray diffraction data for structural analysis. Thank you to Dr. Nasim Alem and Sai Venkata Gayathri Ayyagari for helping me understand structural features using Transmission Electron Microscope. I am also grateful for Dr. Ismaila Dabo, Tara Karimzadeh, and Simon Gelin for discussion about electrocalorics and high entropy material research. Lastly, I would also thank for Dr. Xiaoli Tan for providing a ceramic target for the study of energy storage properties.

I gratefully acknowledge financial support through the Pennsylvania State University Materials Research Science and Engineering Centers DMR-2011839. The findings and conclusions do not necessarily reflect the view of the funding agency.

I would also like to thank my parents and brother: Byungho Son, Kuenhee Lee, and Minjun Son for their care and tremendous support throughout my PhD. No words can express my gratitude to my parents and brother.

Finally, I would like to extremely thank my wife, Hyemi Jeong, for her endless support. She has been always supportive, understanding, and encouraging throughout my PhD. Without her dedicated love, I could not complete this study.

Chapter 1

Introduction and Thesis Organization

1.1 Ferroelectricity

Ferroelectricity was discovered in Rochelle salt in 1921; however, practical application of this material was limited due to water-sensitivity of the salt [1]. In the mid-20th century, ferroelectricity was also identified in $BaTiO_3$ (the first man-made perovskite ferroelectric) and $PbZr_xTi_{1-x}O_3$ [2,3]. These discoveries marked a significant advance in ferroelectric materials, providing improved stability, stronger polarization response, and tunability of the properties via solid solution. Consequently, there have been a wide range of applications associated with ferroelectric materials, such as actuators, capacitors, ferroelectric random-access memories (FeRAMs), pyroelectric sensors, electro-optics, micro-electro-mechanical systems (MEMS), and film bulk acoustic resonators (FBAR), etc. [4–8].

Ferroelectric materials can be characterized by the development of spontaneous polarization along a crystallographically defined direction (at least two possibilities must exist) which can be re-oriented by an external electric field. Many ferroelectric materials undergo a structural phase transition from a non-polar, high-symmetry phase to a polar, low-symmetry phase with changing temperature. The temperature where this phase transition occurs is called the Curie temperature (T_C) and it is accompanied by a dimensional change in the unit cell. This is coupled with the development of spontaneous polarization in the structure and gives rise to anomalies in the dielectric, thermal, and elastic properties [9,10].

The most well-known crystal structure that hosts ferroelectricity is the ABO_3 perovskite structure, where A and B represent two different cation sites and O stands for the oxygen site. In this structure, the A-site is generally occupied by larger cations coordinating with twelve oxygens (12-fold), while the B-site hosts smaller cations adopting 6-fold coordination with oxygen. A schematic representation of the perovskite structure is given in Figure 1.1. This structure is highly adaptable in terms of taking a variety of ionic radii and valence states, providing extensive possibilities for property exploration [11]. Fundamentally, one origin of ferroelectricity has been described as a competition between long-range Coulomb forces favoring the ferroelectric phase and short-range repulsive forces preferring the non-polar cubic phase [12]. At the atomic level in perovskite structure, B-site cations with d^0 electronic configuration (empty d-orbitals) such as titanium are likely to form partially covalent bonding with oxygen 2p-orbitals, which suppresses the short-range repulsive force; likewise, hybridization between oxygen 2p-orbitals and lone-pair A-site cations such as lead can contribute to the emergence of ferroelectricity [12,13].

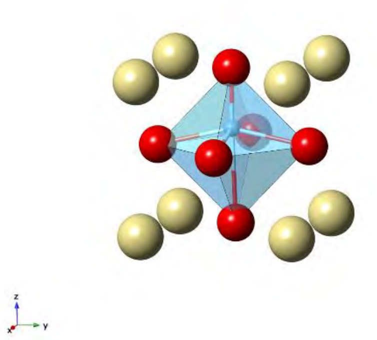

Figure 1.1. Schematic of perovskite unit cell. Red is oxygen, the light-yellow cation is on the A-site, and the blue cation is on the B-site of the unit cell. Note that B-site cation is slightly displaced from the center of the octahedron.

Reorientation of the spontaneous polarization in response to an applied electric field can generate a Polarization-Electric field hysteresis loop (P-E loop). A schematic illustration of the polarization response for a ferroelectric can be seen in Figure 1.2. Measurement of the P-E loop can be used for a proof of ferroelectricity in a given material. In ferroelectric materials, a net zero macroscopic polarization (point A in Figure 1.2) can occur due to the development of a domain structure which minimizes electrostatic and elastic energies; each domain is a region with (approximately) uniform polarization [14,15]. Application of a small electric field increases the polarization linearly by the following equation:

$$D = \varepsilon E$$

where D is the electric displacement, ε is the permittivity, and E is the electric field, which is shown here as segment A to B in Figure 1.2. With increasing electric field, non-linearity can be developed due to the nucleation and growth of domains. Domains aligned with the electric field are preferred thermodynamically. Thus, appropriated oriented crystals can be

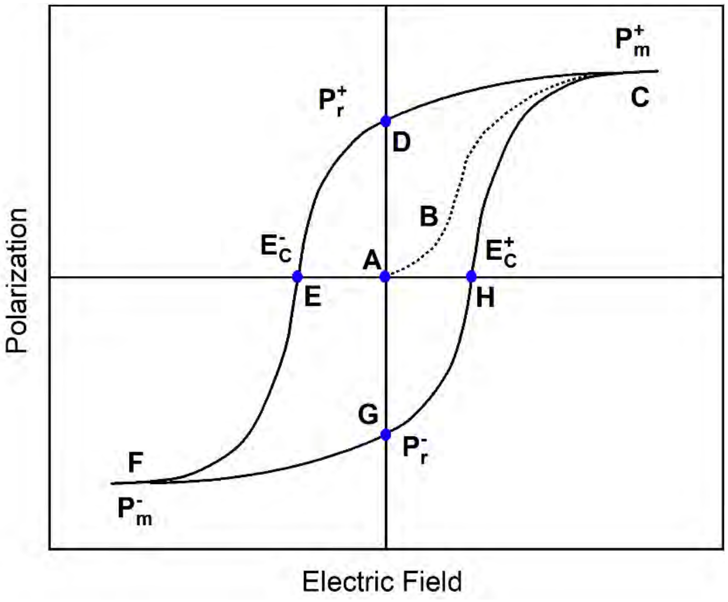

Figure 1.2. A schematic of a P-E loop

converted to a single domain at high enough electric fields (segment B to C). Upon the completion of this process, the polarization reaches a maximum ($\mathrm{P_m^+}$ at point C). When the field is removed, ferroelectric materials typically maintain some alignment of the spontaneous polarization ($\mathrm{P_r^+}$ at point D). The remaining polarization at zero field is called the remanent polarization. The field required to reduce the net polarization back to zero is called the coercive field ($\mathrm{E_C^-}$). This process is driven by promoting nucleation of new domains with oppositely aligned polarization (segment D to E). Further increase of the electric field in the negative direction continues the nucleation and growth of the new domains and eventually reach point F where it shows maximum polarization with opposite direction ($\mathrm{P_m^-}$). Reversing the field direction again leads to a remanent polarization in the negative direction and the cycle can be completed at the positive coercive field ($\mathrm{E_C^+}$ at point H).

1.2 Electrocaloric Effects

The Heckman diagram, as shown in Figure 1.3, visualizes correlations between thermodynamic variables in ferroelectrics, such as polarization (P), temperature (T), and stress (σ) [16]. Ferroelectric materials exposed to mechanical strain, electric field, and temperature, exhibit piezoelectric, dielectric, and pyroelectric effects, respectively. The electrocaloric effect (ECE) originates from the dependence of the entropy change on the application of electric field. Thus, the ECE is the electric field-induced isothermal entropy change or adiabatic temperature change of ferroelectric materials. A majority of the entropy change in ferroelectric material is associated with polar entropy.

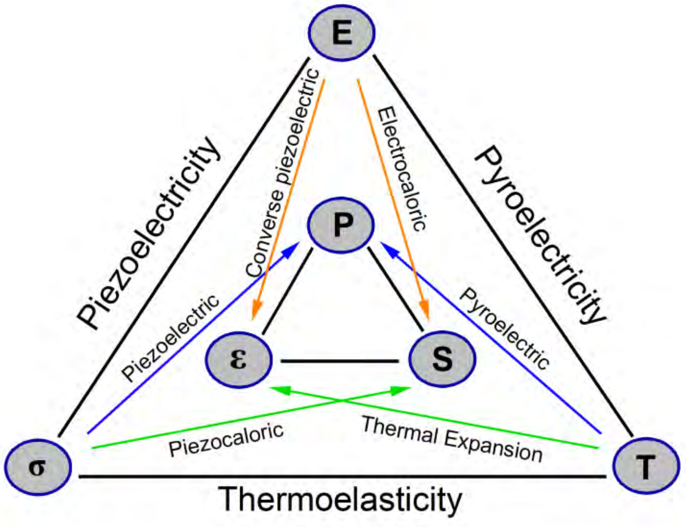

Figure 1.3. Heckman diagram for showing thermal-electrical-mechanical coupling in ferroelectric materials. Figure redrawn from [16].

The first experimental ECE was observed in Rochelle salt crystals in 1930 [17]. However, due to the very small temperature change, which is too small to be useful, the ECE remained one of the least understood properties of ferroelectric materials. However, since the discovery of a large ECE in $PbZr_{0.95}Ti_{0.05}O_3$ thin films (~12 K), research on ECE in ferroelectric materials has accelerated [18]. EC cooling is a developing energy efficient cooling technology with the potential to replace vapor-compression cooling; this in turn should reduce emission of harmful green-house gases [19]. Furthermore, ECE-based devices hold promise for application where small size is highly desired, such as personalized cooling or thermal management of electronic packages and batteries [20–22].

In Figure 1.4, the working principle of a Brayton-like electrocaloric cycle (Figure 1.4 (a)) is illustrated [23]. From point 1 to 2, dipoles in the electrocaloric material (EC material) can be aligned along the direction of an applied electric field. This alignment reduces the entropy associated with the dipoles. The system compensates for the entropy change by heating up the material, primarily through vibrational entropy changes. The EC material is then allowed to exchange heat with its surroundings (the heat sink). Due to the heat exchange, the temperature of the EC material drops until thermal equilibration is achieved. From point 3 to 4, removal of the electric field randomized the dipoles, increasing the entropy in the EC material. The induced drop of temperature in the EC material can then be used to trigger absorption of heat from the heat source. Finally, the temperature and entropy of the EC material return to the original state, ready for the next electrocaloric cycle.

Figure 1.4 (b) is a schematic representation of the temperature and the electric field change as a function of time during the electrocaloric cycle. There are several important considerations for this cycle. First, the time constant for applying the electric field has to be smaller than the time constant of thermal relaxation, in order to achieve adiabaticity. Secondly, a relatively large thermal volume (or mass) is required to cool large areas. Third, given that ECE-based devices transfer heat from a heat source to a heat sink, a large ΔT_{ECE} is preferred (at least >5 K) with a wide working temperature span (at least > 20 K) [23,24].

Generally, quantification of the ECE can be performed through both direct measurement and indirect measurements. Direct measurement techniques such as infrared cameras (IR camera), thermocouples, thermometers, differential scanning calorimetry (DSC), and thermal microscopy allow the electrically-induced temperature change to be measured [24–29]. However, these direct measurements can be questionable especially for thin films. This issue arises mainly due to the small thermal volume of the film, heat

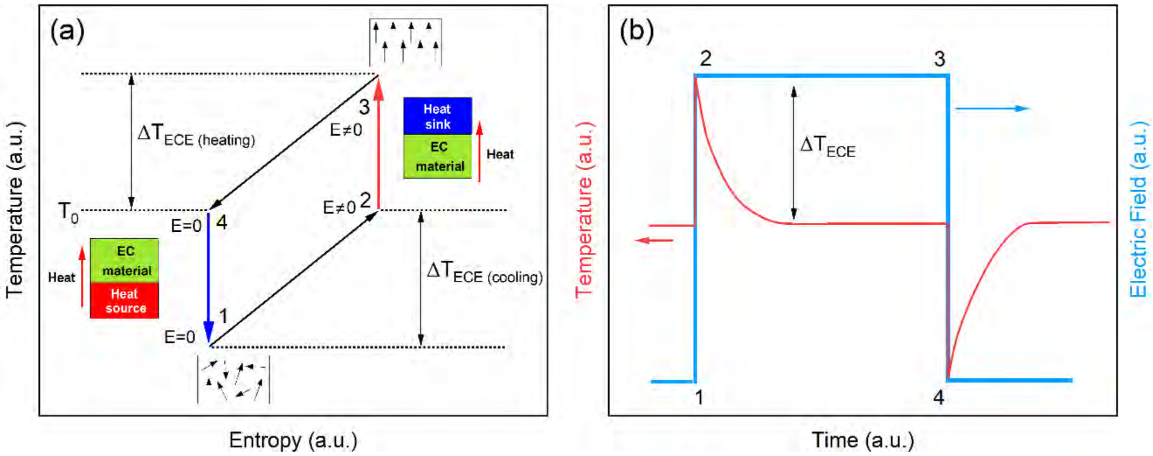

Figure 1.4. (a) Schematic illustration of a Brayton-like electrocaloric cycle and (b) temperature change and electric field change as a function of time. Figure redrawn from [23].

dissipation to the thick substrate, as well as inherent resolution limits of these techniques. Recently, a micro-sized metallic temperature sensor (employing the 3ω technique) has demonstrated the ability to capture electrocaloric temperature change for thin films with a sensitivity < 2 mK; this method mandates a complex fabrication process to create specialized devices structures [30,31].

In contrast, indirect measurement methods using Maxwell's relations are more frequently employed due to ease of applicability. In this approach, P-E loops are measured as a function of temperature and $(\frac{\mathrm{dP}}{\mathrm{dT}})_{\mathrm{E}}$ is extracted from the polarization vs temperature curve plotted as a function of the applied electric field [28]. The isothermal entropy change and adiabatic temperature change then can be estimated by using the following equations [18].

$$\Delta \mathrm{S} = \frac{1}{\rho}\int_{\mathrm{E}_1}^{\mathrm{E}_2} (\frac{\mathrm{dP}}{\mathrm{dT}})_{\mathrm{E}} \mathrm{dE}$$

$$\Delta T = -\int_{E_1}^{E_2} (\frac{T}{\rho C_\rho})(\frac{dP}{dT})_E dE$$

where E_1 and E_2 are the initial and final electric field applied, ρ is the density of the material, T is the temperature, C_ρ is the specific heat capacity, and P is the polarization.

While this indirect method facilitates estimation of the ECE, there are several notable limitations. First, the extracted ECE cannot be correct given the thermal boundary conditions imposed by the substrate. Thus, it violates the assumption of reversible thermodynamics implied in Maxwell's relations [29]. Additionally, perfect adiabaticity is not feasible in practice, especially for the case of thin films. The small thermal mass of the thin film coupled with the thicker substrate (and electrode) dissipate heat from the ECE [32]. Further, the indirect method also is ambiguous in non-equilibrium system such as relaxor ferroelectrics, despite its convenience [33].

1.3 Relaxor Ferroelectricity

In late 1905's, the first Pb-based relaxor ferroelectrics were reported: $Pb(Ni_{1/3}Nb_{2/3})O_3$ (PNN) and $Pb(Mg_{1/3}Nb_{2/3})O_3$ (PMN) [34]. Relaxor ferroelectrics can be distinguished from normal ferroelectrics such as $BaTiO_3$ (BTO) and $PbTiO_3$ (PTO) by the following facts [35].

1) They exhibit frequency-dependent dispersion of the dielectric constant below the temperature of the maximum in the dielectric constant (T_{max}). Above T_{max}, the dielectric dispersion collapses.
2) There is no evident structural change at T_{max}; in contrast, symmetry breaking occurs at T_{max} for normal ferroelectrics such as BTO and PTO.

3) Relaxors display slim hysteresis P-E loops below T_{max}, though typical ferroelectric hysteresis P-E loops may develop at temperatures far below T_{max} (e.g., PMN).
4) There is a large deviation from the Curie-Weiss law for the dielectric constant above T_{max}. The temperature where deviation occurs is called the Burns temperature (T_B).
5) There are no sudden changes in functional properties such as the index of refraction, unit-cell volume, and birefringence, etc. at T_{max}.

PMN or PMN-derived solid solutions such as PMN-PT are well-known for high dielectric permittivity and electro-mechanical coupling. This family of materials has been employed for applications such as actuators for the secondary mirrors in the Hubble telescope, piezoelectric transducers for medical/sonar technology, high-power dielectric capacitors, pyroelectric sensor, etc. [36–38].

Despite their technological importance, the origin of relaxor ferroelectricity is still debated. Generally, relaxor ferroelectricity is associated with nanometer-scale compositional inhomogeneity on the cation sites; these in turn are associated with polar nanoregions (PNRs) [35,39]. In perovskite-based relaxor ferroelectrics, a mix of ordered and disordered site occupancy introduces random local electric fields, disrupting the long-range polar ordering which is responsible for normal ferroelectricity. At sufficiently high temperatures, relaxor ferroelectrics also exhibit a paraelectric-like response. However, below T_B, the PNRs become more prominent with a typical size of a few nanometers [40]. PNRs are highly dynamic and susceptible to external stimuli such as temperature. For example, in PMN, PNRs originating from compositional fluctuation between Mg^{2+} and Nb^{5+} ion leads to the diffusiveness of T_{max}. Upon cooling further, the volume fraction of

PNRs is prone to increase, thus the frequency of the (volumetric) fluctuation decreases, resulting in dispersion in dielectric permittivity [35]. The frequency dependent dielectric susceptibility of relaxor ferroelectrics is often described by the Vogel-Fulcher function [41]:

$$\omega = \omega_0 \exp\left[\frac{-E_A}{K_B(T_{max} - T_f)}\right]$$

where ω is the angular measurement frequency, ω_0 is the phonon frequency (pre-exponential angular frequency), E_A is the activation energy for polarization relaxation, T_{max} is the temperature where the dielectric maximum occurs, T_f is the freezing temperature, and K_B is Boltzmann's constant.

1.4 Energy Storage Dielectrics

Dielectric capacitors are ubiquitous in modern electronic devices. Unlike other energy storage technologies, such as Li-ion batteries, they store energy in a purely electrostatic fashion. Li-ion batteries store (charging) and transfer (discharging) energy via redox reactions through an electrolyte in the cell. They are highly valued for applications requiring a stable and long-term energy supply, such as cell phones or electric vehicles, due to their reasonably large energy density (> 10^2 Wh kg^{-1}) and stable energy transfer [42]. However, the slow movement of charge carriers during charging/discharging makes them unsuitable for applications demanding high power output.

In contrast, dielectric capacitors, which store energy electrostatically, can generate considerably larger power densities (> 10^7 W kg^{-1}) due to their fast charging/discharging rates [42]. Moreover, the absence of an electrolyte permits larger voltages (> 5 V) and good reliability, making them strong candidates for power electronics and pulsed power applications [43].

Commercialized dielectric energy storage capacitors include polypropylene (PP), polyethylene terephthalate (PET), and $BaTiO_3$ (BTO) due to their excellent stability, graceful failure, and long lifespan [44,45]. However, these BTO and polymer-based dielectric capacitors have energy densities of only a few J cm^{-3}, resulting in bulky sizes [45]. Thus, to facilitate dimensional scaling of electronic devices, development of new dielectric capacitors with large energy density is desired. The energy storage density can be calculated from [46]:

$$J = \int_{P_0}^{P_{max}} E\,dP \approx \frac{\varepsilon_0 \varepsilon_r E^2}{2}$$

where J is the energy storage density, ε_0 is the vacuum permittivity, ε_r is the relative permittivity of the material, E is the electric field, P_{max} is maximum polarization and P_0 is the polarization at zero electric field, and P is the resulting polarization of the dielectric

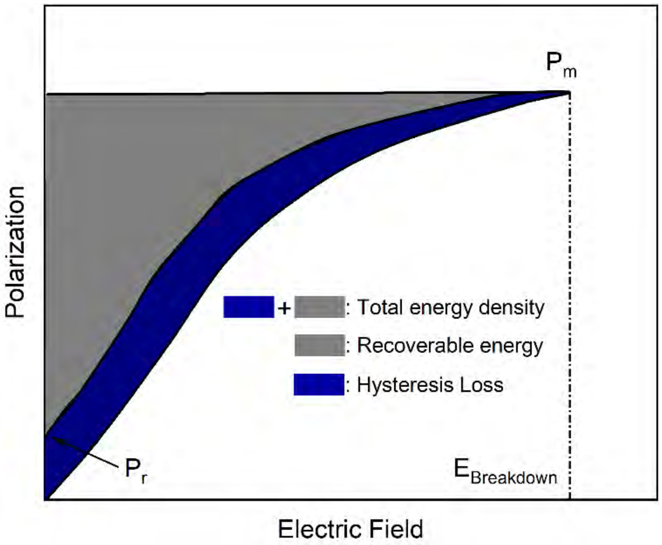

Figure 1.5. Schematic of total energy storage density, recoverable energy density, and hysteresis loss from a unipolar P-E loop.

layer. A combination of large permittivity, polarization, and breakdown strength enables a large energy storage density.

The energy storage density can be determined by evaluating the P-E loop, as shown in Figure 1.5. In Figure 1.5, the grey area represents the recoverable energy density, while the dark blue area shows the high field hysteresis loss. The sum of these two corresponds to the total energy density.

When evaluating the usefulness of a dielectric capacitor, two important parameters are generally considered; energy storage density (J cm^{-3}) and efficiency (%), represented by $\eta\ (\text{efficiency}) = \frac{\text{Recoverable energy density}}{\text{Total energy density (recoverable+loss)}}$. Given the potentially fast charging/discharging speed of a dielectric capacitor, minimizing loss is highly desirable for better temperature control.

Non-linear dielectrics such as some ferroics are of interest for energy storage capacitors due to their larger polarization compared to linear dielectrics. Figure. 1.6 shows

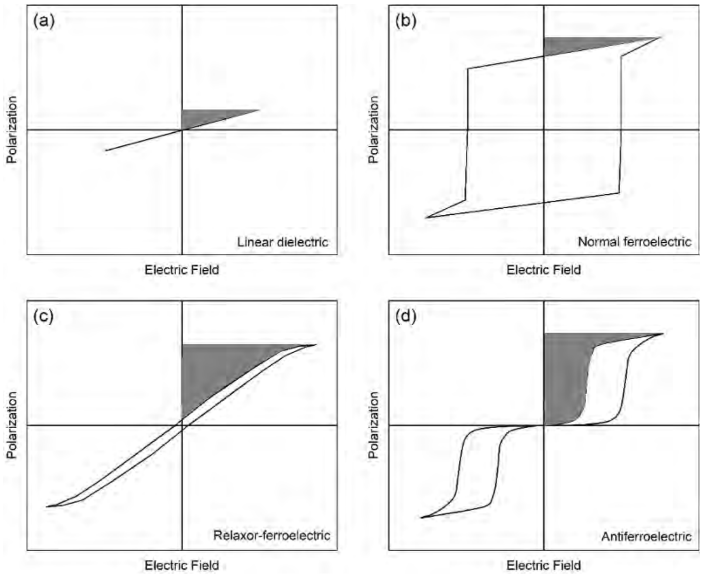

Figure 1.6. Schematics of the P-E loops for a (a) linear dielectric, (b) normal ferroelectric, (c) relaxor ferroelectric, and (d) antiferroelectric with the estimated energy storage density colored grey. Redrawn from [43].

P-E loops of a linear dielectric (a), normal ferroelectric (b), relaxor ferroelectric (c), and antiferroelectric (d). The shaded area represents the estimated energy storage density derived from these P-E loops. Clearly, relaxor and antiferroelectric possess superior energy storage performance due to their large maximum polarization (P_{max}) and low remanent polarization (P_r). Moreover, thin films of these materials can handle much larger electric fields, compared to the bulk counterparts, greatly enhancing energy storage performance. However, especially for antiferroelectrics, significant hysteresis loss associated with the field-induced phase transition and domain wall motion has to be addressed. Most of energy lost by hysteresis loss is converted into heat and this becomes a problematic particularly at high frequencies. Therefore, it is necesary to achieve large energy storage density and high efficiency simultaneously to advance energy storage in dielectric thin film capacitors.

1.5 High Entropy Oxides

Complex oxides often refer to oxide materials with at least two other additional elements. One of the most well-known structures of complex oxides is the ABO_3 perovskite structure. This structure hosts a wide range of functional properties such as superconductivity, ferroelectricity, piezoelectricity, spin-orbit coupling, etc. [7,47–50].

Inspired by discovery of High-Entropy Alloys (HEAs) in the early 2000s, Entropy-Stabilized Oxides (ESO), a new class of crystalline complex oxides, have recently been proposed. For example, the model system $Mg_{0.2}Co_{0.2}Ni_{0.2}Cu_{0.2}Zn_{0.2}O$ utilizes configurational entropy, rather than the enthalpy of mixing, to achieve phase stabilization [51–53]. The model ESO system tends to form a rock-salt solid solution at ~875°C and exhibits a reversible phase transformation (rock-salt to multi-phase) on varying temperature (1000°C to 750°C).

The Gibbs free energy provides the thermodynamic foundation to the understanding of ESOs.

$$G = \Delta H - T\Delta S$$

where G is the Gibbs free energy, H is enthalpy, T is temperature, and S is entropy. Enthalpy-stabilized systems can occur at all temperature ranges. However, at sufficiently high temperature, the entropy term ($-T\Delta S$) may become dominant. A more general term for this class of material is High Entropy Oxides (HEOs). Some researchers categorize a material as an HEO if the configurational entropy (S) exceeds $1.609R$ or the number of constituents exceeds five. The configurational entropy can be expressed by the following equation, based on Stirling's approximation and the Boltzmann hypothesis [54]:

$$S_{configurational} \approx -R\sum_{i} X_i lnX_i \approx Rln(n)$$

where R is the gas constant, and X_i is the molar content of the ith component. It is straightforward to see that the configurational entropy reaches its maximum with equimolar fraction of the constituents, as shown in Figure 1.7. Given the fact that multiple sublattices exist in some crystal structures, such as the ABO_3 perovskite, a second sum can be added to factor in contributions from multiple sublattices or oxygen vacancies, as shown in the following equation [55]:

$$S_{configurational} \approx -R\sum_{S} m_S \sum_{i} X_{i,S} lnX_{i,S}$$

where m_S is the multiplicity of the sublattice, $X_{i,S}$ is the molar content of the ith component on sublattice *S*.

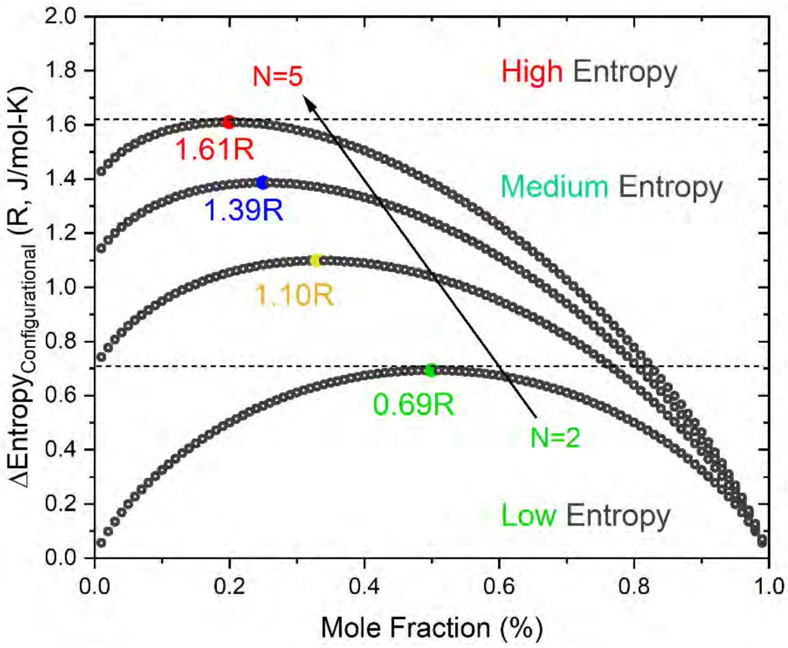

Figure 1.7. Configurational entropy as a function of mole fraction. N is the number of components in the material system and R is the gas constant. Figure redrawn from [53].

The mole fraction of elements in HEOs is typically chosen to be near equimolar to maximize the entropic contribution to the stabilization. ESO requires demonstration of an endothermic reaction, a reversible phase transformation, and/or theoretical validation of a positive enthalpy of formation [55,56]. Significant structural and electrical disorder created at the atomic scale in HEOs has facilitated a number of intriguing properties such as giant charge storage, superior ionic conductivity, low thermal conductivity, etc., making this class of material of interest for wide range of applications [57–59].

From the Gibbs free energy, it is apparent that HEO-like formulations are favored at high temperature and may be metastable phase at room temperature. If sufficient time is allowed upon cooling an HEO, the system is prone to lower its free energy via mechanisms such as phase decomposition and local clustering (chemical ordering). Energetically, a process of phase decomposition is relatively more expensive than local clustering due to the fact that a much longer diffusion distance is required [55]. Consequently, it is not surprising to observe local clustering or short-range ordering in HEO-like materials, which can potentially be a tuning knob for property engineering of HEOs.

1.6 Thesis Organization

This dissertation explores the synthesis, structure, and ECE and energy storage properties of HEO-like formulations. Chapter 2 addresses processing of Al and Mn-based HEO-like formulations, their phase development and their ECE. Chapter 3 examines eight different compositions of High Entropy Perovskite Oxide (HEPO) and their phase evolutions in both powders and films. Dielectric, ferroelectric, and electrocaloric properties are studied. Particularly, the time stability of the polarization is investigated using the Positive-Up-Negative-Down (PUND) measurement technique and the influence of dielectric relaxation on the enhanced ECE is discussed. Chapter 4 discusses fabrication of antiferroelectric-like thin film capacitors and their energy storage properties. Chapter 5 outlines conclusions and future experiments to be conducted, such as determination of the solubility limit of HEPOs, development of ferroelectricity and observation of ECE in high entropy fluorite structure, and investigation of the energy storage properties of a high entropy cubic pyrochlore thin film capacitor.

1.7 References

[1] J. Valasek, Piezo-Electric and Allied Phenomena in Rochelle Salt, Phys. Rev., 17 (4) (1921), pp. 475-481.

[2] C. Randall, R. E. Newnham, L.E. Cross, History of the First Ferroelectric Oxide, $BaTiO_3$, Materials Research Institute, The Pennsylvania State University, University Park, PA, USA, 1 (2004), p.1 https://ceramics.org/wp-content/uploads/2009/03/elec_division_member_papers1.pdf

[3] G. Shirane, A.Takeda, Phase Transitions in Solid Solutions of $PbZrO_3$ and $PbTiO_3$ (I) Small Concentrations of $PbTiO_3$, J. Phys. Soc. Jpn., 7 (1952), pp. 5-11

[4] Y. Xu, Ferroelectric Materials and Their Applications, Elsevier (2013)

[5] H. Ishiwara, Ferroelectric Random Access Memories, J. Nanosci. Nanotechnol., 12 (2012), pp. 7619–7627

[6] R.W. Whatmore, Pyroelectric Devices and Materials, Rep. Prog. Phys., 49 (12) (1986), pp. 1335-1386

[7] S. Trolier-McKinstry, P. Muralt, Thin Film Piezoelectrics for MEMS, J. Electroceram., 12 (2004), pp. 7–17

[8] R.C. Ruby, P. Bradley, Y. Oshmyansky, A. Chien, J.D. Larson, Thin Film Bulk Wave Acoustic Resonators (FBAR) for Wireless Applications, Proc. IEEE Int. Ultrasonics Symp. (IUS) (2001), pp. 813–821

[9] B.A. Strukov, A.P. Levani͡uk, Ferroelectric Phenomena in Crystals: Physical Foundations, Springer Verlag (1998)

[10] K.M.; Rabe, C.; Ahn, J.-M. Triscone, Physics of Ferroelectrics: A Modern Perspective, Springer Verlag, Berlin (2007)

[11] L.W. Martin, D.G. Schlom, Advanced Synthesis Techniques and Routes to New Single-Phase Multiferroics, Curr. Opin. Solid State Mater. Sci., 16 (2012) pp. 199–215

[12] R.E. Cohen, Origin of Ferroelectricity in Perovskite Oxides, Nature, 358 (1992), pp. 136-138

[13] P.S. Halasyamani, K.R. Poeppelmeier, Noncentrosymmetric Oxides, Chem. Mater., 10 (1998), pp. 2753–2769

[14] M. Lines, A. Glass, Principles and Applications of Ferroelectrics and Related Materials, Oxford University Press, Oxford (2001)

[15] J.S. Speck, A. Seifert, W. Pompe, R. Ramesh, Domain Configurations due to Multiple Misfit Relaxation Mechanisms in Epitaxial Ferroelectric Thin Films. II. Experimental Verification and Implications, J. Appl. Phys., 76 (1994), pp. 477–483

[16] J. Nye, Physical Properties of Crystals: Their Representation by Tensors and Matrices, Clarendon Press, Oxoford (1985)

[17] G.G. Wiseman, J.K. Kuebler, Electrocaloric Effect in Ferroelectric Rochelle Salt, Phys. Rev., 131 (1963), p. 2023

[18] A. Mischenko, Q. Zhang, J. F. Scott, R.W. Whatmore, N. D. Mathur, Giant Electrocaloric Effect in Thin-Film $PbZr_{0.95}Ti_{0.05}O_3$, Science, 311 (2006), pp. 1270-1271

[19] M. Valant, Electrocaloric Materials for Future Solid-State Refrigeration Technologies, Prog. Mater. Sci., 57 (2012), pp. 980–1009

[20] S. Hong, Y. Gu, J. K. Seo, J. Wang, P. Liu, Y. S. Meng, S. Xu, R. Chen, Wearable Thermoelectrics for Personalized Thermoregulation, Sci. Adv., 5 (2019), eaaw0536

[21] H. Gu, X. Qian, X. Li, B. Craven, W. Zhu, A. Cheng, S.C. Yao, Q.M. Zhang, A Chip Scale Electrocaloric Effect based Cooling Device, Appl. Phys. Lett., 102 (2013), Article 122904

[22] R. Ma, Z. Zhang, K. Tong, D. Huber, R. Kornbluh, Y.S. Ju, Q. Pei, Highly Efficient Electrocaloric Cooling with Electrostatic Actuation, Science, 357 (2017) p. 1130–1134

[23] Y. Meng, J. Pu, Q. Pei, Electrocaloric Cooling over High Device Temperature Span, Joule, 5 (2021), pp. 780-793

[24] Y. Nouchokgwe, P. Lheritier, C.H. Hong, A. Torelló, R. Faye, W. Jo, C.R.H. Bahl, E. Defay, Giant Electrocaloric Materials Energy Efficiency in Highly Ordered Lead Scandium Tantalate, Nat. Commun., 12 (2021), Article 3298

[25] S. Crossley, T. Usui, B. Nair, S. Kar-Narayan, X. Moya, S. Hirose, A. Ando, N.D. Mathur, Direct Electrocaloric Measurement of $0.9Pb(Mg_{1/3}Nb_{2/3})O_3$-$0.1PbTiO_3$ Films using Scanning Thermal Microscopy, Appl. Phys. Lett., 108 (2016), Article 32902

[26] S. Kar-Narayan, S. Crossley, X. Moya, V. Kovacova, J. Abergel, A. Bontempi, N. Baier, E. Defay, N.D. Mathur, Direct Electrocaloric Measurements of a Multilayer Capacitor using Scanning Thermal Microscopy and Infra-Red Imaging, Appl. Phys. Lett. 102 (2013)., Article 32903

[27] S.G. Lu, B. Rožič, Q.M. Zhang, Z. Kutnjak, X. Li, E. Furman, L.J. Gorny, M. Lin, B. Malič, M. Kosec, R. Blinc, R. Pirc, Organic and Inorganic Relaxor Ferroelectrics with Giant Electrocaloric Effect, Appl. Phys. Lett., 97 (2010), Article 162904

[28] C. Xavier Moya, E. Stern-Taulats, S. Crossley, D. González-Alonso, S. Kar-Narayan, A. Planes, L. Mañosa, N.D. Mathur, Giant Electrocaloric Strength in Single-Crystal $BaTiO_3$, Adv. Mater., 25 (2013), pp. 1360–1365

[29] Y. Liu, J.F. Scott, B. Dkhil, Direct and Indirect Measurements on Electrocaloric Effect: Recent Developments and Perspectives, Appl. Phys. Rev., 3 (2016), Article 31102

[30] S. Pandya, J.D. Wilbur, B. Bhatia, A.R. Damodaran, C. Monachon, A. Dasgupta, W.P. King, C. Dames, L.W. Martin, Direct Measurement of Pyroelectric and Electrocaloric Effects in Thin Films, Phys. Rev. Appl., 7 (2017), Article 034025

[31] C. Mart, T. Kämpfe, M. Czernohorsky, S. Eßlinger, S. Kolodinski, M. Wiatr, W. Weinreich, L.M. Eng, The Electrocaloric Effect in doped Hafnium Oxide: Comparison of Direct and Indirect Measurements, Appl. Phys. Lett., 117 (2020), Article 042903

[32] T. Tong, J. Karthik, L.W. Martin, D.G. Cahill, Secondary Effects in Wide Frequency Range Measurements of the Pyroelectric Coefficient of $Ba_{0.6}Sr_{0.4}TiO_3$ and $PbZr_{0.2}Ti_{0.8}O_3$ Epitaxial Layers, Phys. Rev. B., 90 (2014), Article 155423

[33] F. Le Goupil, A. Berenov, A.K. Axelsson, M. Valant, N.M.N. Alford, Direct and Indirect Electrocaloric Measurements on 〈001〉-$PbMg_{1/3}Nb_{2/3}O_3$-$30PbTiO_3$ Single Crystals, J. Appl. Phys., 111 (2012), Article 124109

[34] G.A. Smolenskii and A. I. Agranovskaya, Dielectric Polarization of a Number of Complex Compounds, Sov. Phys. Solid State., 1 (10) (1959), pp. 1429-1437

[35] L.E. Cross, E. Pugh, Relaxor Ferroelectrics, Ferroelectrics, 76 (1) (1987), pp. 241–267

[36] S. Zhang, F. Li, X. Jiang, J. Kim, J. Luo, X. Geng, Advantages and Challenges of Relaxor-$PbTiO_3$ Ferroelectric Crystals for Electroacoustic Transducers–A Review, Prog. Mater. Sci., 68 (2015), pp. 1-66

[37] K. Uchino, Ferroelectric Devices, Marcel Dekker, New York (2000)

[38] L. Eric Cross, Ferroelectric Materials for Electromechanical Transducer Applications, Jpn. J. Appl. Phys., 34 (1995) pp. 2525–2532

[39] C.A. Randall, A.S. Bhalla, T.R. Shrout, L.E. Cross, Classification and Consequences of Complex Lead Perovskite Ferroelectrics with regard to B-site Cation Order, J. Mater. Res. 5 (1990), pp. 829–834

[40] G. Xu, G. Shirane, J.R.D. Copley, P.M. Gehring, Neutron Elastic Diffuse Scattering Study of $Pb(Mg_{1/3}Nb_{2/3})O_3$, Phys. Rev. B., 69 (2004), Article 064112

[41] D. Viehland, S.J. Jang, L.E. Cross, M. Wuttig, Freezing of the Polarization Fluctuations in Lead Magnesium Niobate Relaxors, J. Appl. Phys., 68 (1990), pp. 2916–2921

[42] T. Christen, M.W. Carlen, Theory of Ragone Plots, J. Power. Sources., 91 (2000), pp. 210–216

[43] G. Wang, Z. Lu, Y. Li, L. Li, H. Ji, A. Feteira, D. Zhou, D. Wang, S. Zhang, I.M. Reaney, Electroceramics for High-Energy Density Capacitors: Current Status and Future Perspectives, Chem. Rev., 121 (2021), pp. 6124–6172

[44] Y.B. Adediji, A.M. Adeyinka, D.I. Yahya, O. V. Mbelu, A Review of Energy Storage Applications of Lead-Free $BaTiO_3$-based Dielectric Ceramic Capacitors, Energy Ecol. Environ., 8 (2023), pp. 401–419

[45] H. Luo, X. Zhou, C. Ellingford, Y. Zhang, S. Chen, K. Zhou, D. Zhang, C.R. Bowen, C. Wan, Interface Design for High Energy Density Polymer Nanocomposites, Chem. Soc. Rev., 48 (2019), pp. 4424–4465

[46] N.H. Fletcher, A.D. Hilton, B.W. Ricketts, Optimization of Energy Storage Density in Ceramic Capacitors, J. Phys. D: Appl. Phys., 29 (1996), pp. 253–258

[47] J.G. Bednorz, K.A. M̈ller, Possible High T_C Superconductivity in the Ba-La-Cu-O System, Ten Years of Superconductivity: 1980-1990, Springer (1986), pp. 267-271

[48] M. Dawber, K.M. Rabe, J.F. Scott, Physics of Thin-Film Ferroelectric Oxides, Rev. Mod. Phys., 77 (4) (2005), pp. 1083-1130

[49] K.J. Choi, M. Biegalski, Y.L. Li, A. Sharan, J. Schubert, R. Uecker, P. Reiche, Y.B. Chen, X.Q. Pan, V. Gopalan, L.Q. Che, D.C. Schlom, C.B. Eom, Enhancement of Ferroelectricity in Strained $BaTiO_3$ Thin Films, Science, 306 (2004), pp. 1005–1009

[50] T. Nan, T.J. Anderson, J. Gibbons, K. Hwang, N. Campbell, H. Zhou, Y.Q. Dong, G.Y. Kim, D.F. Shao, T.R. Paudel, N. Reynolds, X.J. Wang, N.X. Sun, E.Y. Tsymbal, S.Y. Choi, M.S. Rzchowski, Y.B. Kim, D.C. Ralph, C.B. Eom, Anisotropic Spin-Orbit Torque Generation in Epitaxial $SrIrO_3$ by Symmetry Design, Proc. Natl. Acad. Sci., 116 (2019) pp. 16186–16191.

[51] B. Cantor, I.T.H. Chang, P. Knight, A.J.B. Vincent, Microstructural Development in Equiatomic Multicomponent Alloys, Mater. Sci. Eng. A., 375–377 (2004), pp. 213–218

[52] J.W. Yeh, S.K. Chen, S.J. Lin, J.Y. Gan, T.S. Chin, T.T. Shun, C.H. Tsau, S.Y. Chang, Nanostructured High-Entropy Alloys with Multiple Principal Elements: Novel Alloy Design Concepts and Outcomes, Adv. Eng. Mater., 6 (2004), pp. 299–303

[53] C.M. Rost, E. Sachet, T. Borman, A. Moballegh, E.C. Dickey, D. Hou, J.L. Jones, S. Curtarolo, J-P. Maria, Entropy-Stabilized Oxides, Nat. Commun., 6 (2015), Article 8485

[54] R. DeHoff, Thermodynamics in Materials Science, Thermodynamics in Materials Science CRC Press (2006)

[55] S.S. Aamlid, M. Oudah, J. Rottler, A.M. Hallas, Understanding the Role of Entropy in High Entropy Oxides, J. Am. Chem. Soc., 145 (2023), pp. 5991–6006.

[56] M. Brahlek, M. Gazda, V. Keppens, A.R. Mazza, S.J. McCormack, A. Mielewczyk-Gryń, B. Musico, K. Page, C.M. Rost, S.B. Sinnott, C. Toher, T.Z. Ward, A. Yamamoto, What is in a Name: Defining “High Entropy” Oxides, APL Mater., 10 (2022), Article 110902

[57] B. Yang, Y. Zhang, H. Pan, W. Si, Q. Zhang, Z. Shen, Y. Yu, S. Lan, F. Meng, Y. Liu, H. Huang, J. He, L. Gu, S. Zhang, L.Q. Chen, J. Zhu, C.W. Nan, Y.H. Lin, High-Entropy Enhanced Capacitive Energy Storage, Nat. Mater., 21 (9) (2022), pp. 1074–1080

[58] D. Bérardan, S. Franger, A.K. Meena, N. Dragoe, Room Temperature Lithium Superionic Conductivity in High Entropy Oxides, J. Mater. Chem. A Mater., 4 (2016), pp. 9536–9541

[59] A. J. Wright, Q. Wang, S. Ko, K. Chung, R. Chen, J. Luo, Size Disorder as A Descriptor for Predicting Reduced Thermal Conductivity in Medium-and High-Entropy Pyrochlore Oxides, Scr. Mater., 181 (2020), pp. 76-81

Chapter 2

Electrocaloric Effect of Perovskite High Entropy Oxide Films

Chapter 2 of this dissertation has been previously published in *Advanced Electronic Materials;* Y. Son, W. Zhu, S.E. Trolier-McKinstry, Electrocaloric Effect of Perovskite High Entropy Oxide Films, Adv. Electron. Mater., 8 (2022), Article 220352

2.1 Introduction

Rapid growth in the worldwide economy has led to concerns regarding global energy consumption and the environmental impact of increased greenhouse gas emissions [1]. As of 2016, heating and cooling residential and public buildings accounted for approximately 12% of the total energy consumption in the United States [2]. Given that many heating, ventilation and air conditioning (HVAC) systems are building-wide, a considerable amount of energy is wasted heating or cooling empty spaces in buildings [3]. Recently, personal thermal management has garnered attention as an alternative that can deliver precise, adjustable temperature control to a target area, reducing wasted energy and increasing personal comfort [4,5].

Such small-scale cooling is also of interest for on-chip cooling of semiconductor circuits [6]. In 2020, data centers in the United State used an estimated 75 billion kWh, more than 2% of the nation’s total energy consumption. Approximately half of this energy was spent on cooling these centers [7]. Advanced cooling technology that directly cools Integrated Circuits (ICs) (rather than the entire data center) offers an alternative. Furthermore, IC miniaturization increased the power density of a packaged chip to 10^6 W cm^{-2} in 2018; power densities continue to rise, and often induces highly non-uniform heat generation [8]. It has been reported that more than 50% of IC failures are related to thermal control; this rate is expected to increase with further miniaturization [9]. Therefore, new approaches for local cooling of IC are needed [10].

Solid-state cooling, a potential solution, is highly compact, efficient, and environmentally friendly. Research involving thermoelectric, electrocaloric, and magnetocaloric effects is promising [11–13]. In 2006, large electrocaloric effects were observed in PZT thin films [14]. Unlike magnetocaloric and barocaloric materials, the electrocaloric effect does not require bulky external magnets or pressure apparatus. Electrocalorics enable relatively good energy efficiency that can be further improved via charge recovery [15,16]. Achieving large temperature changes in the electrocaloric material necessitates inducing large field-induced entropy changes. For this purpose, relaxor ferroelectrics are of special interest due to the disordered polarization and polar nanoregions [17].

A potential additional contribution to the entropy change in a ferroelectric-based material is to utilize high compositional complexity, e.g. through entropy engineering to further disorder the polarization on a local scale. In 2004, entropy stabilization of metallic alloys was introduced [18,19]. In 2015, the concept was broadened to include entropy stabilized oxides [20]. Various Entropy Stabilized Oxides (ESO) have shown high dielectric constants, superior ionic conductivity, and extremely high-temperature stability;

that is, entropy stabilization provides an additional approach to property tunability with respect to enthalpy-based compositional design [21–23]. In cases where reversible phase transformations have not yet been demonstrated, potential ESO may be called High Entropy Oxides (HEO) [24]. Triggered by the novel concept, several attempts to investigate the Electrocaloric Effect (ECE) based on HEO have been made. A-site disordered HEO ceramics show good temperature stability and a high ECE [25–27]. Moreover, high entropy polymeric films produced greatly enhanced ECE at 500 kV cm^{-1} [28]. In spite of the promising results, a study of ECE based on HEO film has been absent to date.

This paper discusses a new relaxor-type ferroelectric material based on entropy engineering and examines the effect of HEO-like formulations on electrocaloric responses. Pb was used for the A-site of the perovskite structure, while two different sets of compositions were used to populate the B-site. The first B-site precursor is based on hafnium (Hf), niobium (Nb), titanium (Ti), zirconium (Zr), and manganese (Mn), hereafter called the Mn precursor. After forming the perovskite phase, it is called the Mn PHEO. Correspondingly, for the second B-site precursor, aluminum (Al) replaces Mn (Al PHEO). PZT was chosen as a starting composition with a large electrocaloric effect [14]. Pb was fixed on the A-site because the lone electron pair promotes ferroelectricity [29]. For the B-site, Hf, Zr, Ti, and Nb all have $3d^0$ electron configuration as ions, which facilitates development of ferroelectricity in the perovskite structure [30]. Mn is a well-known Jahn-Teller ion that can induce lattice distortion which could be a source of additional entropy increase. Al has no 3d electrons, so that it can play a role as a disrupter of polarization, which could also be a source of additional entropy change, while simultaneously maintaining charge balance on the B-site of the perovskite structure. Both powders and thin films were prepared.

2.2 Experimental Procedure

Target Preparation: To fabricate a ceramic $Pb(Hf_{0.2}Zr_{0.2}Ti_{0.2}Nb_{0.2}Mn_{0.2})O_3$ target, a Mn-based B-site precursor was mixed using HfO_2 (Stanford Materials Corp, (99.9%), ZrO_2 (Alfa Aesar, 99.7%), TiO_2 (Alfa Aesar, 99.7%), Nb_2O_5 (Alfa Aesar, 99.9%), and Mn_2O_3 (Alfa Aesar, 98.0%) powders that were wet ball-milled with ethanol for 12 h. The resultant slurry was then dried at 80°C for > 24 h. The dried powder was calcined at temperatures from 1000℃ to 1400℃ for 240 min to homogenize the cation distribution and attempt to form a single-phase $Hf_{0.2}Zr_{0.2}Ti_{0.2}Nb_{0.2}Mn_{0.2}O_x$ (Mn precursor), following a columbite-like route [31]. However, despite multiple calcination, crushing, calcination cycles, single-phase precursors were not achieved up to 1400℃. After adding Pb_3O_4 (Sigma-Aldrich, 99%), single phase $Pb(Hf_{0.2}Zr_{0.2}Ti_{0.2}Nb_{0.2}Mn_{0.2})O_3$ perovskite was obtained with a calcination step at 750℃ for 240 min. After calcination, the powder was vibratory milled with 20% excess of PbO and pressed into a 1-inch pellet in a uniaxial press, followed by Cold Isostatic Pressing (CIP). The pressed pellet was sintered at 850°C for 120 min. The finished pellet was used as a target for PLD. A comparable procedure was used to make the Al-based PHEO target (Alfa Aesar, 99.0%), however, a single-phase was not achieved.

Film Deposition: Perovskite high entropy oxide thin films were synthesized using a KrF (248 nm) excimer laser (Compex 102 F, Coherent). For all growths, the laser energy density and substrate-target distance were fixed at 1.15 ± 0.04 J cm^{-2} and 40 mm, unless otherwise specified. The optimization process was carried out under varying deposition pressures, laser frequencies, and substrate temperatures for growth on $Pt/Ti/SiO_2/Si$

substrates (KOTech LLC) with a 60 nm Nb-doped PZT seed layer [32,33]. Mn PHEO films were synthesized with 175 mTorr, 90%O_3/10%O_2 deposition ambient, at a 630℃ substrate temperature and 10 Hz laser frequency. Identical processing conditions were utilized for Al PHEO films.

Structural Characterization: The phase purity and crystallographic orientation of the film was assessed using a PANalytical Empyrean diffractometer with Cu Kα X-ray radiation. The microstructures of the films were observed with a Merlin Field Emission Scanning Electron Microscope (FESEM) (Carl Zeiss Microscopy GmbH, Hena, Germany). Film compositions were characterized by Energy Dispersive X-ray Spectroscopy (AZtecLive Advanced Microanalysis system with an UltiMax 100 SSD Detector). A spectroscopic ellipsometer (Woollam M-2000 XF-193) was utilized to map the thickness uniformity of the sample. (Figure 2.S9)

Electrical Characterization: To characterize the electrical properties, platinum (Pt) top electrodes varying from 200 μm to 15 μm in diameter were prepared by double-layer resist photolithography and a lift-off process. 100 nm thick Pt electrodes were sputter deposited on the PHEO films (CMS-18 sputter system, Kurt J. Lesker Company, Pittsburgh, PA) over the resist stack. After lift-off, rapid thermal annealing was performed at 500℃ for 1 min to improve the contact between the Pt electrodes and the film. To expose the bottom electrode, 1827 (Shipley) photoresist was coated on the sample, defining the area for etching. After curing at 95℃ for 3 min, a 10:1 buffered HF etch was followed by a hydrochloric acid etch to remove the PHEO film. Finally, the photoresist was removed by acetone. To validate the quality of the top electrode patterning, the dielectric properties of Al PHEO were measured for various electrode sizes, as displayed in Figure 2.S6.

Dielectric and Ferroelectric Property Measurements: An HP 4284 LCR meter was utilized to measure the room temperature dielectric property of the films from 100 Hz to 100 kHz with 30 mV applied to a 200 μm diameter top electrode. Polarization-electric field hysteresis loops were obtained using a Precision Multiferroic tester (Radiant Technology) at 10 kHz. The temperature dependent dielectric measurement was performed with either an in-house probe station (Love_Film Stage) or a FormFactor 11000 from -50℃ to 285℃. An AC voltage of 100 mV was applied to the top electrode from 100 Hz to 1 MHz.

Electrocaloric Entropy and Temperature Change Calculation: To calculate the electrocaloric entropy and temperature changes, an indirect measurement approach based on Maxwell's relations was applied. The upper branches of the P-E loops were measured and fitted to a sixth order polynomial at temperatures from -50℃ to 280℃. A temperature interval of 10℃ was adopted to reduce peak shifts as reported elsewhere [34]. Numerical differentiation of the P(T) values was utilized as input equations (2) and (3).

$$\Delta T = -\int_{E_1}^{E_2} \frac{T}{\rho C_p} \left(\frac{dP}{dT}\right)_E dE \qquad (2)$$

$$\Delta S = \frac{1}{\rho} \int_{E_1}^{E_2} \left(\frac{dP}{dT}\right)_E dE \qquad (3)$$

where ρ is the mass density of the material, C_p is the specific heat capacity, P is the polarization, T is the measured temperature, and E_1 and E_2 are the initial and final applied electric fields, respectively. The theoretical density of Al PHEO determined by XRD was used and the heat capacity was assumed to be the same as that of $PbMg_{1/3}Nb_{2/3}O_3$-$PbTiO_3$ (PMN-PT).

2.3 Results and Discussion

2.3.1 PHEO Powder Processing

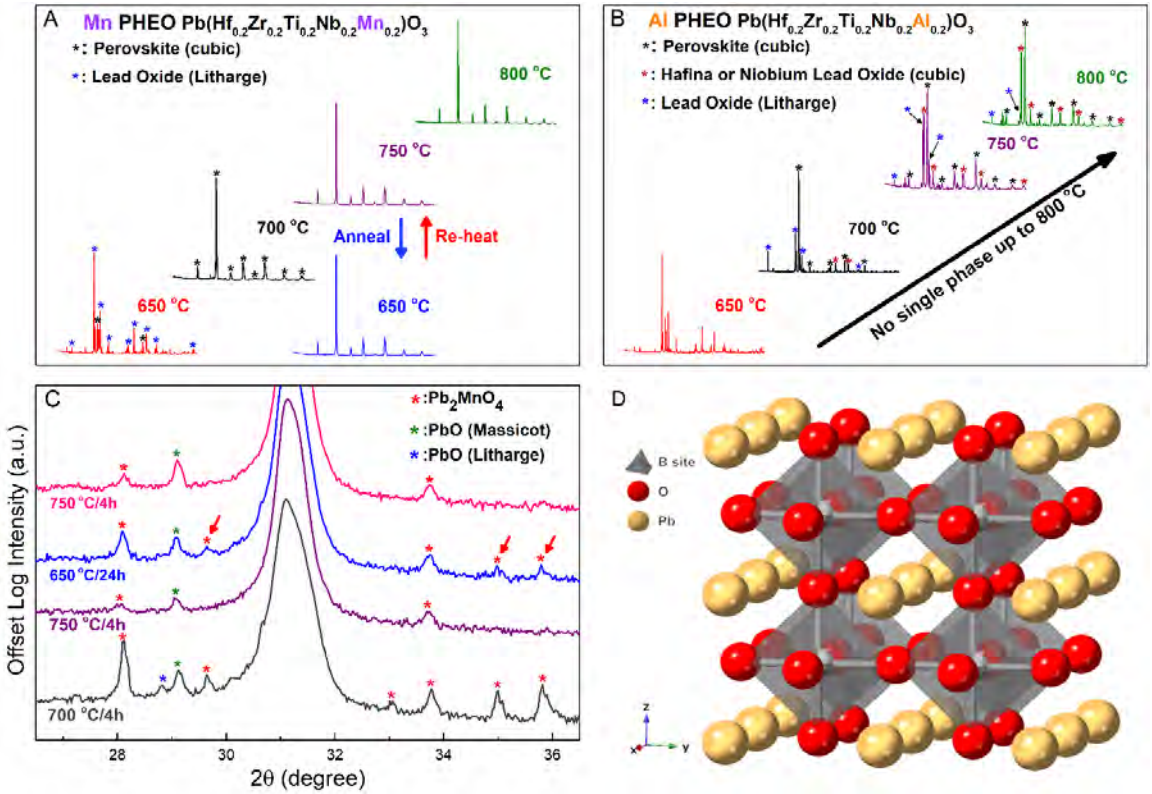

Figure 2.1. A) X-ray diffraction patterns of Mn PHEO from 650℃ to 800℃. B) Al PHEO X-ray patterns from 650℃ to 800℃. C) Cyclic phase transformation test of Mn PHEO and comparison based on the peaks around the perovskite 110 at ~31°. Red, green, and blue asterisks correspond to Pb_2MnO_4, PbO (Massicot), and PbO (Litharge), respectively. The peaks related to entropy-driven phase transformation are highlighted by red arrows. D) Crystal structure of pseudo-cubic perovskite high entropy oxide showing the B-site octahedra.

In order to reach a pseudo-cubic perovskite phase, in the PHEO compositions, the B-site precursor oxide powders were pre-mixed and heat-treated following a columbite-like process [31]. The results of heat treatment on the B-site powders are shown in Figure 2.S1 of the supplementary material. Lead oxide powder and the pre-treated B-site powder were mixed with a molar ratio of 1:1 and the batch was calcined. Several sequential heat treatments were performed to discover if a single phase could be developed and if entropy-driven cyclic phase transformations occurred. Figure 2.1A and 2.1B shows X-ray diffraction (XRD) patterns of the stoichiometric Mn PHEO and Al PHEO powders, respectively, heat treated from 650℃ to 800℃, for 4 hours periods. Litharge, cubic HfO_2 or niobium lead oxide ($Pb_{1.5}Nb_2O_{6.5}$), and perovskite peaks are marked with blue, dark red, and black asterisks, respectively. For the Mn PHEO calcined at 650℃, clear litharge peaks appear, indicating unmixed lead oxide. With increasing temperature, the litharge peaks decreased in intensity, accompanied by the development of perovskite peaks at 700℃. At 750℃, the powder was predominantly perovskite phase with minimal second phase peaks at ~28.1°, 29.2°, and 33.7°. The lattice constant of Mn PHEO powder annealed at 750℃ calculated based on the Nelson-Riley method was 4.062±0.001Å (Figure 2.S3 and Table 2.S1) [35].

After obtaining the perovskite phase at 750℃, a cyclic phase transformation test was conducted at 650℃ for 24 hours. This temperature minimized the volatility of the lead species; the longer annealing time off-set the resultant sluggish kinetics. Figure 2.1C highlights peaks around the perovskite 110 at ~ 31° 2θ. The Mn PHEO powder was heat-treated at 750℃ for 4 hours (purple), then annealed at 650℃ for 24 hours (blue). The powder was re-heated at 750℃ for 4 hours (pink). The red arrows indicate several peaks which occur <700℃ and disappeared at >750℃. Those peaks correspond to Pb_2MnO_4; it is prone to decompose into $Pb_3Mn_7O_{15}$ + PbO + Pb_3O_4 between 700℃ and 750℃ [36]. The decomposition in the 750℃ temperature range results in a relatively weak intensity at ~28.1° and 33.7°, and loss of the peaks at 29.6°, 35.0°, and 35.8°. In other words, the peaks marked by red arrows develop at ≤700℃ and the material is assimilated into the perovskite phase at temperatures ≥750℃. The existence of the peaks implies the entropy-driven phase transformation of an ESO [24]. The intensity of the entropy-driven secondary phase peaks is relatively weak due to slow kinetics of this transition.

For Al PHEO, cubic perovskite structure was obtained with some amount of unmixed lead oxide. With increasing temperature, the amount of unmixed lead oxide is reduced, but the intensity of peaks from cubic hafnia or niobium lead oxide ($Pb_{1.5}Nb_2O_{6.5}$) increases. Those peaks survive up to 1200℃, hindering the formation of single phase of Al PHEO powder. Therefore, cyclic phase transformation data and lattice parameter calculations are not available for Al PHEO.

2.3.2 PHEO Thin Films

To identify the best processing conditions for Mn PHEO films on Pt/Ti/SiO_2/Si substrates, the laser frequency, substrate temperature, and deposition pressure were varied individually, while other conditions were held constant. The XRD results of the optimization process are shown in Figure 2.S5 of the supporting information. It was found that phase-pure Mn PHEO film could not be fabricated on Pt/Ti/SiO_2/Si substrates for the range of conditions explored, as overlapping regions of Pb-rich pyrochlore or Pb-deficient pyrochlore phases occurred. The best processing conditions for Mn PHEO films on the platinized silicon substrate are: 175 mTorr O_3/O_2 deposition pressure, 10 Hz laser frequency, and substrate temperature of 630℃.

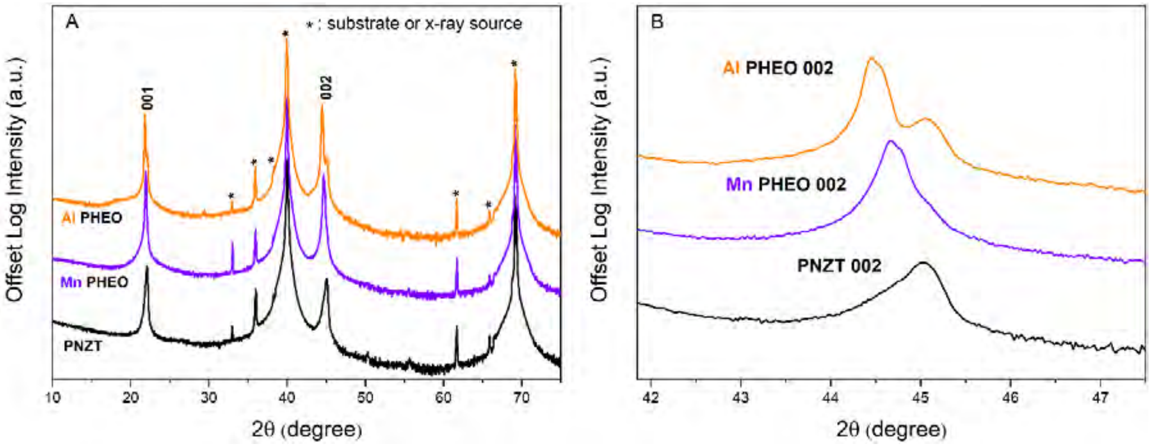

Figure 2.2. X-ray diffraction patterns of perovskite high entropy oxides films. A) PNZT seed layer (Black), Mn PHEO film on PNZT seed layer (Violet), and Al PHEO film on PNZT seed layer (Orange). B) Enlarged view around {200} to highlight peak shifting between Al PHEO and Mn PHEO.

To promote the formation of a single-phase perovskite film, a seed layer of 60 nm thick {100} oriented niobium doped lead zirconate titanate (PNZT) was grown on the Pt-coated Si substrate. PHEO films were then grown using the optimized conditions listed above. Figure 2.2A shows the XRD scans of Al PHEO (orange), Mn PHEO (violet), and the PNZT seed layer (black), respectively. Peaks from the substrate and other wavelengths from the X-ray source are marked with an asterisk (*). The films were grown to a thickness of ~ 490 nm; this should minimize the impact of the seed layer on the electrical properties. It is clear that the highly oriented PNZT seed layer promotes formation of phase-pure Mn PHEO with no detected secondary phase. For Al PHEO films, the predominant peaks are from the perovskite phase, with a small pyrochlore peak at ~ 31° and additional weak peak at ~ 19° 2θ. The XRD peaks from the Al PHEO film are well separated from those of the PNZT seed layer as shown in Figure 2.2B, while the peaks overlap in the Mn PHEO film.

In particular, the {200} diffraction peak of the Al PHEO appears at a lower angle compared to the Mn PHEO, indicating a larger out-of-plane lattice parameter. This occurred even though Mn^{3+} has a larger Shannon-Prewitt ionic radius than Al^{3+} for octahedral coordination [37]. Table 2.1 shows the lattice parameters of the PNZT seed layer, Mn PHEO, Mn PHEO powder and Al PHEO films, respectively. It is possible that the Mn ions occupied both B- and A-sites of the perovskite structure, or that much of the Mn adopted the 4+ oxidation state, reducing the lattice parameter significantly [38,39]. It is also possible that different Pb vacancy concentrations occurred in the Mn PHEO and Al PHEO films due to Pb volatility during vacuum processing. It should be noted here that the lattice parameter of Mn PHEO powder is larger than the out-of-plane lattice parameter of the corresponding film by 0.015 Å. This could be due to higher valence state of Mn or strain.

Table 2.1. Out-of-plane lattice parameters of PNZT seed layer, Mn PHEO film, Mn PHEO powder and Al PHEO films.

	PNZT seed layer	Mn PHEO film	Mn PHEO powder	Al PHEO film
a (Å)	4.024	4.047	4.062	4.076

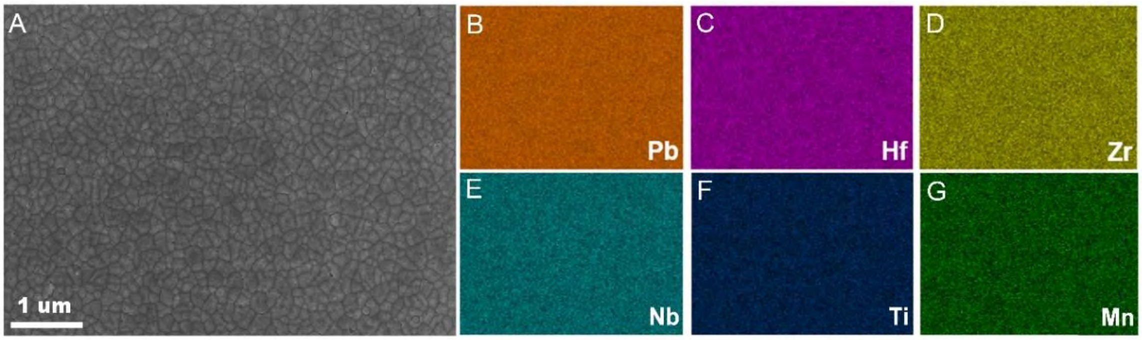

Figure 2.3. A) FESEM top view of a Mn PHEO film and B-G) EDS analysis showing homogeneity of the constituent elements.

The surface microstructure and chemical analysis of Mn PHEO and Al PHEO films are shown in Figure 2.3 and Figure 2.4, respectively. No distinguishable cracks or defects appear and the microstructure is dense, with average lateral grain sizes of 180 nm for both Mn PHEO and Al PHEO films. Boulders were seen on the surface of Al PHEO films, however, they were rarely seen on Mn PHEO films. Based on EDS results, both Mn PHEO and Al PHEO films were compositionally uniform with no segregation at the given length scale.

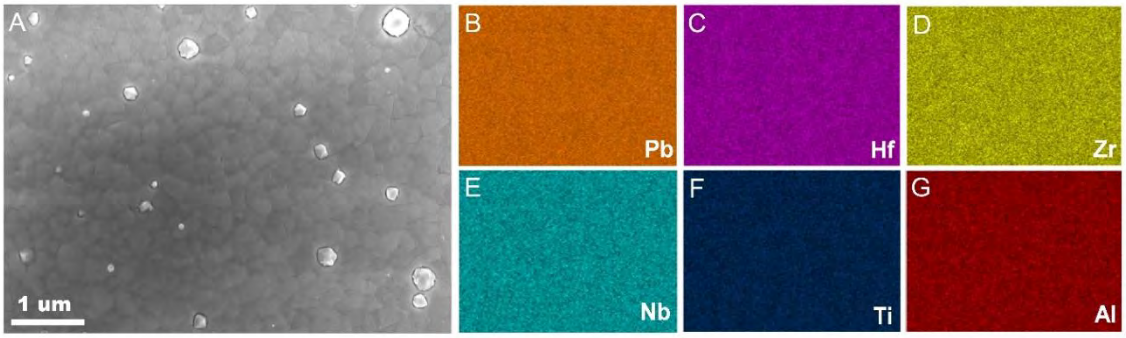

Figure 2.4. A) FESEM top view of an Al PHEO film and B-G) EDS analysis showing homogeneity of the constituent elements.

2.3.3 Room Temperature Dielectric and Ferroelectric Properties of Mn PHEO and Al PHEO

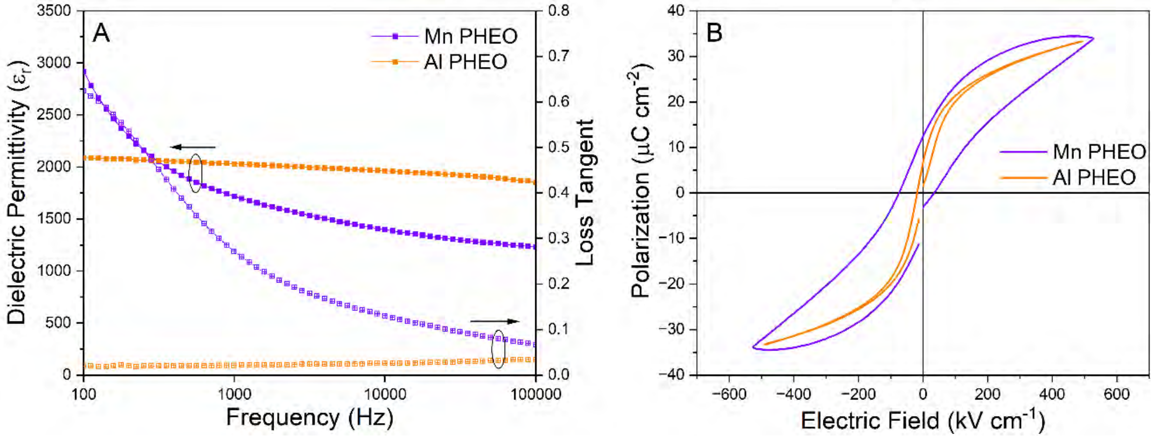

Figure 2.5. A) Dielectric permittivity and loss tangent. B) Ferroelectric hysteresis loops of the Mn PHEO (violet) and Al PHEO films (orange) measured at room temperature, respectively.

Figure 2.5A shows the room temperature dielectric permittivity and loss tangent of Mn PHEO and Al PHEO films; Mn PHEO films are represented by a violet line, Al PHEO films are represented by an orange line. Mn PHEO exhibited a relative permittivity of ~3000 at 100 Hz, but it decayed to 1500 at 100 kHz; the same trend was observed for the loss tangent. The frequency-dependent dielectric properties were attributed to space charge contributions originating from charge hopping between different valence states of Mn ions. In contrast, Al PHEO showed frequency-independent dielectric properties with a relative permittivity of ~2000 and a loss tangent <0.05 over the entire measured frequency range. The polarization loops (Figure 2.5B) of Al PHEO are very slim ferroelectric loops with low remanent polarization ($P_{rem} \approx 7.1$ μC cm^{-2}) for a maximum applied electric field of 520 kV cm^{-1}. The low remanent polarization from Figure 2.5B implies that long-range polar order can effectively be destroyed due to the presence of five different elements on the B-site. As shown later, the presence of relaxor ferroelectricity suggests that there may be nanopolar regions [40,41]. However, the Mn PHEO hysteresis loops are bloated and banana-shaped due to leakage, inflating the apparent remanent polarization [42]. Given the multivalency of Mn ions that adopts a mixture of 2+, 3+, and 4+ oxidation states, electron or hole hopping induces the bloated shape of the P-E loop for Mn PHEO in Figure 2.5B. However, Al has only 3+ oxidation state available, so the resulting film is a good electrical insulator. Thus, the slim relaxor-like P-E loops of Al PHEO can be produced.

Positive-Up and Negative-Down (PUND) measurements were performed to differentiate ferroelectric displacement currents from non-ferroelectric currents [43]. For Mn PHEO, the PUND polarization was only 1.8 μC cm^{-2}. Even though the Mn PHEO is electrically too conductive to be used in electrocaloric applications, the importance of the Mn PHEO can be underscored by the applicability of HEO-like formulations on Pb-based perovskites and the observation of the reversible cyclic phase transformation.

2.3.4 Temperature-Dependent Dielectric and Ferroelectric Properties of Al PHEO

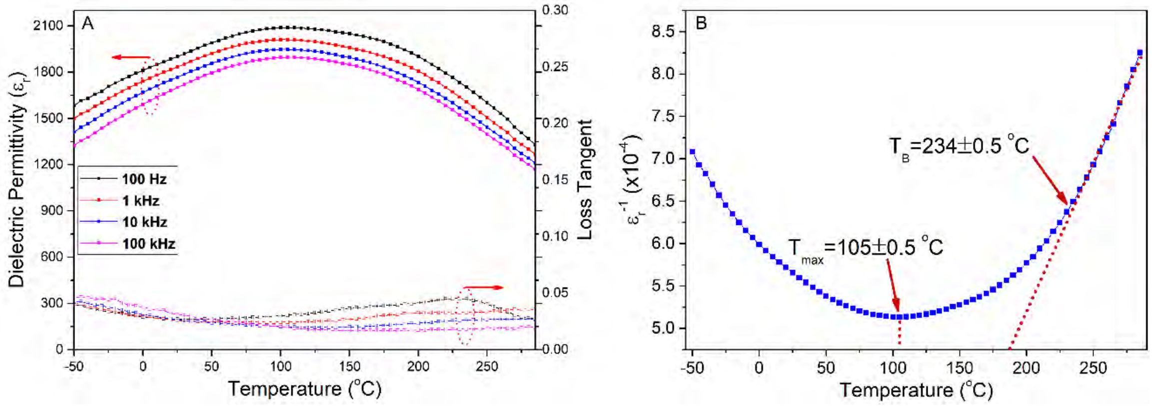

Figure 2.6. A) Dielectric permittivity and loss tangent of Al PHEO film from -50℃ to 280℃ at frequencies from 100 Hz to 100 kHz. B) Inverse dielectric permittivity vs. temperature indicating a dielectric maxima at 105℃ and a Burns temperature of 234℃. The red dotted line shows deviation from Curie-Weiss law below the Burns temperature

The dielectric response of Al PHEO was measured as a function of temperature, as shown in Figure 2.6A. The maximum dielectric permittivity, T_m, was 105℃. The material showed stronger frequency dispersion below T_m, and the data converged above this temperature. This is consistent with relaxor ferroelectric-like behavior for Al PHEO and it implies that polar entropy can be induced by multiple cations occupying the same lattice site [40]. There was some sample-to-sample variability in the permittivity values, even in cases where no differences could be observed in the X-ray patterns as shown in Figure 2.S7. It is likely that these differences are sensitive to the defect chemistry.

The plot of inverse dielectric permittivity against temperature is presented in Figure 2.6B. It is obvious that there is a clear deviation from Curie-Weiss law between T_m and the Burns temperature T_B, presumably due to the presence of polar nano regions (PNRs).[44] The relaxation behavior of Al PHEO is demonstrated via a modified Curie-Weiss law (Figure 2.S8):

$$\frac{1}{\varepsilon_r} - \frac{1}{\varepsilon_m} = \frac{(T-T_m)^{\gamma}}{C} \tag{1}$$

where ε_r is the dielectric permittivity, ε_m is the maximum dielectric permittivity, C is the Curie-Weiss constant, and γ is the degree of dielectric relaxation. The Curie-Weiss constant and relaxation constant were 2.94 (±0.02) × 10^5℃ and 1.91 (±0.03), consistent with the presumption that Al PHEO contains a certain amount of relaxor ferroelectric character.

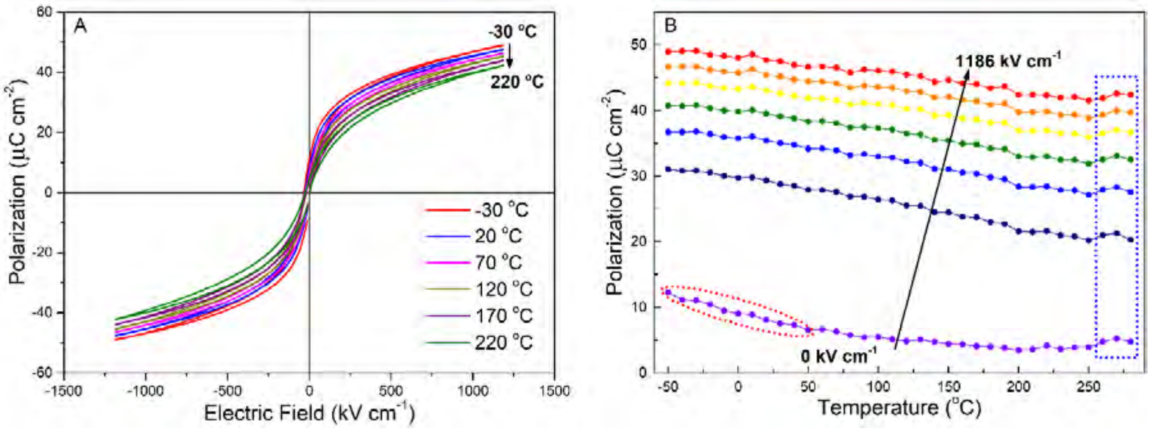

Figure 2.7. A) Ferroelectric hysteresis loops measured from -30℃ to 220℃. B) Maximum polarizations at different electric fields from 0 kV cm^{-1} to 1186 kV cm^{-1} from -50℃ to 280℃ at 10℃ intervals.

Figure 2.7A shows the ferroelectric loops of Al PHEO from -30°C to 220°C. The maximum applied field was 1186 kV cm^{-1}, less than half of the breakdown field (3000 kV cm^{-1}), to avoid breakdown during measurement. Notably, the shape of the loop was maintained over the measured temperature range although the P_{max} and P_{rem} dropped by 6 μC cm^{-2} and 8 μC cm^{-2}, respectively. Figure 2.7B shows the maximum polarization values as a function of temperature for electric fields from 0 kV cm^{-1} to 1186 kV cm^{-1}. Above 260℃, the apparent polarization was influenced by leakage currents, highlighted by the blue line [45]. The area highlighted by a red ellipse in Figure 2.7B represents a relatively sharp drop in remanent polarization due to the reduction of the long-range polar order [46]. The lines connecting the polarization data points are 6th order polynomial fits, used for the calculation of electrocaloric effects based on Maxwell's relations. Figure 2.S10 illustrates ferroelectric loops of Mn PHEO film measured from -30℃ to 120℃ temperature range. At -30℃, the loop shape is similar to that of Al PHEO, a slim and relaxor-like P-E loop. However, the loops become more "banana-like" with increasing temperature due to the lossy characteristic of the Mn PHEO as discussed previously [39]. Therefore, it could not be exploited for the electrocaloric calculation.

2.3.5 Electrocaloric Effect of Al PHEO film

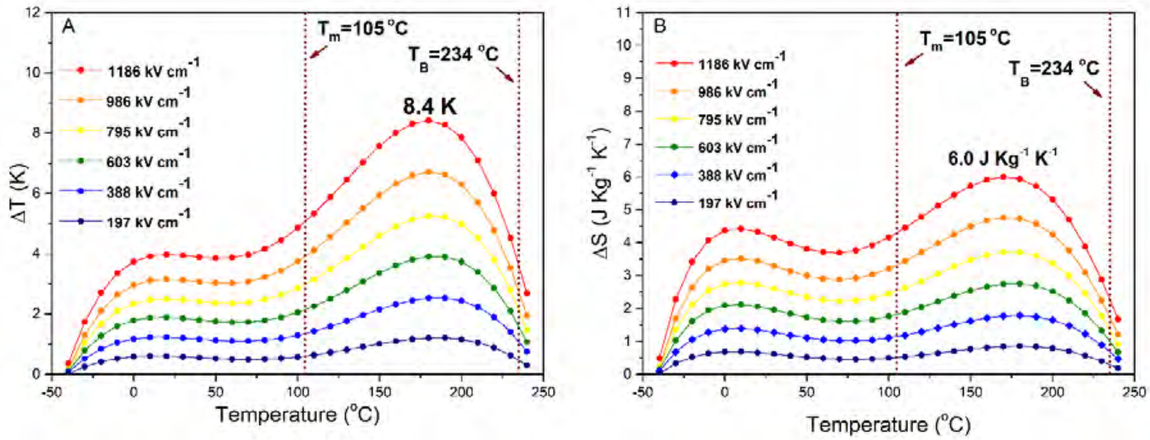

Figure 2.8. A) Electrocaloric temperature change of the Al PHEO. $\Delta E = E_2 - E_1$ where E_2 is fixed at 1186 kV cm^{-1}. Blue dotted lines are T_m and T_B, respectively. B) Corresponding entropy change of the Al PHEO.

To calculate the electrocaloric effects, the theoretical density of Al PHEO was determined using X-ray data, and the heat capacity was assumed to be the same as reported values for $PbMg_{1/3}Nb_{2/3}O_3$-$PbTiO_3$ (PMN-PT) [47]. The electrocaloric temperature change (ΔT_{ECE}) and the associated entropy change (ΔS_{ECE}) are shown in Figure 2.8A and 2.8B, respectively. The maximum ΔT_{ECE} of 8.4 K was obtained at 180℃; the corresponding maximum ΔS_{ECE} of 6.0 J Kg^{-1} K^{-1} was obtained at 170℃ with 1186 kV cm^{-1} applied electric field.

In the Al PHEO, two peaks were observed in the electrocaloric response, as has previously been reported in other relaxor ferroelectrics [48–50]. The first peak correlated with the loss of long-range polar order. This long-range order can be reintroduced by large applied electric fields, inducing an increase in the field-induced entropy change. As the temperature approached the dielectric maximum, field-induced switching of local polar order was facilitated by thermal fluctuations; This established the second peak in the electrocaloric responses, which was maximized at 180℃. Above this temperature, the electrocaloric response dropped and thermal randomization of the dipoles reduced the alignment. When the temperature reached T_B, the local polar order disappeared, producing a sharp drop of ΔT_{ECE}. The electrocaloric temperature change of the Al PHEO film is not as high as a recently proposed high entropy polymer [28]. However, it reveals a comparable temperature change to other oxide-based materials with a relatively wide working temperature range.

2.4 Conclusions

For powder processing, Mn PHEO can be obtained at 750℃ in 240 minutes with a minor amount of second phase formation. Mn PHEO powder undergoes an entropy-driven phase transformation. However, Al PHEO powder is not phase-pure under the same processing conditions. Mn and Al PHEO films were synthesized by PLD; their dielectric and ferroelectric properties were investigated and electrocaloric effect was evaluated based on Maxwell relations. Phase-pure Mn PHEO films were achieved; in Al PHEO films, a small amount of pyrochlore was detected under similar processing conditions. Mn PHEO films were electrically leaky, presumably due to mixed valence on the Mn ions. In contrast, Al PHEO films were insulating and exhibited relative dielectric permittivities of 2000 with loss tangents <0.05 at room temperature. Slim relaxor ferroelectric hysteresis loops were observed with P_{max} of 47.7 μC cm^{-2} and P_{rem} of 8.2 μC cm^{-2} at room temperature, with dielectric relaxation below T_m and progressive loss of the dispersion above T_m. The maximum indirect electrocaloric temperature change was 8.4 K at 180℃ with the applied electric field of 1186 kV cm^{-1}.

2.5 References

[1] S. Chu, A. Majumdar, Opportunities and Challenges for a Sustainable Energy Future, Nature, 488 (2012), pp. 294–303

[2] Annual Energy Outlook 2016 With Projections to 2040, (2016), Vol. 08, USDOE Energy Information Administration, Washington, DC

[3] M. Veselý, W. Zeiler, Personalized Conditioning and Its Impact on Thermal Comfort and Energy Performance – A Review, Renew. Sustain. Energy Rev., 34 (2014), pp. 401–408

[4] P.-C. Hsu, X. Liu, C. Liu, X. Xie, H.R. Lee, A.J. Welch, T. Zhao, Y. Cui, Personal Thermal Management by Metallic Nanowire-Coated Textile, Nano Lett., 15 (2014), pp. 365–371

[5] S. Hong, Y. Gu, J. K. Seo, J. Wang, P. Liu, Y. S. Meng, S. Xu, R. Chen, Wearable Thermoelectrics for Personalized Thermoregulation, Sci. Adv., 5 (2019), Article eaaw0536

[6] I. Chowdhury, R. Prasher, K. Lofgreen, G. Chrysler, S. Narasimhan, R. Mahajan, D. Koester, R. Alley, R. Venkatasubramanian, On-Chip Cooling by Superlattice-based Thin-Film Thermoelectrics, Nat. Nanotechnol., 4 (2009), pp. 235–238

[7] J. Athavale, M. Yoda, Y. Joshi, Thermal Modeling of Data Centers for Control and Energy Usage Optimization, Adv. Heat. Transf., 50 (2018), pp. 123–186

[8] 2015 International Technology Roadmap for Semiconductors (ITRS), Semiconductor Industry Association, Washington, DC 2015

[9] M. Pedram, S. Nazarian, Thermal Modeling, Analysis, and Management in VLSI Circuits: Principles and Methods, Proc. IEEE., 94 (2006), pp. 1487–1501

[10] S.M. Sohel Murshed, C.A. Nieto de Castro, A Critical Review of Traditional and Emerging Techniques and Fluids for Electronics Cooling, Renew. Sustain. Energy Rev., 78 (2017), pp. 821–833

[11] X. Moya, S. Kar-Narayan, N. D. Mathur, Caloric Materials Near Ferroic Phase Transitions, Nat. Mater., 13 (2014), pp. 439-450

[12] S. Lu, Q. Zhang, Electrocaloric Materials for Solid-State Refrigeration, Adv. Mater., 21 (2009), pp. 1983–1987

[13] J. Mao, G. Chen, Z. Ren, Thermoelectric Cooling Materials, Nat. Mater., 20 (2020), pp.454–461

[14] A. Mischenko, Q. Zhang, J. F. Scott, R. W. Whatmore, N. D. Mathur, Giant Electrocaloric Effect in Thin-Film $PbZr_{0.95}Ti_{0.05}O_3$, Science, 311 (2006), pp. 1270-1271

[15] J.F. Scott, Electrocaloric Materials, Annu. Rev. Mater. Res., 41 (2011), pp. 229–240

[16] E. Defay, R. Faye, G. Despesse, H. Strozyk, D. Sette, S. Crossley, X. Moya, N. D. Mathur, Enhanced Electrocaloric Efficiency via Energy Recovery, Nat. Commun., 9 (2018), Article 1827

[17] S.G. Lu, B. Rožič, Q.M. Zhang, Z. Kutnjak, X. Li, E. Furman, L.J. Gorny, M. Lin, B. Malič, M. Kosec, R. Blinc, R. Pirc, Organic and Inorganic Relaxor Ferroelectrics with Giant Electrocaloric Effect, Appl. Phys. Lett., 97 (2010), Article 162904

[18] B. Cantor, I.T.H. Chang, P. Knight, A.J.B. Vincent, Microstructural Development in Equiatomic Multicomponent Alloys, Mater. Sci. Eng. A., 375–377 (2004), pp. 213–218

[19] J.W. Yeh, S.K. Chen, S.J. Lin, J.Y. Gan, T.S. Chin, T.T. Shun, C.H. Tsau, S.Y. Chang, Nanostructured High-Entropy Alloys with Multiple Principal Elements: Novel Alloy Design Concepts and Outcomes, Adv. Eng. Mater., 6 (2004) pp. 299–303

[20] C.M. Rost, E. Sachet, T. Borman, A. Moballegh, E.C. Dickey, D. Hou, J.L. Jones, S. Curtarolo, J.-P. Maria, Entropy-Stabilized Oxides, Nat. Commun., 6 (2015), Article 8485

[21] D. Bérardan, S. Franger, D. Dragoe, A.K. Meena, N. Dragoe, Colossal Dielectric Constant in High Entropy Oxides, Phys. Status Solidi Rapid Res. Lett., 10 (2016) pp. 328–333

[22] D. Bérardan, S. Franger, A. K. Meena, N. Dragoe, Room Temperature Lithium Superionic Conductivity in High Entropy Oxides, J. Mater. Chem. A. Mater., 4 (2016), pp. 9536–9541

[23] J. Gild, M. Samiee, J. Braun, J. L. Braun, T. Harrington, H. Vega, P. E. Hopkins, K. Vecchio, J. Luo, High-Entropy Fluorite Oxides, J. Eur. Ceram. Soc., 38 (2018), pp. 3578-3584

[24] A. Sarkar, B. Breitung, H. Hahn, High Entropy Oxides: The Role of Entropy, Enthalpy and Synergy, Scr. Mater., 187 (2020), pp. 43–48

[25] Y. Pu, Q. Zhang, R. Li, M. Chen, X. Du, S. Zhou, Dielectric Properties and Electrocaloric Effect of High-Entropy $(Na_{0.2}Bi_{0.2}Ba_{0.2}Sr_{0.2}Ca_{0.2})TiO_3$ Ceramic, Appl. Phys. Lett., 115 (2019), Article 223901

[26] W. Liu, F. Li, G. Chen, G. Li, H. Shi, L. Li, Y. Guo, J. Zhai, C. Wang, Comparative Study of Phase Structure, Dielectric Properties and Electrocaloric Effect in Novel High-Entropy Ceramics, J. Mater. Sci., 56 (2021), pp. 18417–18429

[27] S. Wei, X. Chen, G. Dong, L. Liu, Q. Zhang, B. Peng, Large Electrocaloric Effect in Two-Step-SPS Processed $Pb(Sc_{0.25}In_{0.25}Nb_{0.25}Ta_{0.25})O_3$ Medium-Entropy Ceramics, Ceram. Int., 48 (2022), pp. 15640–15646

[28] X. Qian, D. Han, L. Zheng, J. Chen, M. Tyagi, Q. Li, F. Du, S. Zheng, X. Huang, S. Zhang, J. Shi, H. Huang, X. Shi, J. Chen, H. Qin, J. Bernholc, X. Chen, L.Q. Chen, L. Hong, Q.M. Zhang, High-Entropy Polymer Produces a Giant Electrocaloric Effect at Low Fields, Nature, 600 (2021), pp. 664–669

[29] D.J. Singh, M. Ghita, S. v. Halilov, M. Fornari, The Role of Pb in Piezoelectrics and Possible Substitutions for it, J. Phys. IV., 128 (2005), pp. 47–53

[30] R.E. Cohen, Origin of Ferroelectricity in Perovskite Oxides, Nature, 358 (1992), pp. 136–138

[31] S.L. Swartz, T.R. Shrout, Fabrication of Perovskite Lead Magnesium Niobate, Mater. Res. Bull., 17 (1982), pp. 1245–1250

[32] T. Borman, W. Zhu, K. Wang, S. W. Ko, P. Mardilovich, S. E. Trolier-McKinstry, Effect of Lead content on the Performance of Niobium-doped {100} Textured Lead Zirconate Titanate Films, J. Am. Ceram. Soc., 100 (2017), pp. 3558–3567

[33] W. Zhu, B. Akkopru-Akgun, J. I. Yang, C. Fragkiadakis, K. Wang, S. W. Ko, P. Mardilovich, S. Trolier-McKinstry, Influence of Graded Doping on the Long-Term Reliability of Nb-doped Lead Zirconate Titanate Films, Acta Mater., 219 (2021), Article 117251

[34] Y. Liu, J.F. Scott, B. Dkhil, Direct and Indirect Measurements on Electrocaloric Effect: Recent Developments and Perspectives, Appl. Phys. Rev., 3 (2016), Article 031102

[35] J. B. Nelson, D. P. Riley, An Experimental Investigation of Extrapolation Methods in the Derivation of Accurate Unit-Cell Dimensions of Crystals, Proc. Phys. Soc., 57 (1945), pp. 160-177

[36] H. S. Brault, M. Jansen, Properties and High-Pressure Behavior of a Ternary Lead Oxide Pb_2MnO_4, Solid State Sci., 13 (2011), pp. 326-330

[37] R. D. Shannon, Revised Effective Ionic Radii and Systematic Studies of Interatomic Distances in Halides and Chalcogenides, Acta Crystallogr. Sect. A., 32 (1976), pp. 751-767

[38] L. X. He, C. E. Li, Effects of Addition of MnO on Piezoelectric Properties of Lead Zirconate Titanate, J. Mater Sci., 35 (2000), pp. 2477–2480

[39] G. R. Li, L. Y. Zheng, Q. R. Yin, B. Jiang, W. W. Cao, Microstructure and Ferroelectric Properties of MnO_2 -doped Bismuth-layer (Ca,Sr) $Bi_4Ti_4O_{15}$ Ceramics, J. Appl. Phys., 98 (2005), Article 064108

[40] F. Li, S. Zhang, D. Damjanovic, L. Q. Chen, T.R. Shrout, Local Structural Heterogeneity and Electromechanical Responses of Ferroelectrics: Learning from Relaxor Ferroelectrics, Adv. Funct. Mater., 28 (2018). Article 1801504

[41] C.A. Randall, A.S. Bhalla, T.R. Shrout, L.E. Cross, Classification and Consequences of Complex Lead Perovskite Ferroelectrics with regard to B-site Cation Order, J. Mater. Res., 5 (1990), pp. 829–834

[42] J.F. Scott, Ferroelectrics Go Bananas, J. Phys. Condens. Matter., 20 (2008), Article 021001

[43] S. Martin, N. Baboux, D. Albertini, B. Gautier, A New Technique based on Current Measurement for Nanoscale Ferroelectricity Assessment: Nano-Positive Up Negative Down, Rev. Sci. Instrum., 88 (2017), Article 023901

[44] R.A. Cowley, S.N. Gvasaliya, S.G. Lushnikov, B. Roessli, G.M. Rotaru, Relaxing with Relaxors: A Review of Relaxor Ferroelectrics, Adv. Phys., 60 (2011), pp. 229–327

[45] B. Peng, T. Wang, L. Liu, X. Chen, J. Li, Q. Zhang, R. Yang, W. Sun, Z.L. Wang, P-GaN-substrate Sprouted Giant Pure Negative Electrocaloric Effect in Mn-doped $Pb(Zr_{0.3}Ti_{0.7})O_3$ Thin Film with a Super-Broad Operational Temperature Range, Nano Energy, 86 (2021), Article 106059

[46] J. Li, J. Li, S. Qin, X. Su, L. Qiao, Y. Wang, T. Lookman, Y. Bai, Effects of Long- and Short-Range Ferroelectric Order on the Electrocaloric Effect in Relaxor Ferroelectric Ceramics, Phys. Rev. Applied., 11 (2019), Article 44032

[47] M. V. Gorev, I. N. Flerov, V.S. Bondarev, P. Sciau, Heat Capacity Study of Relaxor $PbMg_{1/3}Nb_{2/3}O_3$ in a Wide Temperature Range, J. Exp. Theor. Phys., 96 (2003), pp. 531–537

[48] B. Peng, H. Fan, Q. Zhang, A Giant Electrocaloric Effect in Nanoscale Antiferroelectric and Ferroelectric Phases Coexisting in a Relaxor $Pb_{0.8}Ba_{0.2}ZrO_3$ Thin Film at Room Temperature, Adv. Funct. Mater., 23 (2013), pp. 2987–2992

[49] G. Chen, Y. Zhang, X.M. Chu, G. Zhao, F. Li, J. Zhai, Q. Ren, B. Li, S. Li, Large Electrocaloric Effect in La-doped $0.88Pb(Mg_{1/3}Nb_{2/3})O_3$-$0.12PbTiO_3$ Relaxor Ferroelectric Ceramics, J. Alloys. Compd., 727 (2017), pp. 785–791

[50] J. Hagberg, A. Uusimäki, H. Jantunen, Electrocaloric Characteristics in Reactive Sintered $0.87Pb(Mg_{1/3}Nb_{2/3})O_3$–$0.13PbTiO_3$, Appl. Phys. Lett., 92 (2008), Article 132909

2.6. Supplementary Material for Chapter 2

Figure 2. S1 represents the calcination steps for the Mn B-site precursor (Figure 2.S1A) and Al B-site precursor (Figure 2.S1B), respectively, from 1000℃ to 1400℃. To describe the reaction occurring during the calcination steps, columbite (Mn and Nb based), monoclinic ZrO_2, and cubic $Hf_{0.5}Zr_{0.5}O_2$ peaks are marked with green, blue, and red for Mn B-site precursor and monoclinic ZrO_2/HfO_2, tetragonal rutile, and orthorhombic $Zr_{0.3}Ti_{0.7}O_2$ peaks are marked with pink, blue, and green for Al B-site precursor, respectively. For the Mn-precursor at 1000℃, there are clear monoclinic ZrO_2 peaks, indicating unreacted ZrO_2. The highest intensity peak corresponds to cubic $Hf_{0.5}Zr_{0.5}O_2$ for powder calcined at 1000℃. With increasing temperature, the monoclinic ZrO_2 peaks and cubic $Hf_{0.5}Zr_{0.5}O_2$ are diminished and decreased; columbite peaks emerge and become the highest intensity peaks. However, it is also possible that the cubic $Hf_{0.5}Zr_{0.5}O_2$ can be

shifted toward lower angles, meaning that reactions reduce the lattice constant of cubic $Hf_{0.5}Zr_{0.5}O_2$. With further increase in temperature from 1200℃ to 1400℃, the number of small peaks between 40° and 60° reduced, and the peaks became sharper. Similar behavior is observed for the Al B-site precursors; the monoclinic ZrO_2/HfO_2 disappeared with increasing temperature and the number of peaks decreased over the entire range. The orthorhombic $Zr_{0.3}Ti_{0.7}O_2$ peaks dominate the phase at 1400℃.

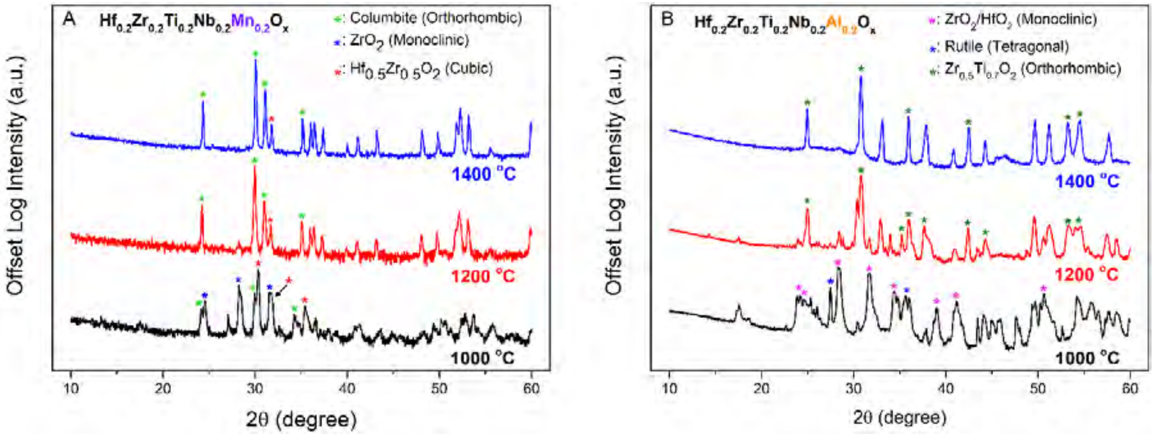

Figure 2.S1. X-ray diffraction of B-site precursors of A) Mn-precursors and B) Al-precursors after heat treatments from 1000℃ to 1400℃ for 240 minutes. Peaks are identified based on the most plausible combination of the compositions.

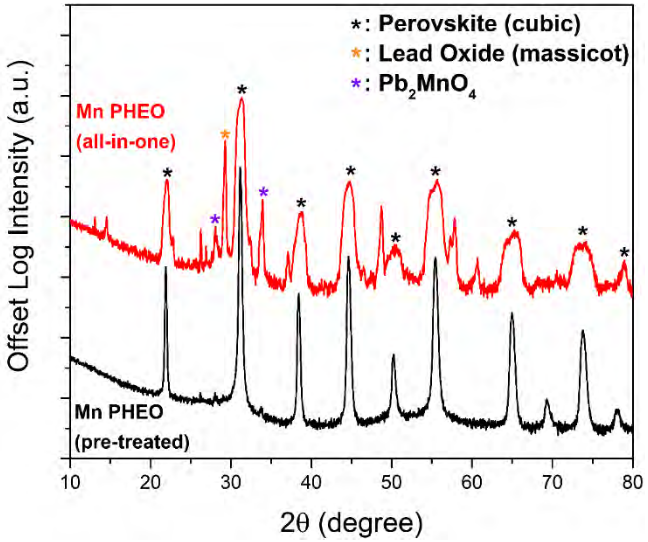

Figure 2.S2. X-ray diffraction of heat treatments on Mn PHEO powder without B-site pre-treatment (red) and with B-site pre-treatment (black) for 4 hours at 800℃. Without the B-site pre-treatment, phase pure Mn PHEO powder is not obtained at the same temperature.

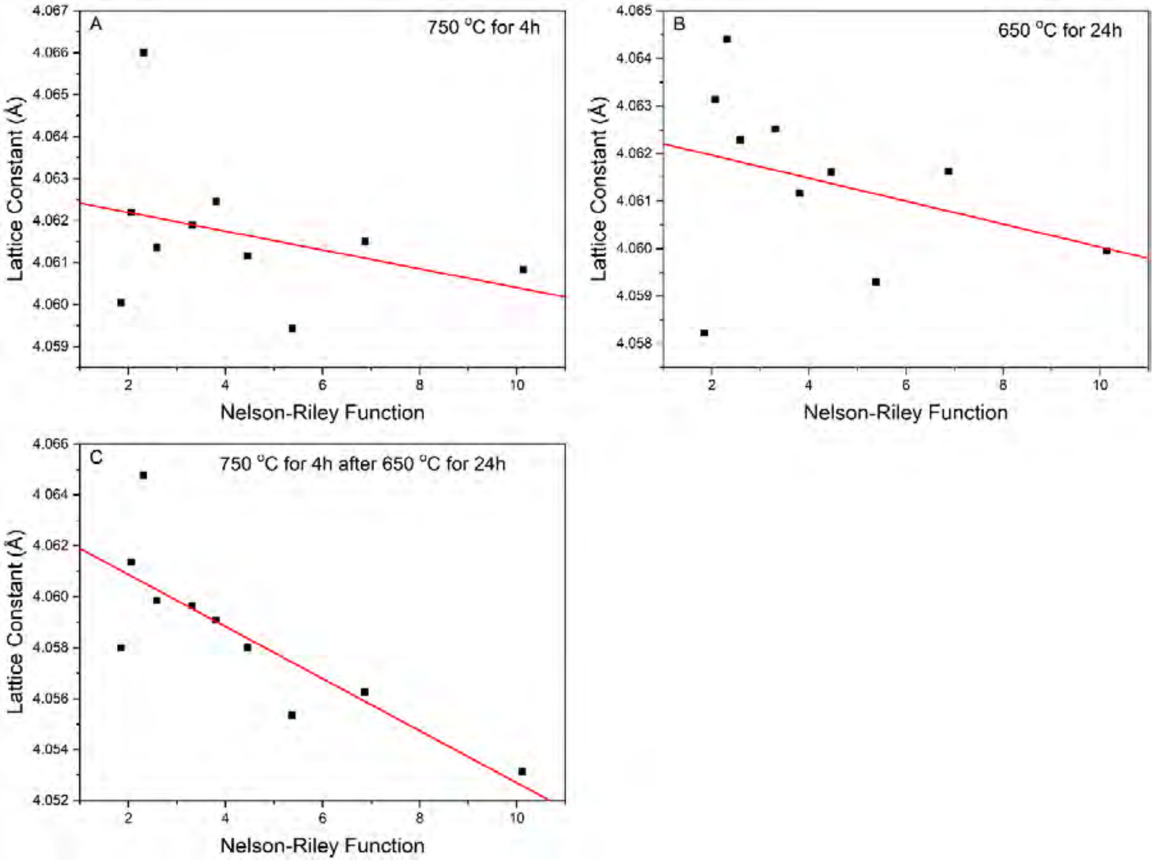

Figure 2.S3 Lattice constants of Mn PHEO powders determined using the Nelson-Riley function for powders heated at A) 750℃ for 4 hours, B) 650℃ for 24 hours after 750℃ for 4 hours, and C) 750℃ for 4 hours after 650℃ for 24 hours.

Table 2.S1. Lattice constants of Mn PHEO using the Nelson-Riley function for powders heated at A) 750℃ for 4 hours, B) 650℃ for 24 hours after 750℃ for 4 hours, and C) 750℃ for 4 hours after 650℃ for 24 hours.

	(A)	(B)	(C)
Lattice Constant (Å)	4.0628±0.0011	4.0624±0.0012	4.0629 ± 0.0013

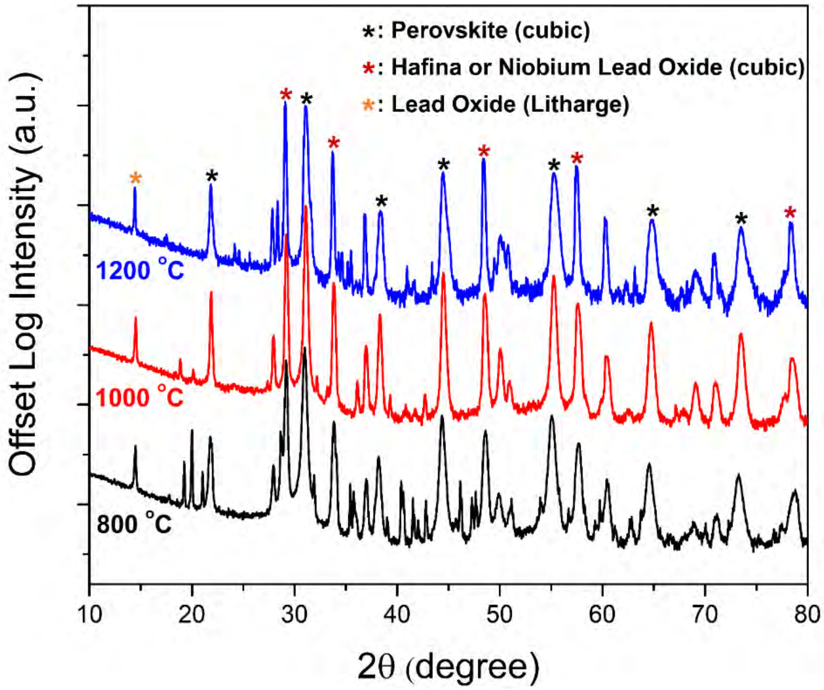

Figure 2.S4 Heat treatments on Al PHEO powder from 800℃ to 1200℃. Single-phase is not achieved even for heat treatment at 1200℃.

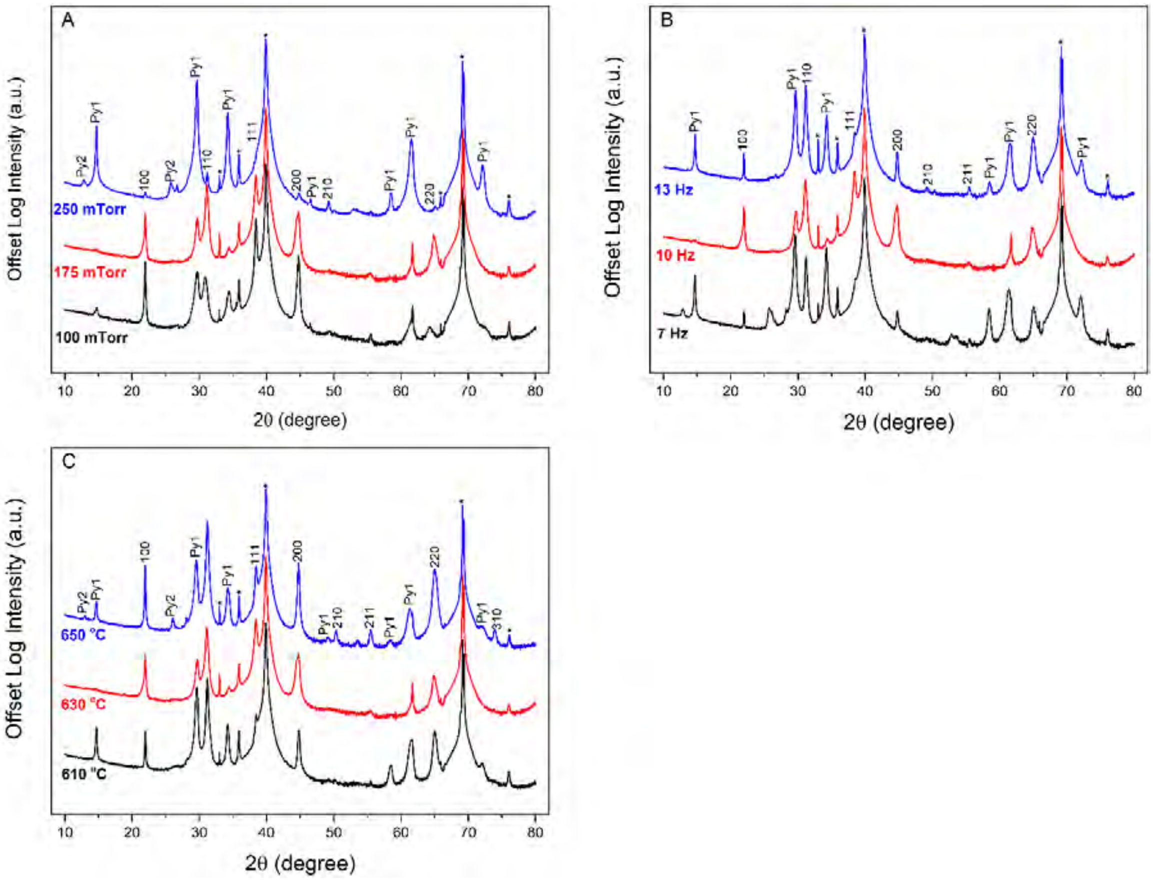

Figure 2.S5. A) XRD patterns of varying deposition pressure from 250 mTorr to 100 mTorr, B) laser frequency from 10 Hz to 7 Hz, and C) substrate temperature from 650℃ to 610℃ to find out best processing window of Mn PHEO on Pt/Ti/SiO_2/Si substrates.

First, the (O_3/O_2) deposition pressure (10%/90%) was varied from 100 mTorr to 250 mTorr. The substrate temperature and laser repetition rate were fixed at 630℃ and 10 Hz, respectively. Figure 2.S5A shows XRD scans of Mn PHEO on platinized silicon changing for deposition pressure of 250 mTorr (Blue), 175 mTorr (red), and 100 mTorr (black). The asterisk (*) indicates peaks from the substrate and from other wavelengths from the X-ray source; the perovskite peaks were indexed based on $Pb(Zr_{0.4}Ti_{0.6})O_3$. Two different pyrochlore phases were detected. Py1 was fitted using data for $Pb_2Ti_{0.67}Nb_{1.33}O_{6.67}$, while Py2 was fitted based on $Pb_{2-x}Mn_8O_{16}$. The Py2 peaks are most intense for depositions at high pressures, but disappear for deposition pressures lower than 175 mTorr. Interestingly, the Py1 peak at 14.5°diminished with lowering pressure from 250 mTorr, but reoccurred at 100 mTorr.

Figure 2.S5B shows XRD scans of films grown varying laser frequency from 13 Hz to 7 Hz. With a 10 Hz laser frequency, the Py1 and Py2 peaks are not detected at a low angle (~ 13° degree) and the other pyrochlore peaks are minimized. At 7 Hz, Py2 is clearly identified at a low angle, but not at 13 Hz. Given that low laser frequencies allow more PbO volatility from the growing film, Py2 is a Pb-deficient and Py1 is a Pb-rich pyrochlore phase, respectively.

Lastly, the substrate temperature was varied from 610℃ to 650℃ at 20℃ intervals as shown in Figure S5C. It is notable that at 610℃, the Py2 peak receded while Py1 peaks emerged. At 630℃, the smallest pyrochlore peak intensities are observed over the entire scan range. At 650℃, the Py1 peak at low angle recurred and a small Py2 peak also emerged. This behavior confirms that Py1 is correlated with Pb-rich pyrochlore while Py2 is Pb-deficient.

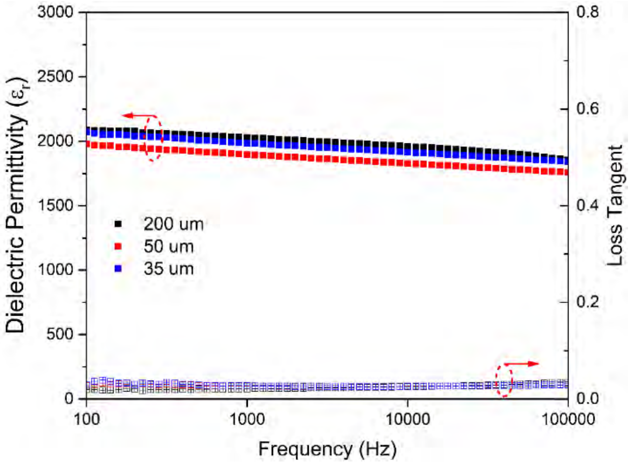

Figure 2.S6. Dielectric properties of Al PHEO varying the size of top electrode. Size-independent of dielectric properties of Al PHEO indicates successful top electrode fabrication.

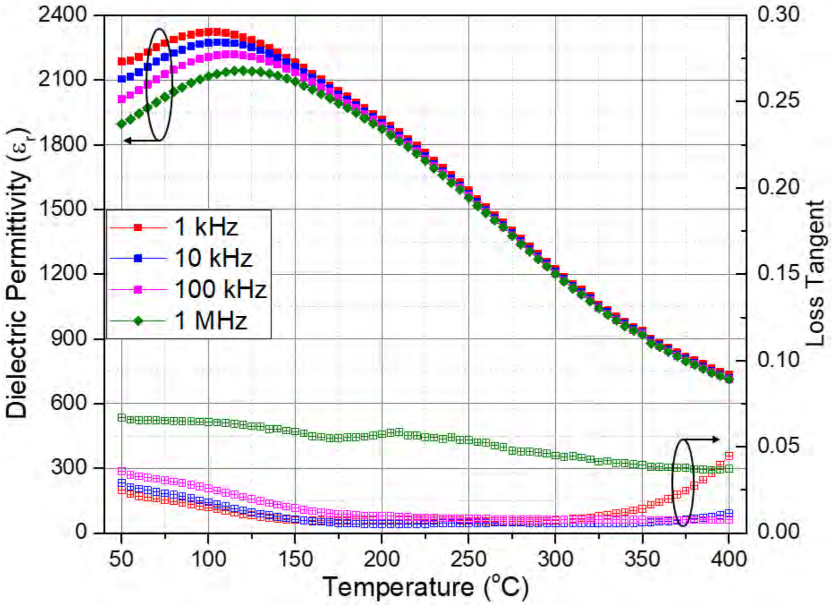

Figure 2.S7. Dielectric permittivity vs temperature of another Al PHEO film. This sample shows very clear frequency dispersion below the dielectric maxima (105℃).

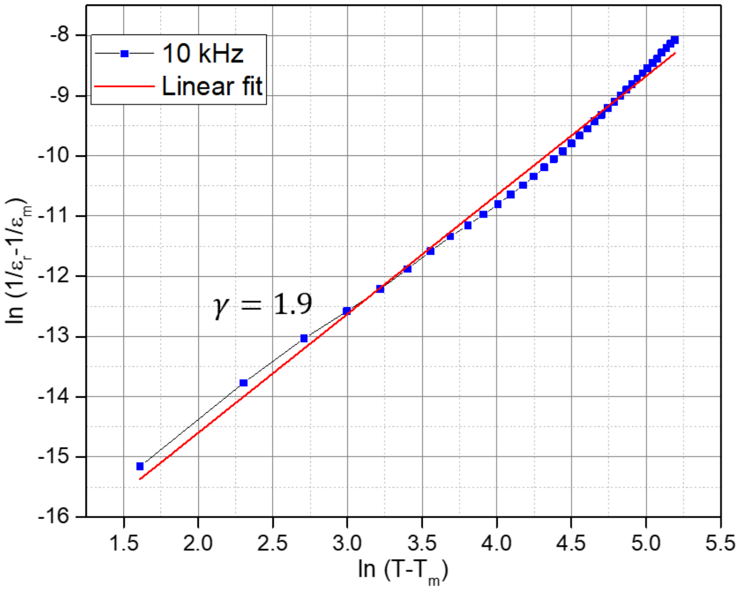

Figure 2.S8. The result of modified Curie-Weiss law with relaxation parameter of 1.9. The 10 kHz data are shown.

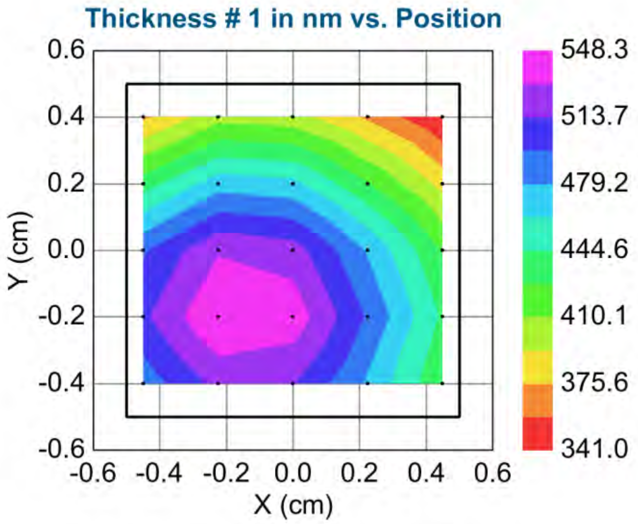

Figure 2.S9. Ellipsometry mapping of Al PHEO film on PNZT seed layer to measure the thickness. Electrical measurements were performed based on electrodes in the purple area to minimize errors from variation in the thickness.

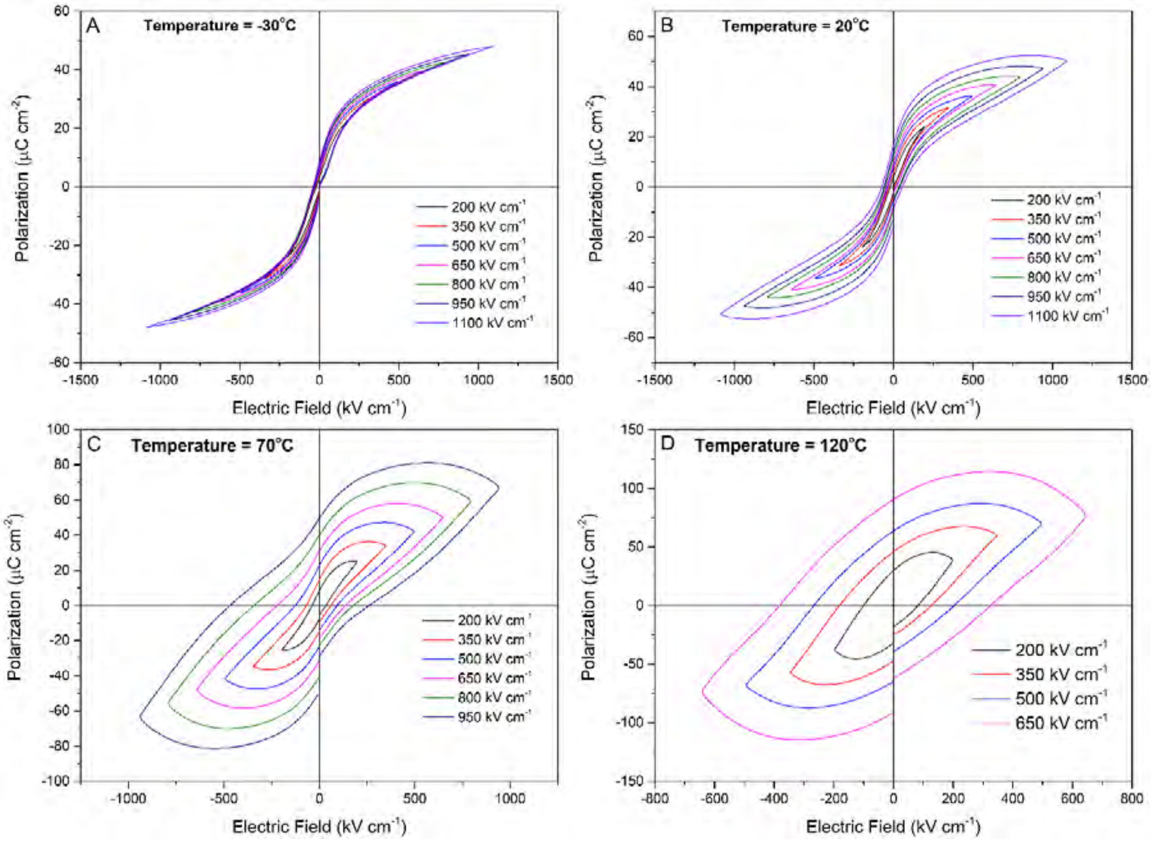

Figure 2.S10. Nested ferroelectric P-E loops of a Mn PHEO film A) at -30℃, B) at 20℃, C) at 70℃, and D) at 120℃. Except for the P-E loops measured at -30℃, all loops are bloated, and would lead to overstating the apparent remanent polarization.

Chapter 3

Polarization Stability and its Influence on Electrocaloric Effects of High Entropy Perovskite Oxide Films

Chapter 3 of this dissertation has been submitted to *Acta Materialia;* Y. Son, S. Udovenko, S. V. G. Ayyagari, J. Barber, K. Nakamura, C. M. Rost, N. Alem, S. Trolier-McKinstry, Polarization Stability and Its Influence on Electrocaloric Effects of High Entropy Perovskite Oxide Films (under review)

3.1 Introduction

The electrocaloric effect (ECE) describes the adiabatic temperature change observed in ferroelectric materials originating from the entropy change associated with electric field-induced polarization [1]. Since the discovery of large ECE in 2006, the phenomenon has garnered increased attention as a potential approach for energy-efficient cooling [2]. Thermodynamic simulations suggest that cooling devices utilizing the ECE exhibit superior coefficients of performance relative to mechanical vapor compression coolers, and can achieve a Carnot efficiency exceeding 60% [3]. Numerous studies have explored electrocaloric materials for the development of advanced cooling devices such as on-chip cooling and battery thermal management systems [4–6]. For this technology to become practical, it will need to enable usefully large adiabatic temperature changes (ΔT), reduced driving electric field (E) to enable adequate cycling reliability, and a broad working temperature range (T_{span}) [7].

Recently, multilayer ceramic capacitor-based electrocaloric prototypes have shown directly measured electrocaloric temperature changes of 5.5 K and a working temperature range of 13 K [8,9]. More specifically, harnessing ferroelectric-to-ferroelectric field induced phase transitions has emerged as a promising approach. Relaxor ferroelectrics are also of interest for ECE applications due to large dipole entropy associated with Nano-Polar Regions (NPRs) [10–14]. Relaxors are typically characterized by short range ordering on one of the cation sites, as has been previously shown in ABO_3 perovskites [15,16]. However, in some cases, the processing of relaxor materials is complicated by relatively poor phase stability, which carries associated difficulties in processing and reproducibility.

The use of configurational entropy to thermodynamically stabilize solid solutions has garnered considerable attention since the discovery of high entropy alloys in 2004 [17,18]. In 2015, $Mg_{0.2}Ni_{0.2}Co_{0.2}Cu_{0.2}Zn_{0.2}O$ was identified as a model rocksalt Entropy-Stabilized Oxide (ESO) [19]. High Entropy Oxide (HEO) is more general term to describe multicomponent systems with near equimolar amounts; ESO, which requires demonstration that a reversible phase transition can be driven by entropy are a subset of HEO [20,21]. Numerous attempts to understand the fundamental properties of these materials and to fabricate new HEOs with different crystal structures have been established. The structural disorder induced by the presence of multiple cations with different sizes and charges on a single lattice site has been shown to benefit various applications as catalysts, capacitors, thermal barriers, batteries, and more. [22–27].

There are four principle influences that high entropy can have on materials, namely high-entropy, lattice distortion, slow diffusion, and cocktail effects [28]. It is speculated that HEO-type materials may enhance the ECE, given that cooperative phenomena such as the polar order inherent to ferroelectricity can be affected by HEO-like formulations, especially through the local structural distortion and the cocktail effect. More specifically, the complex compositions of HEOs are expected to introduce a competition between long-range polar order and local fluctuations due to different atomic sizes and propensities for the displacement from the center of the B-site octahedra. That is, local structural distortion should produce the type of random-bond, random-fields that favor relaxor ferroelectricity relative to normal ferroelectricity [29,30]. This is turn, should favor polar disorder. This can be augmented by a cocktail effect in which some of the ions favor long range polar order, while others do not. While it is known that for ECE, polar entropy plays a pivotal role; nonetheless, the investigation of ECE of HEOs has been rarely reported [31–34].

This paper represents exploratory research on the effect of HEO-like formulations on the ECE and the stability of the induced polarization with time. To do this, the A-sites and B-sites of an ABO_3 perovskite were individually disordered by introducing 5 different elements, while maintaining charge balance and size compatibility. Pb was used as a fixed A-site element for all B-site disordered compositions and Ti was used as a fixed B-site element for all A-site disordered compositions. Overall, eight different compositions were prepared. Table 3.1 lists the designation and details of each High Entropy Perovskite Oxide (HEPO) composition. Previous work demonstrated that Mn_P was electrically leaky, therefore further investigation was not performed here [34].

Table 3.1. Designation of 8 different HEPO compositions investigated for this study.

Designation	A-site cations	B-site cations
AlP	Pb	$(\mathrm{Ti_{0.2}Zr_{0.2}Hf_{0.2}Nb_{0.2}Al_{0.2}})$
CrP	Pb	$(\mathrm{Ti_{0.2}Zr_{0.2}Hf_{0.2}Nb_{0.2}Cr_{0.2}})$
FeP	Pb	$(\mathrm{Ti_{0.2}Zr_{0.2}Hf_{0.2}Nb_{0.2}Fe_{0.2}})$
MnP	Pb	$(\mathrm{Ti_{0.2}Zr_{0.2}Hf_{0.2}Nb_{0.2}Mn_{0.2}})$
ScP	Pb	$(\mathrm{Ti_{0.2}Zr_{0.2}Hf_{0.2}Nb_{0.2}Sc_{0.2}})$
NaP	$(\mathrm{Bi_{0.2}Ba_{0.2}Sr_{0.2}Ca_{0.2}Na_{0.2}})$	Ti
KP	$(\mathrm{Bi_{0.2}Ba_{0.2}Sr_{0.2}Ca_{0.2}K_{0.2}})$	Ti
PbP	$(\mathrm{Bi_{0.2}Ba_{0.2}Sr_{0.2}Na_{0.2}Pb_{0.2}})$	Ti

3.2 Experimental Procedure

Powder and target preparation: All the investigated compositions were fabricated via conventional solid-state reaction. The raw materials used for this study were all acquired from Sigma Aldrich: Pb_3O_4 (99%), ZrO_2 (99%), TiO_2 (99.8%), HfO_2 (98%), Nb_2O_5 (99.99%), Al_2O_3 (99.99%), Fe_2O_3 (99.995%), Sc_2O_3 (99.9%), Cr_2O_3 (99.9%), Na_2CO_3 (99.5%), Bi_2O_3 (99.999%), $BaCO_3$ (99.98%), $SrCO_3$ (99.9%), $CaCO_3$ (99.9%), K_2CO_3 (99%). For the B-site disordered compositions, all the B-site cation precursors were pre-ball-milled with yttria stabilized zirconia media in ethanol for 24 hours and heat-treated at 1300℃ for 4 hours to homogenize the cation distribution. After adding lead oxide, all the powders were ball-milled again with yttria stabilized zirconia media in ethanol followed by heat treatment at 800℃ for 4 hours to achieve a single phase.

A-site disordered compositions were treated in a different way. No pre-treatments were performed for the A-site precursors due to melting. Instead, A-site precursors were mixed with TiO_2 powder and ball-milled with yttria-stabilized zirconia media in ethanol for 24 hours. Calcination was performed at 1200°C for Na_P and K_P and 1050℃ for Pb_P for 4 hours, respectively. After the calcination, 20 mole% excess lead oxide, 1 mole% excess sodium, potassium, and bismuth oxide powder were added to the powder batch to compensate for potential loss of those atoms either during the target processing or during subsequent film growth under vacuum. The powders were vibratory milled with the zirconia media using ethanol for 24 hours. Then, the powders were uniaxially pressed into 1-inch in die under 44 MPa, followed by Cold Isostatic Pressing (CIP) at a pressure of 207 MPa for 1 min. Finally, the pressed ceramic pellets were heat treated at different temperatures from 900°C to 1300°C depending on the compositions. All the prepared targets had a relative density ≥ 94 %.

Deposition of HEPO Films: All deposition of HEPO films was carried out using a custom Pulsed Laser Deposition (PLD) system equipped with 248 nm KrF (102F, Coherent) and (100) $SrRuO_3/SrTiO_3$ crystal substrates (MSE supplies). Prior to the deposition of the $SrRuO_3$ film, a $SrTiO_3$ substrate was chemically etched with buffered-hydrofluoric acid followed by annealing at 1200°C for 30 min to obtain an atomically smooth surface. A ceramic target of $SrRuO_3$ was purchased from Kojundo, Co, Ltd. Details for the processing parameters and the quality of the $SrRuO_3/SrTiO_3$ are shown in the supplementary material.

All HEPO film depositions were conducted after growth of the $SrRuO_3$ bottom electrode without breaking the vacuum. For the B-site disordered HEPO film, a laser energy of 1.5 J cm^{-2}, a working distance of 6.2 cm, a laser frequency of 6 Hz, an oxygen deposition pressure of 70 mTorr, and a substrate temperature of 595℃ were used. After the deposition, all the films were immediately removed from the heater to avoid loss of volatile species during the cooling process.

Deposition of $PbZr_{0.52}Ti_{0.48}O_3$ film: A commercial solution (PZT-E1, Mitsubishi Materials Corporation, Hyogo, Japan) was used to deposit a PZT film on a Pt-coated SiO_2/Si wafer (NOVA Wafers) by spin coating. The solution was batched with 14 mol% excess Pb, Zr/Ti = 52/48, and 2 % Nb on the B-site. The solution was first dispensed onto the substrate, then spun at 3000 rpm for 45 s, dried at 100℃ for 1 min, pyrolyzed at 400℃ for 4 min, and crystallized in a rapid thermal annealer (RTA) ramping for 40 s from 300℃ to 700℃ with an oxygen partial pressure at 2 standard liters per minute (SLPM). The process was repeated 9 times to achieve a thickness of 770 nm. The processing and quality of the PZT film are described in details elsewhere [35].

Capacitor fabrication: 100 nm thick platinum (Pt) top electrodes were sputter-deposited (CMS-18 sputter system, Kurt J. Lesker Company, Pittsburgh, PA) over the photolithographically-defined double-layer resist stack followed by lift-off. After lift-off, RTA at 500℃ for 15 min was performed in air to promote adhesion between the Pt electrode and the HEPO films.

Structural Characterization: The structural phase and crystallographic orientation of the HEPO powders at room temperature were examined using a PANalytical Empyrean diffractometer with Cu Kα X-ray radiation. Temperature-dependent X-ray diffraction (XRD) data were collected using a PANalytical Empyrean diffractometer and a PANalytical X'Pert Pro MPD equipped with temperature stage HTK 1200 and TTK-450, respectively, both with Cu Kα X-ray radiation, from room temperature to 400℃. The structural quality of the HEPO films was assessed using a 4-circle high-resolution XRD

(Malvern Panalytical-MRD) equipped with a hybrid Ge (220) 2-bounce monochromator and a multilayer mirror for 2Theta and rocking curves or X-ray reflectivity (XRR), respectively, using Cu Kα X-ray radiation. Transmission electron microscopy (TEM) samples were prepared using the FEI Helios 660 Dual Beam Focused Ion Beam (FIB). The FIB lamellae were thinned down at 5 kV followed by 2 kV to reduce FIB induced surface damage. Selected area electron diffraction (SAED), and X-ray energy dispersive spectroscopy (XEDS) experiments were performed on the FEI Talos 200X at an accelerating voltage of 200 kV. X-ray photoelectron spectroscopy (XPS; Physical Electronics VersaProbe III) was performed using a monochromatic Al Kα X-ray source and a concentric hemispherical analyzer. Charge neutralization was performed using both low energy electrons (<5 eV) and argon ions. The binding energy axis was calibrated using sputter cleaned Cu (Cu $2p_{3/2}$ = 932.62 eV, Cu $3p_{3/2}$ = 75.1 eV) and Au foils (Au $4f_{7/2}$ = 83.96 eV). Peaks were charge referenced to Pb^{2+} band in the Pb 4f spectra at 138.2 eV. Measurements were made at a takeoff angle of 90° with respect to the sample surface plane. This resulted in a typical sampling depth of 5-7 nm (95% of the signal originated from this depth or shallower). Quantification was done using instrumental relative sensitivity factors (RSFs) that account for the x-ray cross section and inelastic mean free path of the electrons. The analysis size was ~200 μm in diameter.

Electrical characterization: The dielectric properties of the films were measured using an HP 4284 LCR meter coupled with a FormFactor 11000 probe station. An applied voltage 30 mV and a frequency range from 100 Hz to 100 kHz were used. Polarization-Electric field hysteresis loops (P-E loops) were measured using a Precision Multiferroic Tester (Radiant Technologies) using a bipolar triangular waveform. Leakage current densities of the films were measured by 4140 pico-Ampere meter/DC voltage source with a FormFactor 11000 probe station. Positive-Up-Negative-Down (PUND) measurements were performed using the Precision Multiferroic Tester varying parameters of pulse amplitude (voltage) and delay time. A customized PUND voltage profile was generated using MATLAB and executed using the same tester.

3.3 Results and Discussion

3.3.1 Structure of High Entropy Perovskite Oxide Powders and Films

3.3.1.1 High Entropy Perovskite Oxide Powders

As was discussed in the experimental procedure section, depending on the intended stoichiometry, different synthesis strategies were employed for the successful development of the perovskite phase in powders. For the synthesis of the B-site disordered compositions, B-site pre-treatment via a columbite-like route was adapted to discourage formation of the pyrochlore phase during synthesis [36]. It was previously reported that this approach can be applied to HEO-like compositions with compositional disorder on the B-site of the perovskite [34]. With this synthesis method, all B-site HEPO powders were prepared at temperatures ≤ 800℃. However, the same technique could not be used for the A-site disordered compositions with potassium, sodium, lead, and bismuth, because the precursors melted during pre-treatment steps, even at a temperature of 600℃. Therefore, the calcination temperature was increased to 1200℃ to stabilize the perovskite phase without homogenizing the A-site powders. The increased temperature compensates for the larger diffusion length required for the non-pre-treated A-site precursors.

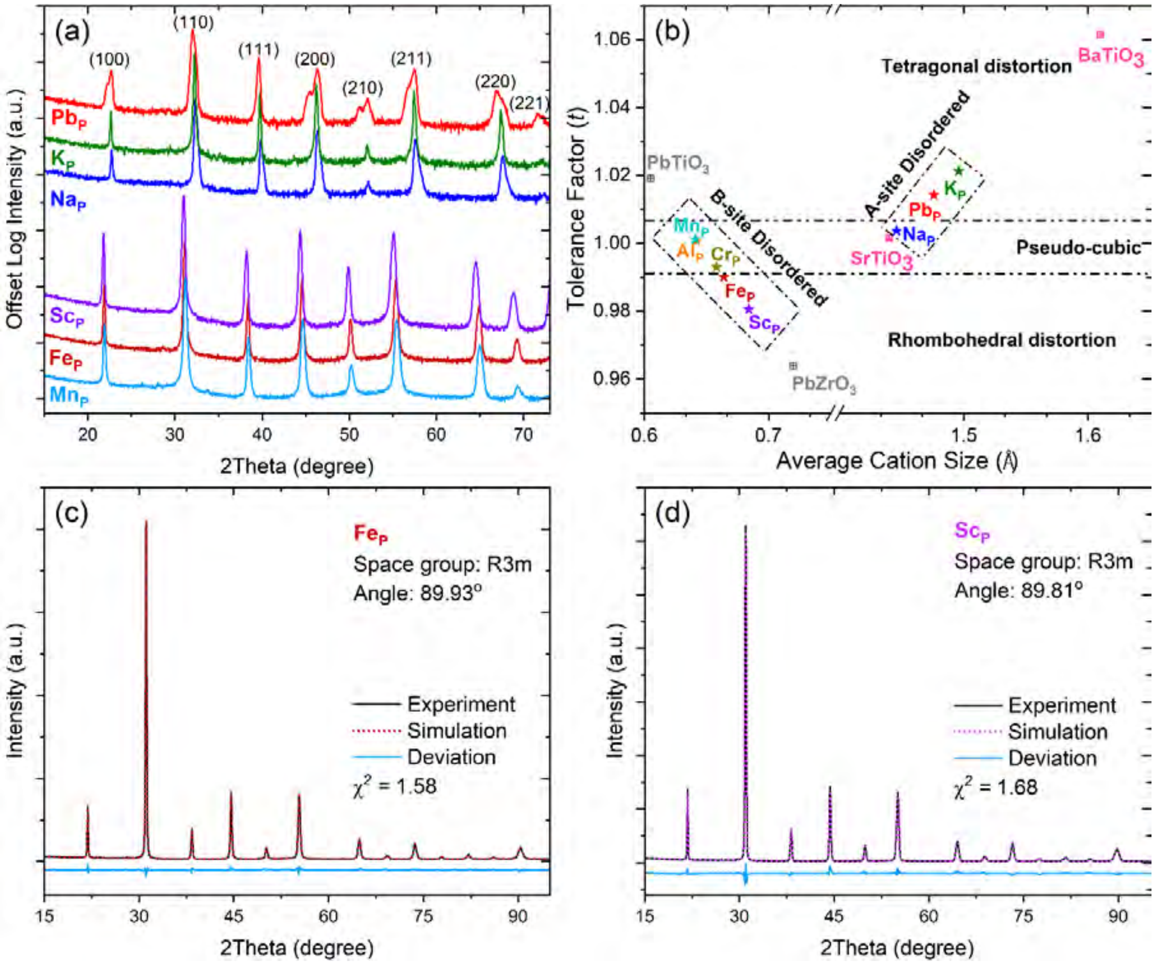

Figure 3.1. X-ray diffraction patterns of (a) HEPO powders that form a single perovskite phase, (b) Goldschmidt's tolerance factor versus cation size maps of all HEPO with several well-known perovskite materials, (c) Rietveld refinement of Fe_P powder, and (d) Sc_P powder. Refinement revealed rhombohedral distortion with α = 89.93° and 89.81° for the Fe_P and Sc_P powders, respectively.

Figure 3.1(a) shows the XRD patterns of all HEPO powders that formed single perovskite phases. However, despite the pre-treatment steps, Al_P and Cr_P powder were reluctant to form a single phase as shown in Figure 3.S1 in the supplementary material.

The lattice parameters of the B-site HEPO powders were larger than those of the A-site HEPOs, which was attributed to the larger averaged B-site cation sizes compared to Ti (0.605 Å) as well as the similar or smaller size of A-site cations than Pb. This also has implications in terms of the stability of the perovskite phase and any anticipated distortions to the perovskite structure, as is expected based on Goldschmidt's tolerance factor [37]. The tolerance factor was calculated via:

$$\mathrm{t\ (tolerance\ factor)} = \frac{r_A + r_X}{\sqrt{2}(r_B + r_X)}$$

where r_A is the average radius of the cations on the A-site, r_B is the average radius of the cations on the B-site, and r_X is the radius of the anion [38]; Shannon-Prewitt ionic radii were utilized [38]. Figure 3.1(b) presents a map of the tolerance factor as a function of averaged disordered cation size of the eight different HEPO compositions investigated in this study. Several well-known perovskite materials such as $PbTiO_3$, $PbZrO_3$, $SrTiO_3$, and $BaTiO_3$ are shown for comparison.

Table 3.2 shows the achievability of single phase, the powder lattice parameter, and Goldschmidt's tolerance factor. Previously, it was suggested that HEPO materials with a tolerance factor of $0.97 \leq t \leq 1.03$ are readily prepared as a perovskite single phase [27,39]. This agrees well with the investigation. However, Al_P and Cr_P are exceptions. It is not clear whether the failure to achieve a single phase in Al_P and Cr_P powders is due to either a relatively large enthalpic contribution which exceeds the phase stabilization of the entropic contribution at the processing conditions or to kinetic limitations associated with sluggish diffusion of the given compositions.

Many HEPO compositions had pseudo-cubic-like XRD patterns. However, the doublet in the {200} family peaks for Pb_P suggests a tetragonal distortion. This is consistent with the observation that the perovskite tolerance factor exceeds 1 [40]. Figure 3.S4(b) shows the result of the temperature dependent XRD for the Pb_P powder; a phase transition from tetragonal to cubic occurred around 250°C, which is consistent with previous findings [41]. Given this, it is intriguing that K$_P$ with tolerance factor of 1.02 which is larger than that of Pb$_P$, shows no evidence of the tetragonal structure. It is speculated that this ferroelectric phase transition temperature of K$_P$ is below room temperature, as is the case for $Ba_{0.5}Sr_{0.5}TiO_3$, which has $t = 1.03$ and a phase transition temperature below room temperature [42]. Neither K$_P$ nor Na$_P$ exhibited an obvious phase transition between room temperature and ~ 400℃, as shown in Figure 3.S4(a) and (c).

Fe$_P$ and Sc$_P$ powders were rhombohedrally distorted as evidenced by the Rietveld refinement using JADE (as shown in Figure 3.1(c) and (d), respectively), and by the splitting of the {222} family peaks in Figure 3.S2(a) and (b), respectively). Rhombohedral distortion from the cubic cell is quantified in terms of the deviation of the unit cell angles from 90°. The larger deviation for Sc$_P$ (89.81°) compared to Fe$_P$ (89.93°), is presumably due to the larger average cation size on the B-site decreasing the tolerance factor. It may also indicate larger displacement of the B site cations from the center of the B-site octahedron [43]. The local tolerance factor accounting for individual B-site cations is shown in Figure 3.S5. It is clear that the variation in tolerance factor is larger for Al$_P$ composition than for the other B-site disordered compositions. This implies a larger magnitude of lattice distortion in the Al$_P$ composition.

Figure 3.S3(a) and (b) shows the result of temperature-dependent XRD of the Fe$_P$ and Sc$_P$ powders, respectively, from room temperature to 400℃. With increasing temperature, the intensity of the {311} and {320} family of perovskite peaks decreased, as the crystal symmetry changed from R3m to $Pm\bar{3}m$.

Table 3.2. Achievability of single phase (temperature), lattice constant and tolerance factor of the PHEO powders based on XRD

	Al_P	**Cr_P**	**Fe_P**	**Mn_P**	**Sc_P**	**Na_P**	**K_P**	**Pb_P**
Single Phase (temp.)	No	No	Yes (800°C)	Yes (750°C)	Yes (800°C)	Yes (1200°C)	Yes (1200°C)	Yes (1050°C)
Lattice constant (Å)	N/A	N/A	4.062 ±0.002	4.060 ±0.002	4.078 ±0.002	3.915 ±0.002	3.925 ±0.002	3.913 ±0.002 (a) 3.989 ±0.002 (c)
Tolerance factor	1.000	0.993	0.990	1.001	0.981	1.004	1.021	1.014

3.3.1.2 High entropy Perovskite Oxide Films

A 45 nm thick layer of $SrRuO_3$ was grown on the (100) $SrTiO_3$ substrates prior to the deposition of any of the B-site HEPO films. Detailed processing information for the SRO/STO is discussed in the supplementary material (see Figure 3.S7). All HEPO films were ~300 nm thick as calibrated by XRR (see Figure 3.S13(a)). Figure 3.2(a), shows an enlarged view near the {200} perovskite XRD peaks for the B-site disordered HEPO films. A single-phase Al_P film was achieved, possibly due to either epitaxial stabilization or to the high effective temperature of the plasma in the PLD process, which increased the entropic contribution (relative to Al_P powder processing). In Figure 3.S13(b), an AFM scan displays the surface morphology of the B-site disordered HEPO films.

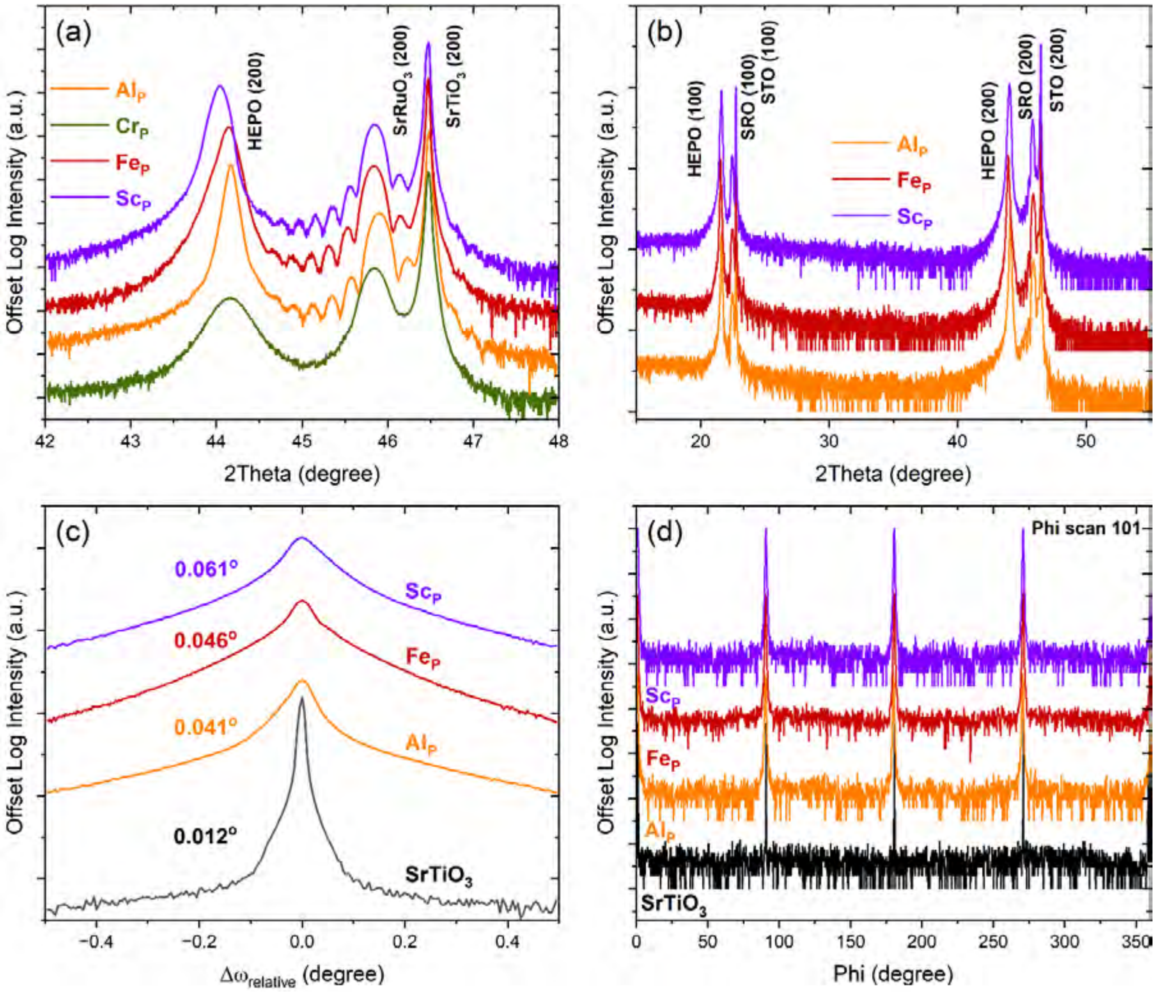

Figure 3.2. XRD of the B-site disordered HEPO, (a) enlarged view near {002} family of the perovskite peaks, (b) wider 2theta scan, (c) rocking curve, and (d) phi scan.

Cr$_P$ did not form a single phase in either a powder or a film. Cr$_P$ films exhibit a large surface roughness, ascribed to $PbCrO_3$ segregation, as seen via XRD (see Figure 3.S13(c)) and Field Emission Secondary Electron Microscopy (FESEM) with Energy Dispersive Spectroscopy (EDS) mapping (Figure 3.S13(d)). The surface roughness of the Cr$_P$ film was associated with a well-organized structure aligned along orthogonal directions on the SRO/STO substrate, as seen in the FESEM image. The structure was confirmed to be predominantly $PbCrO_3$ by EDS, which is consistent with the XRD findings.

Figure 3.2(c) shows the rocking curves of B-site disordered HEPO films (excepting Cr$_P$), where the low full width at half maximum, FWHM (<0.061°) demonstrates good film crystallinity. The FWHM of the B-site disordered HEPO films are compared with several well-known relaxor ferroelectric and other HEPO films in Table 3.S1 of the supplementary material. Figure 3.2(d) shows the Phi scan around (101); a cube-on-cube epitaxial in-plane relationship between the HEPO films and the underlying SRO/STO growth templates can be seen. Table 3.3 shows the lattice constants, FWHM of the rocking curves and film tetragonalities. In-plane lattice constants were determined via $a = 2\sqrt{(d_{101})^2 - (d_{002})^2}$, where d_{hkl} indicates the lattice spacing corresponding to the given hkl [44]. The difference between the lattice constants for powder and deposited Fe$_P$ and Sc$_P$ films may be due to film stress. It should be noted that all the films are likely to be under compressive in-plane strain, which would increase the out-of-plane lattice constant. In Figure 3.S15, the asymmetric XRD scan along (101) is shown. It is noteworthy that the in-plane crystallinity exhibits a lower level of crystal perfection compared to its out-of-plane counterpart. This disparity might be attributed to the more sensitive response for edge dislocations along the in-plane direction [45].

The compositional uniformity of the Al$_P$, Fe$_P$ and Sc$_P$ films were assessed using STEM-EDS as revealed in Figure 3.S10 – Figure 3.S12, respectively. We noted that no evident chemical segregation was confirmed at the given length scale. Note that due to poor reproducibility and large sample-to-sample variation associated with multiple volatile elements in the A-site disordered film, property exploration was performed on the B-site disordered films only. Details of structure, leakage current, dielectric, and ferroelectric properties of the A-site disordered films at room temperature are given in Figure 3.S8 of supplementary material.

Table 3.3. Lattice constants, FWHM, and tetragonality of the B-site HEPO films determined based on symmetric and asymmetric XRD scans.

	Film Lattice constant (Å)	FWHM (°)	Tetragonality (*c*/*a*)
AlP	4.104 ± 0.002 (*c*) 4.032 ± 0.002 (*a*)	0.041	1.02
FeP	4.105 ± 0.002 (*c*) 4.052 ± 0.002 (*a*)	0.046	1.01
ScP	4.109 ± 0.002 (*c*) 4.065 ± 0.002 (*a*)	0.061	1.01
CrP	N/A	N/A	N/A

3.3.2 Electrical Characterizations of the B-site HEPO Films

3.3.2.1 Room-Temperature Dielectric and Ferroelectric Properties

Figure 3.3(a) – (c) shows room-temperature leakage current density, dielectric permittivity, polarization-electric field hysteresis loops (P-E loop) measurements of the HEPO films, respectively. Leakage current measurements, Figure 3.3(a), were made in the field up configuration that caused charge injection from the top Pt electrode. These data were taken with a wait time of 60 seconds after any change in voltage. It is evident that the FeP film had a current density two orders of magnitude higher than the AlP and ScP films. The relatively large leakage of the FeP film was conjectured to be due to charge hopping between multivalent Fe-ions, akin to the behavior observed in MnP [34]. Indeed, XPS of FeP supports the existence of a mixture of Fe^{3+} and Fe^{2+} ions that can induce charge hopping (see Figure 3.S9). In contrast, Al$_{\mathrm{P}}$ and Sc$_{\mathrm{P}}$ films exhibited relatively little electrical conductivity due to the single valence state of the Al and Sc ions. The dielectric permittivity of the Al$_{\mathrm{P}}$ film was ~2000 with a loss tangent of ~0.05, measured from 100 Hz to 100 kHz, as shown in Figure 3.3(b). Fe$_{\mathrm{P}}$ and Sc$_{\mathrm{P}}$ films showed relatively low dielectric permittivities of ~900 and ~700 with loss tangents of ~0.03 over the measured frequency range. As expected, the Cr$_{\mathrm{P}}$ film displayed a low dielectric permittivity of ~180 with 0.02 loss tangent, presumably arising from the poor structural properties discussed earlier.

P-E loops of all the B-site disordered films measured at room temperature and 10 kHz are presented in Figure 3.3(c). The loops for Al$_{\mathrm{P}}$, Fe$_{\mathrm{P}}$, and Sc$_{\mathrm{P}}$ films share a very similar shape, with Al$_{\mathrm{P}}$ displaying a slightly lower P_{max}, ascribed to the lower propensity for the Al^{3+} to deviate from the center of the octahedron, which would in turn decrease the switchable polarization response [46]. Consistent with the structural and dielectric properties, Cr$_{\mathrm{P}}$ film behaved more like a linear dielectric than a ferroelectric material with a low P_{max} of ≤ 8 μC cm^{-2}.

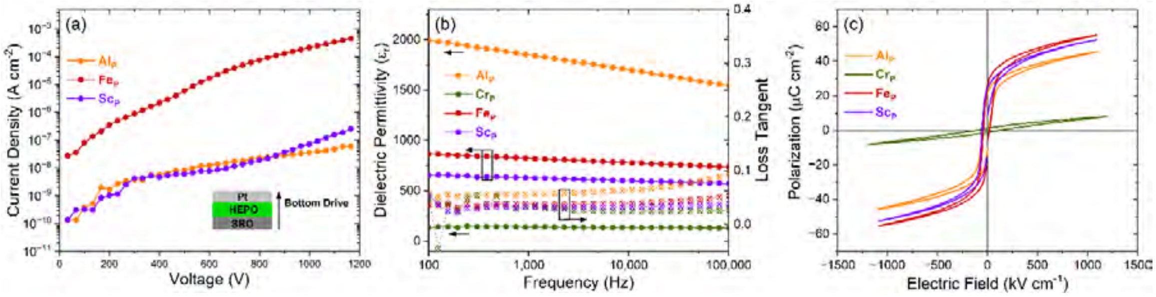

Figure 3.3. (a) Current density of the B-site disordered films in response to DC electric fields up to 1200 kV cm^{-1}. The inset shows that the voltage was driven from the bottom electrode. (b) Dielectric permittivity and loss tangent of the films measured at room temperature over the frequency range from 100 Hz to 100 kHz. (c) P-E loops of the B-site disordered HEPO films measured at room temperature, 10 kHz, with an applied electric field of 1100 kV cm^{-1}.

3.3.2.2 Temperature-dependent Dielectric Properties

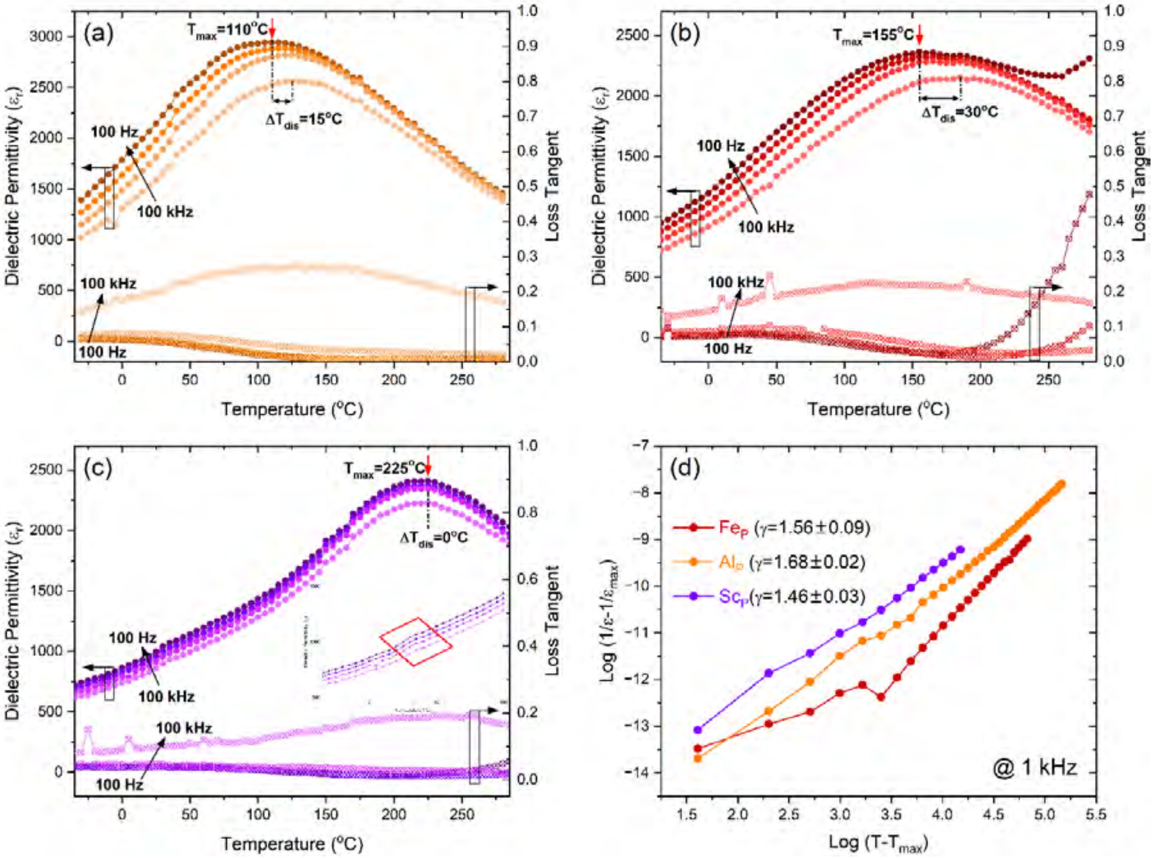

Figure 3.4. Temperature-dependent dielectric permittivity and loss tangent of (a) Al_P film, (b) Fe_P film, and (c) Sc_P film. (d) Modified Curie-Weiss law of Al_P, Fe_P, and Sc_P films showing the level of relaxor character (γ).

The temperature-dependent dielectric permittivity and loss tangent for Al_P, Fe_P, and Sc_P films are shown in Figure 3.4(a), (b), and (c), respectively. $\Delta T_{dis} (= T_{max,100Hz} - T_{max,100KHz})$ was utilized to quantify the degree of dispersion of the dielectric maxima (T_{max}). The Al_P film exhibited strong dispersion of the dielectric permittivity below the T_{max} of 110℃, with ΔT_{dis} of 15°C. The dispersion collapses above T_{max}, as is expected in a relaxor ferroelectric. In the Fe_P film (Figure 3.4(b)), a higher T_{max} of 155°C was achieved with a larger ΔT_{dis} of 30°C. The abrupt increase in the 100 Hz dielectric permittivity and loss tangent above 200℃, is almost certainly associated with space charge polarizability. Such non-negligible space charge at elevated temperature contributes to the measured dielectric permittivity, resulting in a large ΔT_{dis} of 30°C [47]. However, interestingly, dielectric dispersion was suppressed for the Sc_P film (ΔT_{dis} of 0°C). The measured T_{max} was 255°C, the highest among the B-site disordered HEPO films. This could be linked, at least in part, to the larger rhombohedral distortion in Sc_P, compared to Al_P and Fe_P films. Furthermore, the small hump in the permittivity vs. temperature curve near 35°C looks like a ferroelectric-ferroelectric distortion (possibly a rhombohedral to tetragonal phase transformation), which could provide an additional entropy change for the ECE. Comparing the data for the sample shown, the T_{max} of the HEPO films increased as the average B-site cation size increased.

In Figure 3.4(d), the relative degree of relaxation is examined by means of a modified Curie-Weiss law, as shown by:

$$\frac{1}{\varepsilon_r} - \frac{1}{\varepsilon_{max}} = \frac{(T - T_{max})^{\gamma}}{C}$$

where ε_r is the dielectric permittivity, ε_{max} is the maximum dielectric permittivity, C is the Curie-Weiss constant, and γ is the degree of relaxation. In an ideal relaxor ferroelectric, the value of γ is likely to be 2; in an ideal normal ferroelectric, γ is close to 1. The ΔT_{dis} of 0°C is not always correlated with $\gamma=1.00$, as is shown in the case of $K(Ta_{0.55}Nb_{0.45})O_3$ that has $\gamma=1.17$, despite a sharp transition [48,49]. Furthermore, the intermediate $\gamma=1.56\pm0.09$ for Fe_P film is very close to that of $0.88Pb(Zn_{1/3}Nb_{2/3})O_3$-$0.12PbTiO_3$ ($\gamma=1.58$) which is between a relaxor and a normal ferroelectric, while $\gamma=1.68\pm0.02$ of Al_P film is very similar to that of $Pb(Mg_{1/3}Nb_{2/3})O_3$ (PMN) ($\gamma=1.70$). That is, there is a continuum between relaxor and normal ferroelectric character [50]. Thus, Al$_P$ film behaves more like a relaxor-ferroelectric with γ of 1.68±0.02. Sc$_P$ film behaves more like a normal ferroelectric with γ of 1.46±0.03. In combination with the dielectric permittivity data above, the Sc ion may promote a relatively longer length scale for polar order compared to the other compositions.

3.3.2.3 Temperature-dependent Ferroelectric Properties and Electrocaloric Effects

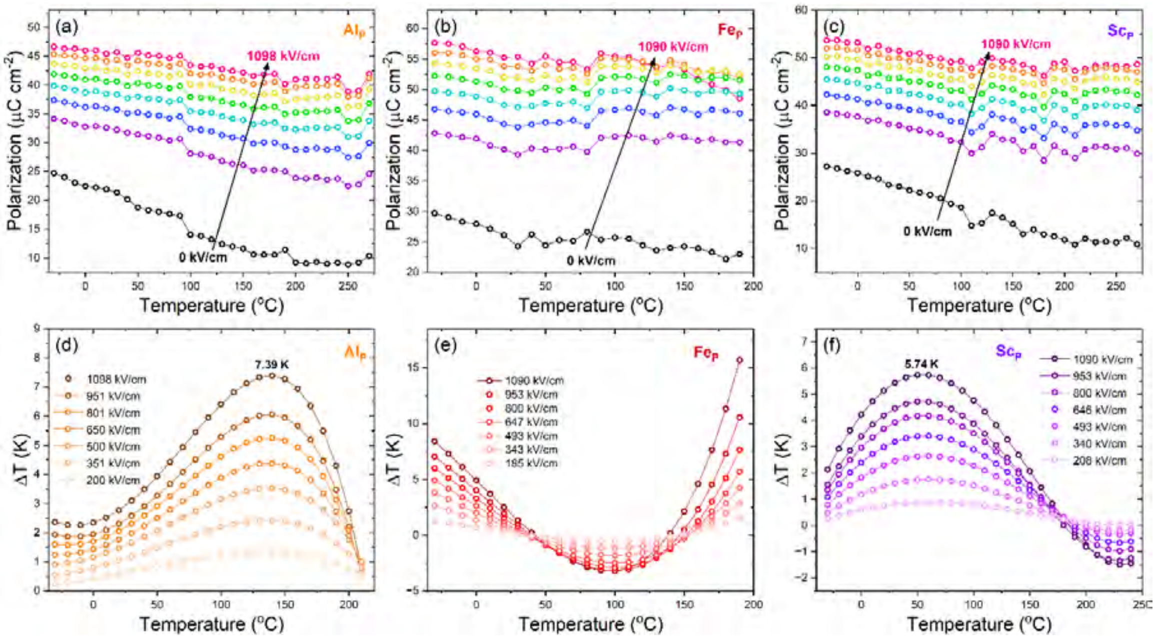

Figure 3.5. Polarization as a function of temperature extracted from temperature dependent P-E loops for (a) Al$_P$ films, (b) Fe$_P$ films, and (c) Sc$_P$ films. Indirectly measured electrocaloric temperature change for (d) Al$_P$ films, (e) Fe$_P$ films, and (f) Sc$_P$ films. Data for the Fe$_P$ film are strongly affected by artifacts associated with high field leakage.

The P-E loops of Al$_P$, Fe$_P$, and Sc$_P$ films were measured at 10 kHz from -35℃ to 275℃. The applied voltage of 32 V (~1100 kV cm^{-1}) was less than 40% of the breakdown voltage (~96 V, ~3400 kV cm^{-1}). This was chosen to prevent unintentional sample failure during measurement. The Sc$_P$ and Al$_P$ film maintain slim P-E loops (shown in Figure 3. S16(a) and (c)) over the measured temperature range. However, the P-E loops for the Fe$_P$

film become more “banana-like” at high temperatures, due to increasing leakage contributions [51]. These changes were reflected in Figure 3.5(a) – (c).

Polarization-Temperature curves (P-T curve) were extracted from the upper branch of the P-E loops. It is clear that the polarization changes in Al_P and Sc_P films from the P-T curve behave similarly. However, bloated “banana-like” P-E loops in the Fe_P film (See Figure 3.S16(b)) lead to overestimation of the polarization and misinterpretation of the electrocaloric effects of the material [7,51,52]. From -30°C to 180°C, P_{rem} for the Al_P film dropped from 24.7 $\mu C\ cm^{-2}$ to 10.5 $\mu C\ cm^{-2}$, while P_{rem} for Sc_P film decreased from 27.2 $\mu C\ cm^{-2}$ to 13.0 $\mu C\ cm^{-2}$. Interestingly, over this temperature range, P_{rem} of the Al_P film was roughly 85% that of the Sc_P film. The difference in P_{rem} could be attributed to non-ferroelectrically active Al ion which accounts for 20 % of the B-site cations.

To estimate the ECE of the films, an indirect method (based on Maxwell’s relations), was employed. This can be expressed as:

$$\Delta T = -\int_{E_1}^{E_2} \frac{T}{\rho C_p} \left(\frac{dP}{dT}\right)_E dE$$

$$\Delta S = \frac{1}{\rho} \int_{E_1}^{E_2} \left(\frac{dP}{dT}\right)_E dE$$

where T is the temperature, ρ is the density of the material, C_p is the specific heat capacity, P is the polarization, and E_1 and E_2 are the initial and final electric fields, respectively. Here, the theoretical density was calculated for each composition; it was assumed that the heat capacity of the films would be comparable to the well-known relaxor ferroelectric, $PbMg_{1/3}Nb_{2/3}O_3$-$PbTiO_3$ (PMN-PT) [53]. In Figure 3.5(d) – (f), the electrocaloric temperature changes are shown. The Al_P film had a temperature change of

7.39 K at 135℃ for an applied electric field of 1100 kV cm^{-1}. The magnitude of the temperature change was consistent with previous studies, which showed a slightly higher temperature change due to a larger applied field [34]. The other noticeable change was that the maximum electrocaloric temperature change ($T_{max,ECE}$) occurred at lower temperature, compared to the previous study of Al_P on Si that has $T_{max,ECE}$ of 180℃. Typically, compressive strain shift $T_{max,ECE}$ towards a higher temperature, but the opposite happened here [54]. It is speculated that differences in defect chemistry originating from different growth conditions triggered the change in T_{max}, and ultimately in electrocaloric responses [55].

The appearance of both negative and positive calculated electrocaloric temperature changes for the Fe_P film over the measured temperature range is an artifact associated with high field leakage [56,57].

In spite of the relatively smaller electrocaloric temperature change in Sc_P film (5.74 K), it had a $T_{max,ECE}$ of 50°C, close to room temperature [58,59]. The Sc_P film experienced what appears to be a ferroelectric-ferroelectric phase transition measured at low field around 35℃ as shown in Figure 3.4(c); this transition temperature could shift with the magnitude of the applied field, and so may be the origin of the electrocaloric temperature peak of 5.74 K near 50℃. The negative temperature change of Sc_P film above 175℃ is attributed to leakage, as evidenced by a leakage-induced increase in the polarization at ≥ 170℃ (see Figure 3.S16(c)).

3.3.3 Polarization Stability of the B-site Disordered HEPO Films

3.3.3.1 Polarization Decay by Positive-Up-Negative-Down (PUND) Measurement

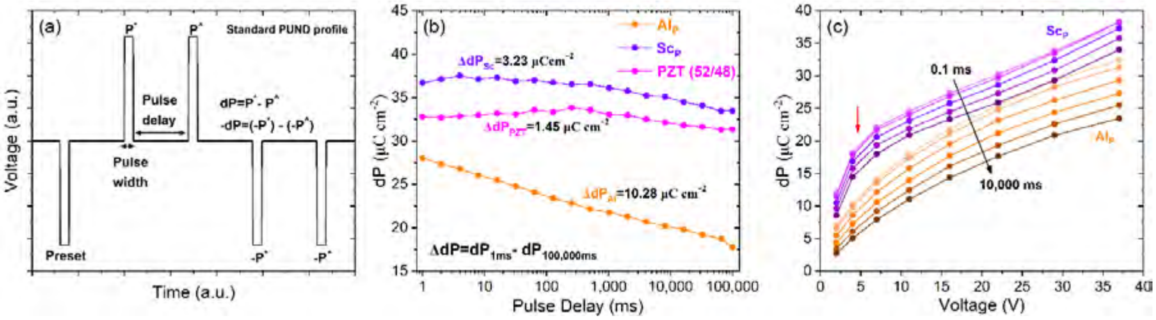

Figure 3.6. (a) Schematic of the PUND voltage profile. (b) Remanent polarization of Al_P (Orange), PZT (52/48) (Pink) and Sc_P (Purple) films measured by the PUND. (c) Remanent polarization of Al_P and Sc_P films as a function of voltage from 1 V to 37 V for varying pulse delays. The red arrow indicates an abrupt change in dP of a Sc_P film which could be associated with a field-induced phase transition.

To study the polarization stability of the HEPO films, a voltage pulse was applied as a function of delay time via PUND measurement. A schematic of the PUND waveform can be seen in Figure 3.6(a). Briefly, dipoles switched by the first voltage pulse (P^*) are likely to relax over time (pulse delay). The second measurement ($P^\wedge$) captures non-remanent polarization and leakage. This remanent polarization is then $dP = P^* - P^\wedge$. Here, the pulse delay was varied to quantify the dipole relaxation as a function of time. As shown in Figure 3.6(b), dP was measured from pulse delays of 1 ms to 100,000 ms with an applied voltage of 32 V for Al_P, Sc_P, and 2% Nb-doped $PbZr_{0.52}Ti_{0.48}O_3$ (PZT(52/48)) films. The Fe_P film was not included for the polarization stability study due to its leaky response. The magnitude of the change of dP over delay time was calculated via $\Delta dP = dP_{1\,ms} - dP_{100{,}000\,ms}$. The normal ferroelectric PZT (52/48) film exhibits a small drop in remanent polarization (~1.5 μCcm^{-2}). Likewise, other normal ferroelectrics such as doped-HfO_2, $Al_{0.7}Sc_{0.3}N$, and $BaTiO_3$ films have negligible decay of dP over this time scale [60–62]. In comparison, the polarization drop (ΔdP) for the $\mathrm{Sc_P}$ film was 3.2 μC $\mathrm{cm^{-2}}$; in the $\mathrm{Al_P}$ film it was 10.3 μC $\mathrm{cm^{-2}}$. It is noted that this significant difference cannot be due to a difference in the structural order, as the $\mathrm{Sc_P}$ and $\mathrm{Al_P}$ films have very similar FWHM in the X-ray data. Rather, this significant difference suggests that the Al ions break up the long-range polar order, changing the local structural distortions, and causing rapid decay of the dP in the $\mathrm{Al_P}$ film (see Figure 3.S18). Converting this into the frequency domain, 28.0 μC $\mathrm{cm^{-2}}$ of ΔdP can be achieved at 1 kHz, while approximately 21.8 μC $\mathrm{cm^{-2}}$ can be obtained for a 1 Hz cycle, showing the time dependent polarization relaxation of the $\mathrm{Al_P}$ film. In contrast, Sc facilitates more long-range polar order, such that a written polarization state is better preserved over time. The difference in polarization relaxation between a normal ferroelectric and a HEPO (or high entropy ferroelectric) is schematically illustrated in Figure 3.S6. In short, the compositional complexity of the HEPO film frustrates long-range polar ordering, and leads to faster relaxation of the induced polarization. The tendency of the ΔdP in the $\mathrm{Al_P}$ film was similar to that reported in $\mathrm{PbZrO_3}$, where the switching behavior was perturbed by defect dipoles showing the metastability of remanent dipoles [63].

To further investigate the polarization stability in the $\mathrm{Al_P}$ and $\mathrm{Sc_P}$ films, dP was investigated as a function of applied voltage with varying delay times. A sharp increase of dP in $\mathrm{Sc_P}$ film was observed around 5 V, as highlighted by red arrow in the figure. It is speculated that this is indicative of a field-induced rhombohedral to tetragonal-like phase transition in the $\mathrm{Sc_P}$ film given the fact that $\mathrm{Sc_P}$ possess rhombohedral structure from powder XRD as shown in Figure 3.1(d) [64]. This result supports the observation of ECE peak of $\mathrm{Sc_P}$ film at around 50℃. Furthermore, development of ferroelectricity in HEO-like formulation is sensitive to specific elements, enabling engineerable ferroelectricity in HEO-like materials.

3.3.3.2 Estimation of Activation Energy for Depolarization of Dipoles

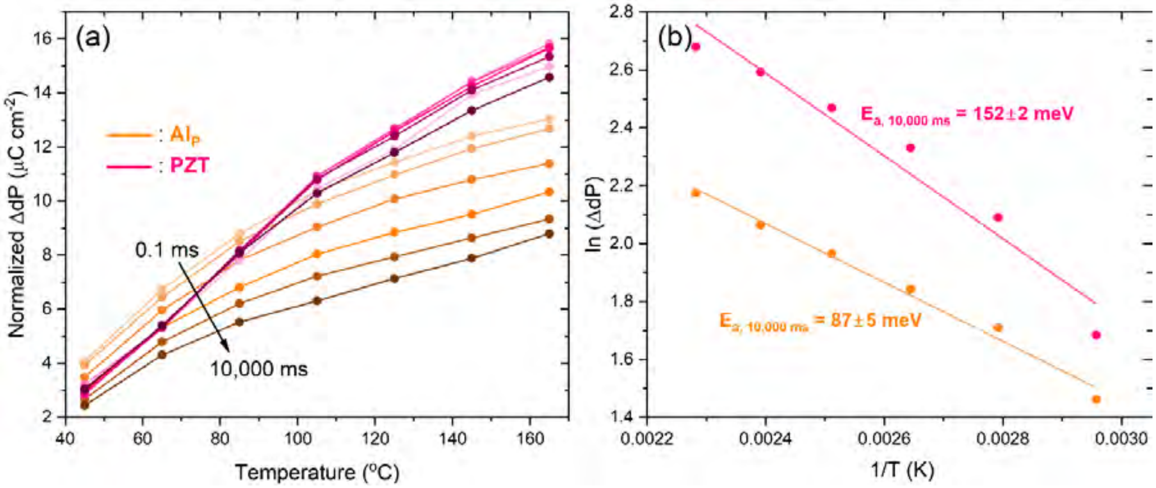

Figure 3.7. (a) Normalized remanent polarization of AlP and PZT films as a function of temperature and (b) activation energy for the depolarization of dipoles estimated with the Arrhenius equation using dP with 10,000 ms data.

The dP for the AlP film was measured up to 165℃, and compared to that of the PZT film. The dP was normalized against $\mathrm{dP_{room\ temperature}}$. The temperature-dependent dP was fitted using an Arrhenius-like equation $\ln(\Delta\mathrm{dP}) = \exp\left(-\mathrm{E_a}/\mathrm{RT}\right) + \ln(\mathrm{A})$, where $\mathrm{E_a}$ is activation energy for the depolarization with 10,000 ms delay time, R is gas constant, T is temperature, and $\ln(\mathrm{A})$ is the y-intercept, as shown in Figure 3.7(b). The energy required for the depolarization of dipoles in AlP film is calculated to be ≈87±5 meV while the energy for the PZT film is extracted to be ≈ 152±2 meV. A 70 nm PZT (25/75) normal ferroelectric capacitor used for ferroelectric memory has been reported to exhibit an activation energy of 280 meV for the depolarization [65]. The comparatively high activation energy for the PZT film is consistent with careful control of the defect chemistry and the quality of the ferroelectric/electrode interfaces essential to ensure retention in the memory. Obviously, the AlP film has a much smaller activation energy for the depolarization. It is speculated that the large local strain and electric fields created by disorder on the B-site of AlP film provokes instability of the dipoles, lowering the activation energy for the depolarization.

3.3.3.3 Enhanced ECE by Customized PUND Measurement

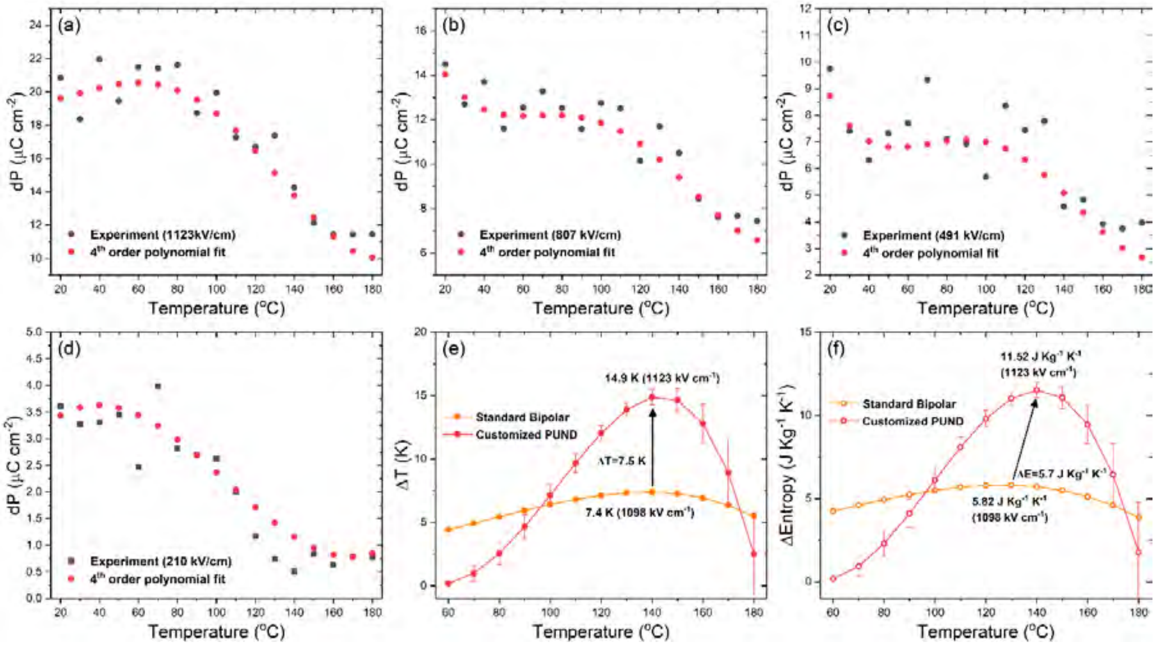

Figure 3.8. Remanent polarization (dP) as a function of temperature measured by customized PUND and polynomial fit for applied electric field of (a) 1123 kV cm^{-1}, (b) 807 kV cm^{-1}, (c) 491 kV cm^{-1}, (d) 210 kV cm^{-1}. (e) Enhanced electrocaloric temperature change of AlP film and (f) entropy change by customized PUND.

The polarization decay in AlP film over time suggests a possible time-dependent enhancement of the ECE. To assess this, PUND data were taken to extract time-dependent P vs T curves. A pulse delay of 2000 ms was chosen. Detailed information of the customized-PUND can be found in the supplementary material (Figure 3.S19(a) and (b)).

The remanent polarization measured via the customized-PUND is shown in Figure 3.8(a) – (d) for applied electric fields of 1123 kV cm^{-1}, 807 kV cm^{-1}, 491 kV cm^{-1}, 210 kV cm^{-1}, respectively; the data were fit with a 4th order polynomial. It was found that a significant polarization drop occurred between 100℃ and 160℃, as shown in Figure 3.S20. This range of temperature is consistent with the T_{max} of the Al_P film (110℃) as well as the peak of ECE measured by standard bipolar P-E loops. However, the time delay boosts relaxation of the polarization. A comparison between standard bipolar P-E loops-induced ECE and the customized PUND-induced ECE is shown in Figure 3.8(e) and (f). The electrocaloric temperature and entropy change extracted from the customized-PUND were 14.9 K and 11.52 J Kg^{-1} K^{-1} respectively, an enhancement of 7.5 K and 7.20 J Kg^{-1} K^{-1}. That is, a delay time of 2000 ms was long enough to randomize dipoles aligned by a voltage pulse so that the polar entropy was markedly enhanced. This ultimately resulted in a larger change in the polarization response, which could double the ECE of the Al_P films. These results provide insights into the development of ferroelectricity in HEO-like materials, including the influence of polarization stability on the functional properties such as ECE.

3.4. Conclusions

The structural and electrical properties of several different HEPO films were investigated, with an emphasis on the electrocaloric effect and polarization stability. Structural analysis of the HEPO powders revealed the perovskite tolerance factor controls the ferroelectric distortion observed. HEPO films with disorder on the B-site can be fabricated by pulsed laser deposition with good structural quality on SRO/STO, excepting the Cr$_{\mathrm{P}}$ composition. Fe$_{\mathrm{P}}$ films show high leakage, presumably due to charge hopping. Al$_{\mathrm{P}}$ and Sc$_{\mathrm{P}}$ films displayed relaxor-like and ferroelectric-like behaviors based on dielectric properties, respectively. The electrocaloric temperature change in Al$_{\mathrm{P}}$ and Sc$_{\mathrm{P}}$ films extracted by Maxwell-relations were 7.39 K at 135℃ and 5.74 K at 50℃, respectively. PUND measurement was employed to study the polarization stability of the films. It showed rapid polarization decay for Al$_{\mathrm{P}}$ films due to the relaxor-like properties associated with the Al ion. A field-induced phase transition for Sc$_{\mathrm{P}}$ film was observed, which could be a useful source of ECE. The activation energy for the depolarization of the Al$_{\mathrm{P}}$ film was $\approx$ 87 meV. An enhanced ECE temperature change of 14.9 K was observed for the Al$_{\mathrm{P}}$ film via a customized-PUND that allowed 2000 ms of rest between measurement pulses to promote dipole randomization.

3.5. References

[1] S.G. Lu, Q. Zhang, Electrocaloric Materials for Solid-State Refrigeration, Adv. Mater., 21 (2009), pp. 1983–1987

[2] A. Mischenko, Q. Zhang, J. Scott, R.Whatmore, N. Mathur, , Giant electrocaloric effect in thin-film $PbZr_{0.95}Ti_{0.05}O_3$, Science, 311 (2006), pp. 1270-1271

[3] O. V. Pakhomov, S.F. Karmanenko, A.A. Semenov, A.S. Starkov, A. V. Es'kov, Thermodynamic estimation of cooling efficiency using an electrocaloric solid-state line, Tech. Phys., 55 (2010), pp. 1155–1160

[4] J. Shi, D. Han, Z. Li, L. Yang, S.-G. Lu, Z. Zhong, J. Chen, Q.M. Zhang, X. Qian, Electrocaloric Cooling Materials and Devices for Zero-Global-Warming-Potential, High-Efficiency Refrigeration, Joule, 3 (2019), pp. 1200–1225

[5] R. Ma, Z. Zhang, K. Tong, D. Huber, R. Kornbluh, Y.S. Ju, Q. Pei, Highly efficient electrocaloric cooling with electrostatic actuation, Science, 357 (2017), pp. 1130–1134

[6] H. Gu, X. Qian, X. Li, B. Craven, W. Zhu, A. Cheng, S.C. Yao, Q.M. Zhang, A chip scale electrocaloric effect based cooling device, Appl. Phys. Lett., 102 (2013), Article 122904

[7] Y. Sun, S.E. Shirsath, S. Zhang, D. Wang, A reflection on recent efforts in optimization of cooling capacity of electrocaloric thin films, APL Mater., 11 (2023), Article 090602

[8] A. Torelló, P. Lheritier, T. Usui, Y. Nouchokgwe, M. Gérard, O. Bouton, S. Hirose, E. Defay, Giant temperature span in electrocaloric regenerator, Science, 370 (2020), pp. 125-129

[9] J. Li, A. Torelló, Y. Nouchokgwe, T. Granzow, V. Kovacova, S. Hirose, E. Defay, Electrocaloric effect in $BaTiO_3$ multilayer capacitors with first-order phase transitions, J. Phys. Energy., 5 (2023), Article 024017

[10] S.G. Lu, B. Rožič, Q.M. Zhang, Z. Kutnjak, X. Li, E. Furman, L.J. Gorny, M. Lin, B. Malič, M. Kosec, R. Blinc, R. Pirc, Organic and inorganic relaxor ferroelectrics with giant electrocaloric effect, Appl. Phys. Lett., 97 (2010), p. 162904

[11] B. Peng, Q. Zhang, B. Gang, G.J.T. Leighton, C. Shaw, S.J. Milne, B. Zou, W. Sun, H. Huang, Z. Wang, Phase-transition induced giant negative electrocaloric effect in a lead-free relaxor ferroelectric thin film, Energy Environ. Sci., 12 (2019), pp. 1708–1717

[12] A.S. Mischenko, Q. Zhang, R.W. Whatmore, J.F. Scott, N.D. Mathur, Giant electrocaloric effect in the thin film relaxor ferroelectric 0.9Pb $Mg_{1/3}Nb_{2/3}O_3$-0.1$PbTiO_3$ near room temperature, Appl. Phys. Lett., 89 (2006), Article 242912

[13] R. Pirc, Z. Kutnjak, R. Blinc, Q.M. Zhang, Electrocaloric effect in relaxor ferroelectrics, J. Appl. Phys., 110 (2011), Article 74113

[14] R.A. Cowley, S.N. Gvasaliya, S.G. Lushnikov, B. Roessli, G.M. Rotaru, Relaxing with relaxors: A review of relaxor ferroelectrics, Adv. Phys., 60 (2011), pp. 229–327

[15] L.E. Cross, E. Pugh, Relaxor ferroelectrics, Ferroelectrics, 76 (1987), pp. 241–267

[16] C.A. Randall, A.S. Bhalla, T.R. Shrout, L.E. Cross, Classification and consequences of complex lead perovskite ferroelectrics with regard to B-site cation order, J. Mater. Res., 5 (1990), pp. 829–834

[17] B. Cantor, I.T.H. Chang, P. Knight, A.J.B. Vincent, Microstructural development in equiatomic multicomponent alloys, Mater. Sci. Eng. A., 375–377 (2004), pp. 213–218

[18] J.W. Yeh, S.K. Chen, S.J. Lin, J.Y. Gan, T.S. Chin, T.T. Shun, C.H. Tsau, S.Y. Chang, Nanostructured high-entropy alloys with multiple principal elements: Novel alloy design concepts and outcomes, Adv. Eng. Mater., 6 (2004), pp. 299–303

[19] C.M. Rost, E. Sachet, T. Borman, A. Moballegh, E.C. Dickey, D. Hou, J.L. Jones, S. Curtarolo, J.-P. Maria, Entropy-stabilized oxides, Nat. Commun., 6 (2015), pp. 1–8

[20] M. Brahlek, M. Gazda, V. Keppens, A.R. Mazza, S.J. McCormack, A. Mielewczyk-Gryń, B. Musico, K. Page, C.M. Rost, S.B. Sinnott, C. Toher, T.Z. Ward, A.

Yamamoto, What is in a name: Defining “high entropy” oxides, APL. Mater., 10 (2022), p. 110902

[21] S.S. Aamlid, M. Oudah, J. Rottler, A.M. Hallas, Understanding the Role of Entropy in High Entropy Oxides, J. Am. Chem. Soc., 145 (2023), pp. 5991–6006

[22] B. Yang, Y. Zhang, H. Pan, W. Si, Q. Zhang, Z. Shen, Y. Yu, S. Lan, F. Meng, Y. Liu, H. Huang, J. He, L. Gu, S. Zhang, L.Q. Chen, J. Zhu, C.W. Nan, Y.H. Lin, High-entropy enhanced capacitive energy storage, Nat. Mater., 21 (2022), pp. 1074–1080

[23] F. Li, L. Zhou, J.X. Liu, Y. Liang, G.J. Zhang, High-entropy pyrochlores with low thermal conductivity for thermal barrier coating materials, J. Adv. Ceram., 8 (2019), pp. 576–582

[24] T.X. Nguyen, Y.-C. Liao, C.-C. Lin, Y.-H. Su, J.-M. Ting, Advanced High Entropy Perovskite Oxide Electrocatalyst for Oxygen Evolution Reaction, Adv. Funct. Mater., 31 (2021), Article 2101632

[25] D. Wang, S. Jiang, C. Duan, J. Mao, Y. Dong, K. Dong, Z. Wang, S. Luo, Y. Liu, X. Qi, Spinel-structured high entropy oxide $(FeCoNiCrMn)_3O_4$ as anode towards superior lithium storage performance, J. Alloys Compd., 844 (2020), Article 156158

[26] J. Gild, M. Samiee, J.L. Braun, T. Harrington, H. Vega, P.E. Hopkins, K. Vecchio, J. Luo, High-entropy fluorite oxides, J. Eur. Ceram. Soc., 38 (2018), pp. 3578–3584

[27] S. Jiang, T. Hu, J. Gild, N. Zhou, J. Nie, M. Qin, T. Harrington, K. Vecchio, J. Luo, J. Luo, A new class of high-entropy perovskite oxides, Scr. Mater., 142 (2018), pp. 116–120

[28] W. L. Hsu, C. W. Tsai, A. C. Yeh, J. W. Yeh, Clarifying the Four Core Effects of High-Entropy Materials, Nat. Rev. Chem., 8 (2024), pp. 471-485

[29] R. Blinc, J. Dolinšek, A. Gregorovic, B. Zalar, C. Filipic, Z. Kutnjak, A. Levstik, R. Pirc, Local Polarization Distribution and Edwards-Anderson Order Parameter of Relaxor Ferroelectrics, Phys. Rev. Lett., 83 (1999), pp. 424–427.

[30] A. Bussmann-Holder, A. R. Bishop, Intrinsic Local Modes and Heterogeneity in Relaxor Ferroelectrics, J. Phys.: Condens. Mater., 16 (2004), pp. L313-L320

[31] W. Liu, F. Li, G. Chen, G. Li, H. Shi, L. Li, Y. Guo, J. Zhai, C. Wang, Comparative Study of Phase Structure, Dielectric Properties and Electrocaloric Effect in Novel High-Entropy Ceramics, J. Mater. Sci., 56 (2021), pp. 18417–18429

[32] Y. Pu, Q. Zhang, R. Li, M. Chen, X. Du, S. Zhou, Dielectric Properties and Electrocaloric Effect of High-Entropy $(Na_{0.2}Bi_{0.2}Ba_{0.2}Sr_{0.2}Ca_{0.2})TiO_3$ Ceramic, Appl. Phys. Lett., 115 (2019), pp. 0-5

[33] X. Qian, D. Han, L. Zheng, J. Chen, M. Tyagi, Q. Li, F. Du, S. Zheng, X. Huang, S. Zhang, J. Shi, H. Huang, X. Shi, J. Chen, H. Qin, J. Bernholc, X. Chen, L.-Q. Chen, L. Hong, Q.M. Zhang, High-Entropy Polymer Produces a Giant Electrocaloric Effect at Low Fields, Nature, 600 (2021), pp. 664–669

[34] Y. Son, W. Zhu, S.E. Trolier-Mckinstry, Electrocaloric Effect of Perovskite High Entropy Oxide Films, Adv. Electron. Mater., 8 (2022), Article 220352

[35] W. Zhu, B. Akkopru-Akgun, J. I. Yang, C. Fragkiadakis, K. Wang, S. W. Ko, P. Mardilovich, S. Trolier-McKinstry, Influence of Graded Doping on the Long-term Reliability of Nb-doped Lead Zirconate Titanate Films, Acta Mater., 219 (2021), Article 117251

[36] S.L. Swartz, T.R. Shrout, Fabrication of Perovskite Lead Magnesium Niobate, Mater. Res. Bull., 17 (1982), pp. 1245–1250

[37] H. D. Megaw, Crystal Structure of Double Oxides of the Perovskite Type, Proc. Phys. Soc., 58 (1946), p. 133-152

[38] R. D. Shannon, Revised Effective Ionic Radii and Systematic Studies of Interatomic Distances in Halides and Chalcogenides, Acta. Cryst. Sect. A., 32 (1976), pp. 751-767

[39] M. Fracchia, M. Coduri, P. Ghigna, U. Anselmi-Tamburini, Phase Stability of High Entropy Oxides: A critical review, J. Eur. Ceram. Soc., 44 (2024), pp. 585–594

[40] I.M. Reaney, E.L. Colla, N. Setter, Dielectric and Structural Characteristics of Ba- and Sr-based Complex Perovskites as a Function of Tolerance Factor, Jpn. J. Appl. Phys., 33 (1994), pp. 3984-3990

[41] Z. Liu, S. Xu, T. Li, B. Xie, K. Guo, J. Lu, Microstructure and Ferroelectric Properties of High-Entropy Perovskite Oxides with A-site Disorder, Ceram. Int., 47 (2021), pp. 33039–33046

[42] H. V. Alexandru, C. Berbecaru, A. Ioachim, L. Nedelcu, A. Dutu, BST Solid Solutions, Temperature Evolution of the Ferroelectric Transitions, Appl. Surf. Sci., 253 (2006), pp. 354–357

[43] M. Ghita, M. Fornari, D.J. Singh, S. V Halilov, Interplay Between A-site and B-site Driven Instabilities in Perovskites, Phys. Rev. B., 72 (2005), Article 054114

[44] M. Zheng, W. Wang, Tunable Ferromagnetic Transition Temperature and Vertical Hysteretic Shift in $SrRuO_3$ Films Integrated on Si(001), ACS Appl. Mater. Interfaces., 8 (2016), pp. 14012–14018

[45] Z. Wang, B.H. Goodge, D.J. Baek, M.J. Zachman, X. Huang, X. Bai, C.M. Brooks, H. Paik, A.B. Mei, J.D. Brock, J.P. Maria, L.F. Kourkoutis, D.G. Schlom, Epitaxial $SrTiO_3$ Film on Silicon with Narrow Rocking Curve despite Huge Defect Density, Phys. Rev. Mater., 3 (2019), Article 073403

[46] R.E. Cohen, Origin of Ferroelectricity in Perovskite Oxides, Nature, 358 (1992), pp. 136–138

[47] R. K. Dwivedi, D. Kumar, O. Parkash, Valence Compensated Perovskite Oxide System $Ca_{1-x}La_xTi1\text{-}xCr_xO_3$. Part ll: Electrical Transport Behavior, J. Mater. Sci., 36 (2001), pp. 3649-3655

[48] S. Nomura, K. Uchino, Critical Exponents of the Dielectric Constants in Diffused-Phase-Transition Crystals, Ferroelectrics, 44 (1982), pp. 55-61

[49] K. Uchino, Electrostrictive and Piezoelectric Effects in Relaxor Ferroelectrics: Historical Background, IEEE Trans. Ultrason. Eng. 69 (2022), pp. 3013-3036

[50] M. J. Cabral, S. Zhang, E. C. Dickey, J. M. LeBeau, Gradient Chemical Order in the Relaxor $Pb(Mg_{1/3}Nb_{2/3})O_3$, 112 (2018), Article 082901

[51] J.F. Scott, Ferroelectrics Go Bananas, J. Phys. Condens. Matter., 20 (2007), Article 021001

[52] M. Wu, D. Song, G. Vats, S. Ning, M. Guo, D. Zhang, D. Xue, S.J. Pennycook, X. Lou, Defect-Controlled Electrocaloric Effect in $PbZrO_3$ Thin Films, J. Mater. Chem. C. Mater., 6 (2018), pp. 10332–10340

[53] H. Uršič, M. Vrabelj, L. Fulanovič, A. Bradeško, S. Drnovšek, B. Malič, Specific Heat Capacity and Thermal Conductivity of the Electrocaloric (1-

x)Pb($Mg_{1/3}Nb_{2/3}$)O_3–xPbTiO_3 Ceramics Between Room Temperature and 300℃, J. Microelectron. Electron. Components Mater., 45 (2015), pp. 260-265

[54] D.L. Shan, C.H. Lei, Y.C. Cai, K. Pan, Y.Y. Liu, Mechanical Control of Electrocaloric Response in Epitaxial Ferroelectric Thin Films, Int. J. Solids. Struct., 216 (2021), pp. 59–67

[55] S. Saremi, J. Kim, A. Ghosh, D. Meyers, L.W. Martin, Defect-Induced (Dis)Order in Relaxor Ferroelectric Thin Films, Phys. Rev. Lett., 123 (2019), Article 207602

[56] B. Peng, Q. Zhang, Y. Lyu, L. Liu, X. Lou, C. Shaw, H. Huang, Z. Wang, Thermal Strain induced Large Electrocaloric Effect of Relaxor Thin Film on $LaNiO_3$/Pt Composite Electrode with the Coexistence of Nanoscale Antiferroelectric and Ferroelectric Phases in a Broad Temperature Range, Nano Energy, 47 (2018), pp. 285–293

[57] B. Peng, T. Wang, L. Liu, X. Chen, J. Li, Q. Zhang, R. Yang, W. Sun, Z.L. Wang, P-GaN-Substrate Sprouted Giant Pure Negative Electrocaloric Effect in Mn-doped $Pb(Zr_{0.3}Ti_{0.7})O_3$ Thin Film with a Super-Broad Operational Temperature Range, Nano Energy, 86 (2021), Article 106059

[58] J. Hagberg, A. Uusimäki, H. Jantunen, Electrocaloric Characteristics in Reactive Sintered $0.87Pb(Mg_{1/3}Nb_{2/3})O_3$–$0.13PbTiO_3$, Appl. Phys. Lett., 92 (2008), Article 132909

[59] B. Peng, H. Fan, Q. Zhang, A Giant Electrocaloric Effect in Nanoscale Antiferroelectric and Ferroelectric Phases Coexisting in a Relaxor $Pb_{0.8}Ba_{0.2}ZrO_3$ Thin Film at Room Temperature, Adv. Funct. Mater., 23 (2013), pp. 2987–2992

[60] J.W. Adkins, I. Fina, F. Sánchez, S.R. Bakaul, J.T. Abiade, Thermal Evolution of Ferroelectric Behavior in Epitaxial $Hf_{0.5}Zr_{0.5}O_2$, Appl. Phys. Lett., 117 (2020), Article 142902

[61] R. Nie, S. Shao, Z. Luo, X. Kang, T. Wu, Characterization of Ferroelectric $Al_{0.7}Sc_{0.3}N$ Thin Film on Pt and Mo Electrodes, Micromachines, 13 (2022), Article 1629

[62] Y. Jiang, E. Parsonnet, A. Qualls, W. Zhao, S. Susarla, D. Pesquera, A. Dasgupta, M. Acharya, H. Zhang, T. Gosavi, C.C. Lin, D.E. Nikonov, H. Li, I.A. Young, R. Ramesh, L.W. Martin, Enabling Ultra-Low-Voltage Switching in $BaTiO_3$, Nat. Mater., 21 (2022), pp. 779–785

[63] H. Pan, Z. Tian, M. Acharya, X. Huang, P. Kavle, H. Zhang, L. Wu, D. Chen, J. Carroll, R. Scales, C.J.G. Meyers, K. Coleman, B. Hanrahan, J.E. Spanier, L.W. Martin, Defect-Induced, Ferroelectric-Like Switching and Adjustable Dielectric Tunability in Antiferroelectrics, Adv. Mater., 35 (2023), Article 2300257

[64] S.E. Park, T.R. Shrout, Ultrahigh Strain and Piezoelectric Behavior in Relaxor based Ferroelectric Single Crystals, J. Appl. Phys., 82 (1997), pp. 1804–1811

[65] J.A. Rodriguez, K. Remack, K. Boku, K.R. Udayakumar, S. Aggarwal, S.R. Summerfelt, F.G. Celii, S. Martin, L. Hall, K. Taylor, T. Moise, H. McAdams, J. McPherson, R. Bailey, G. Fox, M. Depner, Reliability Properties of Low-Voltage Ferroelectric Capacitors and Memory Arrays, IEEE Trans. Device Mater. Reliab., 4 (2004), pp. 436-449

3.6. Supplementary Materials for Chapter 3

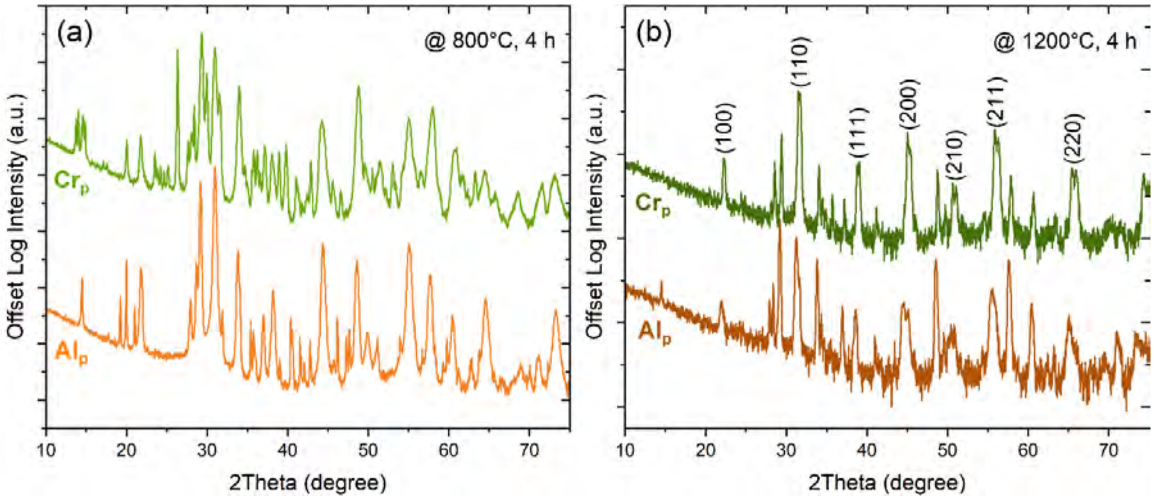

Figure. 3.S1. X-ray diffraction of Cr$_P$ and Al$_P$ powders calcined at (a) 800°C and (b) 1200°C. Note that indexed peaks correspond to perovskite Pb(Zr$_{0.4}$Ti$_{0.6}$)O$_3$.

Figure 3.S1(a) and (b) shows the XRD patterns of Cr$_P$ and Al$_P$ powders calcined at 800°C and 1200°C, respectively. These specific compositions are not likely to form single phase at the same given processing parameters used for other B-site disordered powders. Formation of a single phase was not achievable up to 1200°C; higher temperatures could be not utilized due to significant melting of the powders. It is speculated that the phase development of Al$_P$ powder could be either a kinetically-limited process or high enough formation enthalpy that exceeded the entropy term [1]. It is assumed that phase development of the Cr$_P$ powder is not very different from that of the Al$_P$ powder.

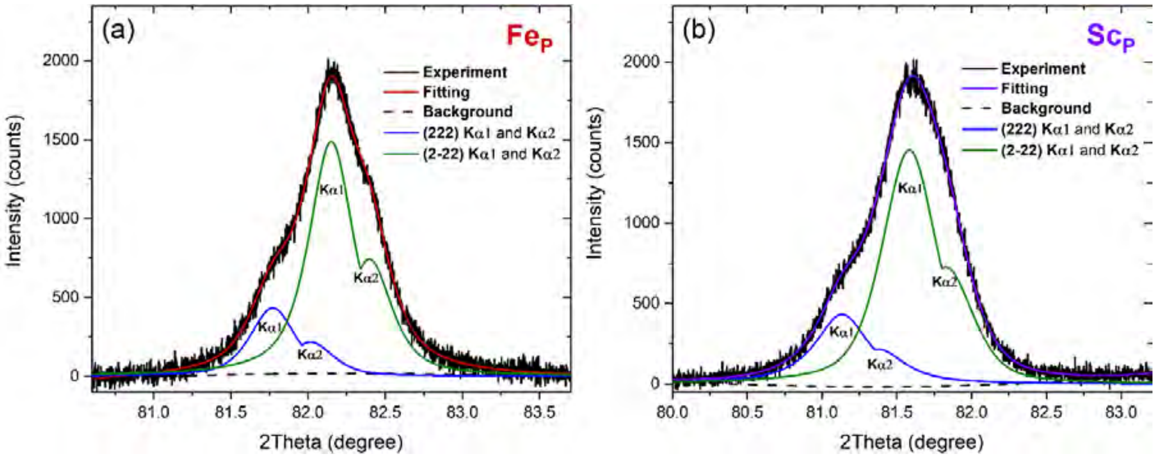

Figure 3.S2. X-Ray diffraction of $\mathrm{Fe_P}$ and $\mathrm{Sc_P}$ powders near {222} peaks with LIPRAS fits

Figure 3.S2. reveals XRD of $\mathrm{Fe_P}$ and $\mathrm{Sc_P}$ powders near {222} peaks with fits performed by Line-Profile Analysis Software (LIPRAS) [2]. In addition to the Rietveld refinement (Figure 3.1(c) and (d)), LIPRAS clearly highlights splitting of the peaks near the {222} family, showing the rhombohedrally distorted structure of the $\mathrm{Fe_P}$ and $\mathrm{Sc_P}$ powders.

Figure 3.S3 shows the temperature dependent XRD data for (a) $\mathrm{Fe_P}$ and (b) $\mathrm{Sc_P}$ powders, respectively. With increasing temperature, the intensity of the {311} and {320} perovskite family peaks are significantly diminished. Additionally, the {222} perovskite family peaks become sharper. These changes are consistent with a symmetry change from R3m rhombohedral to $Pm\bar{3}m$ cubic.

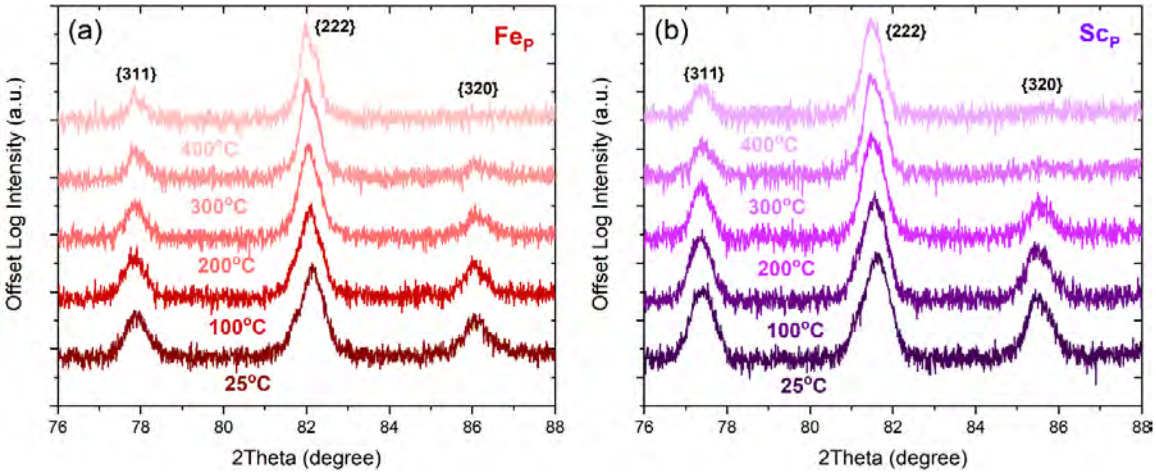

Figure 3.S3. Temperature-dependent X-ray diffraction patterns of (a) Fe_P powder and (b) Sc_P powder for the 2θ range of 76 to 88° from room temperature to 400℃.

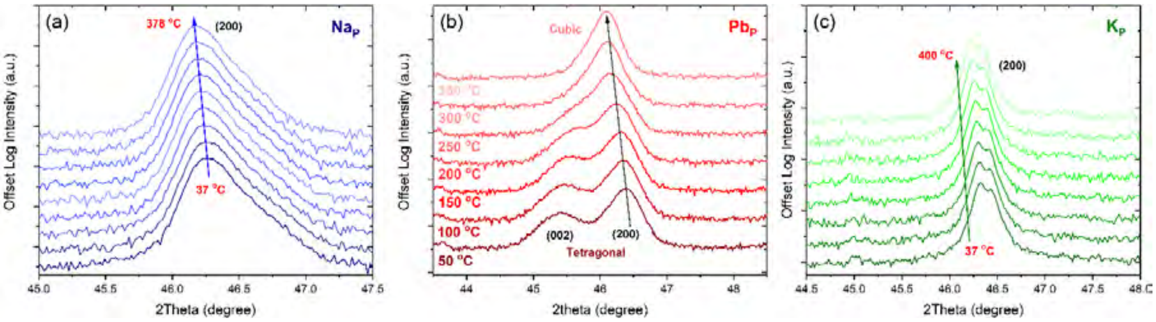

Figure 3.S4. Temperature-dependent X-ray diffraction data of the (a) Na_P powder, (b) Pb_P powder, and (c) K_P powder up to 400℃. An enlarged view near the (002)/(200) perovskite peaks is shown.

The Pb_P powder shows evidence of a phase transition from tetragonal to cubic around 250℃ [3]. In contrast, the (200) peak of Na_P and K_P powders shift toward lower 2θ due to thermal expansion and not to a phase change

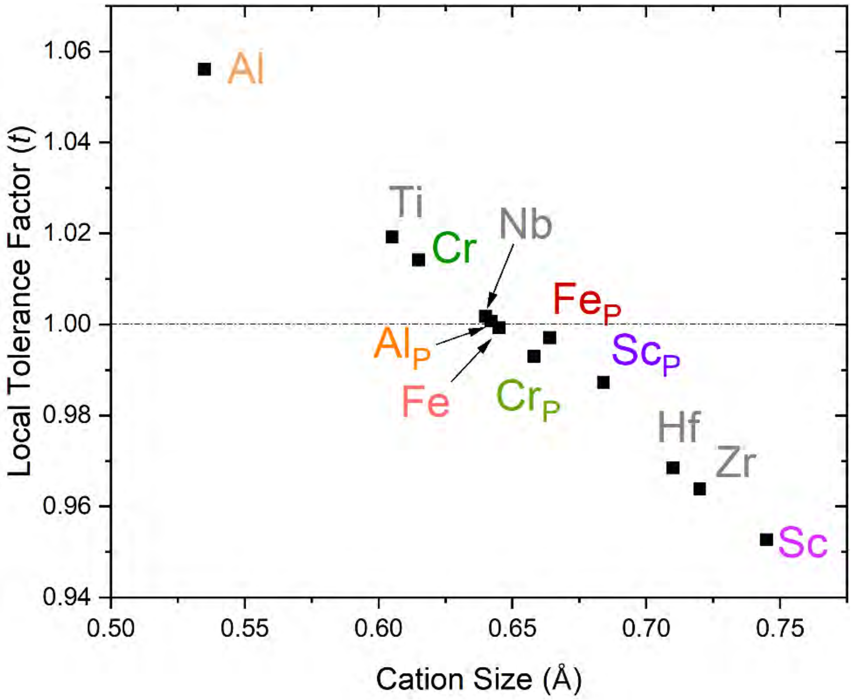

Figure 3.S5. Local tolerance factor for individual cations utilized for the design of B-site HEPOs. Note that Mn_P was not considered here due to poor electrical properties.

The local tolerance factor map is shown in Fig. S5. Given the assumption that Pb occupies the A-site, the local tolerance factor was calculated for the individual elements used for the B-site disordered HEPOs. For example, the local tolerance factor with only Al on the B-site was approximately 1.06, while that of Sc was 0.95. Based on this map, the standard deviation in the local tolerance factor map corresponding to Al_P and Sc_P describes variation in the local tolerance factor in each composition. The standard deviation was 0.04 for Al_P, and 0.03 for Sc_P, suggesting more random bonding or lattice distortion in Al_P composition, compared to Sc_P.

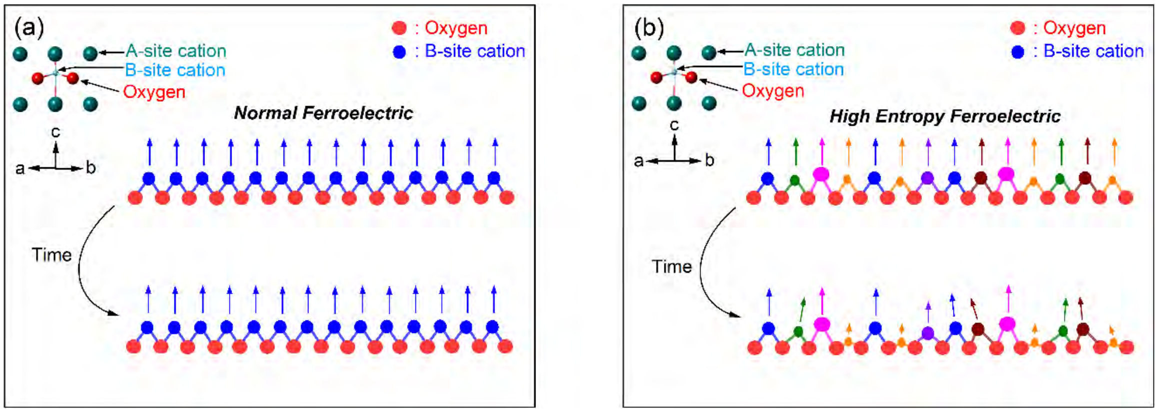

Figure 3.S6. Schematic illustration of polarization relaxation (stability) for (a) a normal ferroelectric and (b) a high entropy ferroelectric.

Figure 3.S6 (a) and (b) illustrates the difference between a normal ferroelectric such as $PbTiO_3$ and a high entropy ferroelectric in terms of polarization relaxation. In normal ferroelectrics, the polarization is well-preserved as a function of time after removal of the applied field, as shown in Figure 3.S6(a). In contrast, given the local size and charge fluctuations in HEPOs, polar correlation is broken up effectively, resulting in faster polarization relaxation. For example, Al^{3+} is prone to relatively short and strong bonding, and has no low-lying d^0 orbitals to favor off-centering in the octahedra. This in turn destabilizes long-range ferroelectric ordering, producing faster relaxation.

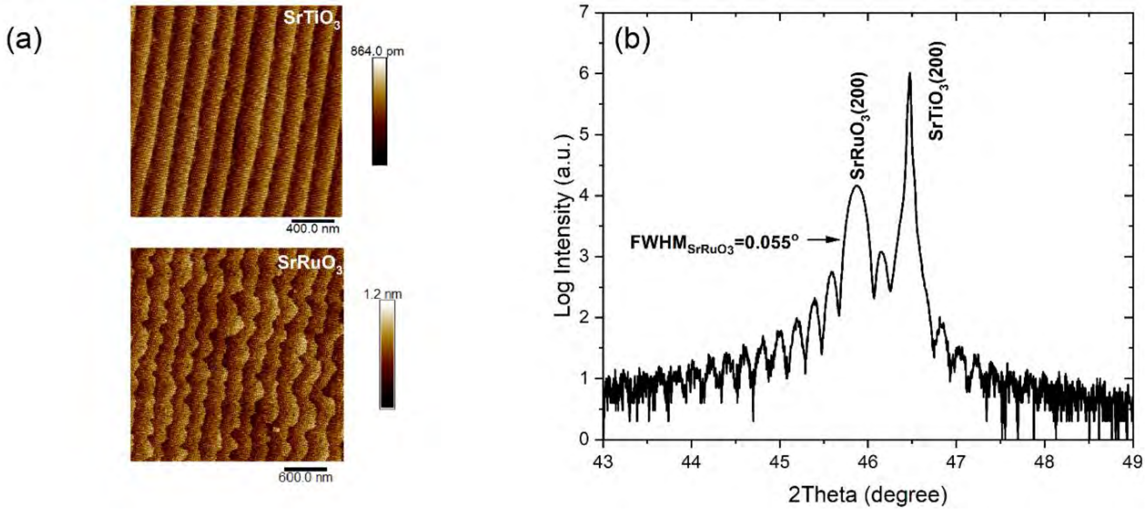

Figure 3.S7. (a) Atomic Force Microscope (AFM) image of an etched and annealed SrTiO$_3$ single crystal substrate (Top) and deposited SrRuO$_3$ film (Bottom) and (b) XRD of the SrRuO$_3$ film on the etched and annealed SrTiO$_3$.

To obtain an atomically flat SrTiO$_3$ (STO) substrate, buffered hydrofluoric (5.6 M HF (49%) + 10.6 M NH$_4$F (40%)) acid etching (pH level of 4.5 for 10 seconds) followed by a rinse with DI water and high temperature annealing (1200℃ for 40 min) was conducted. This treatment resulted in an STO substrate with a root-mean-square (RMS) roughness of 0.130 nm. The AFM of the deposited SRO revealed an RMS roughness of 0.175 nm with a clear step and terrace morphology. Figure 3.S7 (b) shows a typical XRD of the SRO/STO, where the thickness fringes indicate a sharp interface, consistent with the AFM findings. The rocking curve of the SRO is 0.055°. These results demonstrated reasonably good structural quality of the SRO/STO growth template for the deposition of the HEPO films.

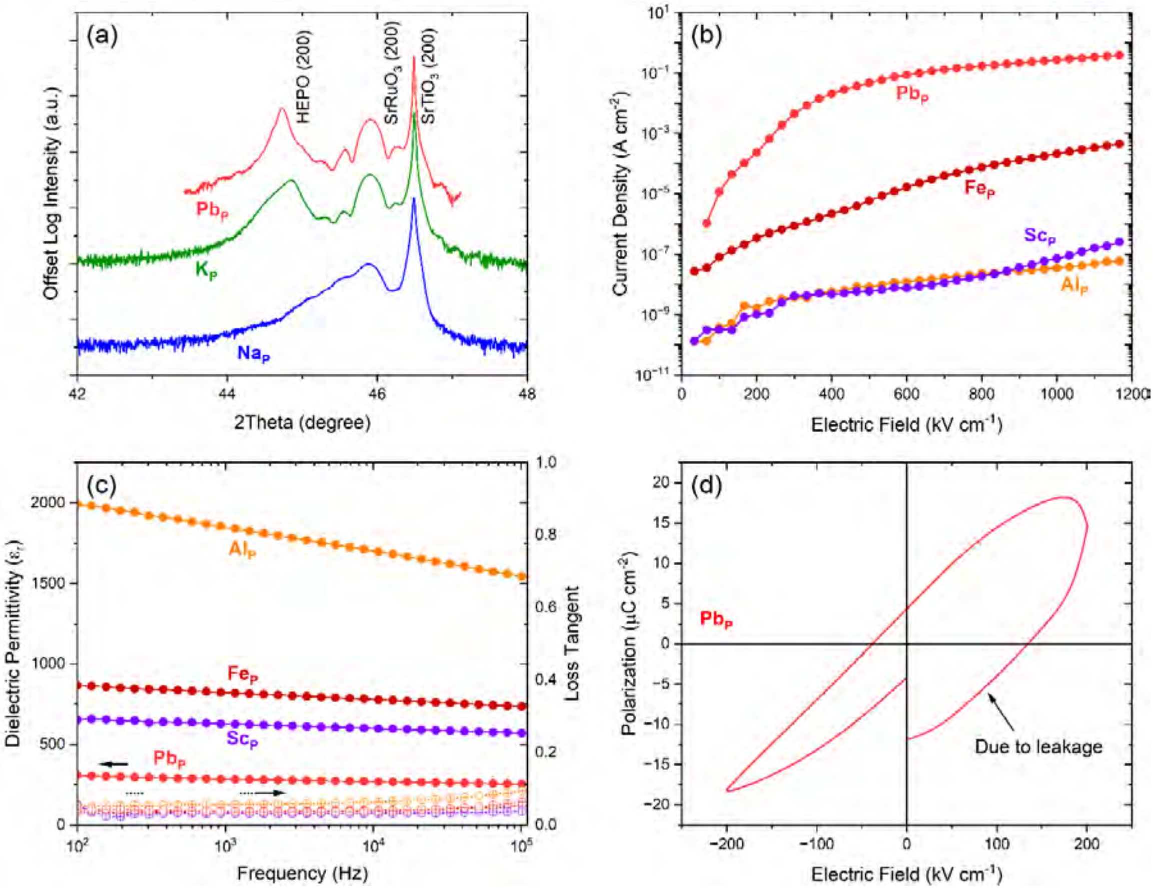

Figure 3.S8. (a) XRD of A-site disordered films prepared on SRO/STO near {002} family of the perovskite peaks. (b) Current density and (c) the relative dielectric permittivity and loss tangent of a Pb$_P$ film, compared to the B-site disordered HEPO films. (d) P-E loop of a Pb$_P$ film measured at 10 kHz for an applied electric field of 200 kV cm^{-1}.

Figure 3.S8(a) represents the XRD of A-site disordered HEPO films. The films were deposited using following processing parameters; a laser energy of 1.5 J cm^{-2}, a working distance of 5.9 cm, laser frequency of 5 Hz, a substrate temperature of 575°C, and deposition pressures of 70 mTorr for the Pb$_P$ film and 50 mTorr for Na$_P$ and K$_P$ films. It is important to highlight that the XRD patterns corresponds to the highest quality samples obtained. The results were not reproducible due to significant sample-to-sample variation particularly for Na$_P$ and K$_P$ samples. Presumably, 1 % excess Bi, Na, and K in the ceramic

target were not enough to compensate for volatility at the given processing conditions, leading to poor reproducibility and large sample-to-sample variation [4–6]. Consequently, further investigation on $\mathrm{Na_P}$ and $\mathrm{K_P}$ film were excluded for this study.

The $\mathrm{Pb_P}$ film exhibited relatively better reproducibility in deposition among the A-site disordered films. The current density and dielectric properties of a $\mathrm{Pb_P}$ film measured at room temperature were compared with the B-site disordered films, as shown in Figure 3.S8(b) and S8(c), respectively. The current density of the $\mathrm{Pb_P}$ film was more than 6 orders of magnitude higher than that of $\mathrm{Sc_P}$ and $\mathrm{Al_P}$ films. At room temperature, a relative dielectric permittivity of approximately 300 with loss tangent below 0.04 was achieved. In Figure 3.S8(d), highly bloated P-E loop was observed for an applied electric field of 200 kV cm^{-1}. The film was broken down when electric field exceeds 250 kV cm^{-1}. Due to the high leakage, further electrical measurement was not performed.

Table 3.S1. Comparison table of Full-Width-at-Half-Maximum with other materials

Materials (film/substrate)	FWHM of film (degree)	FWHM of substrate (degree)	Reference
$Al_P/SrTiO_3$	0.041	0.012	[This work]
Fe_P / $SrTiO_3$	0.046	0.012	[This work]
Sc_P / $SrTiO_3$	0.061	0.012	[This work]
Pb_P / $SrTiO_3$	0.057	0.012	[This work]
PMN-PT/$NdScO_3$	0.038	0.006	[7]
PMN-PT/$Nd_{0.5}Sm_{0.5}ScO_3$	0.035	0.006	[7]
PMN-PT/$SmScO_3$	0.053	0.005	[7]
PMN-PT/$NdScO_3$	0.041	0.007	[8]
PST/$DyScO_3$	0.034	0.007	[9]
$(La,Pr,Nb,Sm,Eu)NiO_3/NdGaO_3$	0.085	0.01	[10]
$Ba(Zr,Sn,Ti,Hf,Nb)O_3/SrTiO_3$	0.06	Not provided	[11]
$(La,Lu,Y,Gd,Ce)AlO_3/LaAlO_3$	0.39	Not provided	[12]

PMN-PT for reference [7] and [8] is $0.68PbMg_{1/3}Nb_{2/3}O_3$-$0.32PbTiO_3$. PST for reference [9] is $PbSc_{1/2}Ta_{1/2}O_3$. Please note that Cr_P, Kp, and Na_P films are excluded due to poor quality and reproducibility. Comparison results shows that B-site disordered and Pb_P film used for this study are comparable to many Pb-based relaxor ferroelectric and even better than other high entropy perovskite oxides.

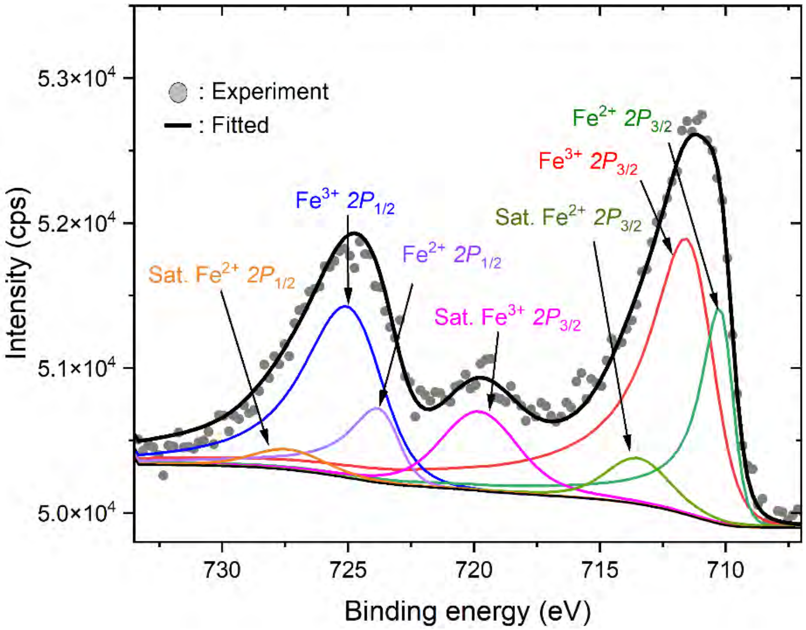

Figure 3.S9. X-ray photoelectron spectroscopy spectra corresponding to Fe 2p $_{3/2}$ obtained from the Fe$_P$ film. The grey dots are the experimental data and the black line is the fit.

Figure 3.S9 shows the Fe 2p spectrum fitted over the binding energy range from 705 – 735 eV. The grey dots correspond to the experimental data and the black line represents the fit. From the deconvolution of Fe 2p spectrum, the binding energy of Fe^{2+} 2p$_{3/2}$ and Fe^{3+} 2p$_{3/2}$ were 710.1 and 711.3 eV, respectively. This energy range is close to that reported for BiFeO$_3$, Fe doped BaTiO$_3$, Fe$_3$O$_4$ powders, and oxide layers on polycrystalline iron [13-15]. The broad satellite at 719.7 eV (Sat. Fe^{3+} 2p$_{3/2}$) is characteristic of Fe^{3+} [16]. Another satellite peak at 713.8 eV (Sat. Fe^{2+} 2p$_{3/2}$) supports the existence of Fe^{2+} species [17]. The concentration of Fe^{2+} was estimated to be 29% based on the corresponding area. It is not uncommon to achieve undesired valence state mixtures of multivalent ion, particularly under either high vacuum or highly oxidizing environment [18,19]. This XPS result supports the high leakage current of the Fe$_P$ film (Figure 3.3(a)).

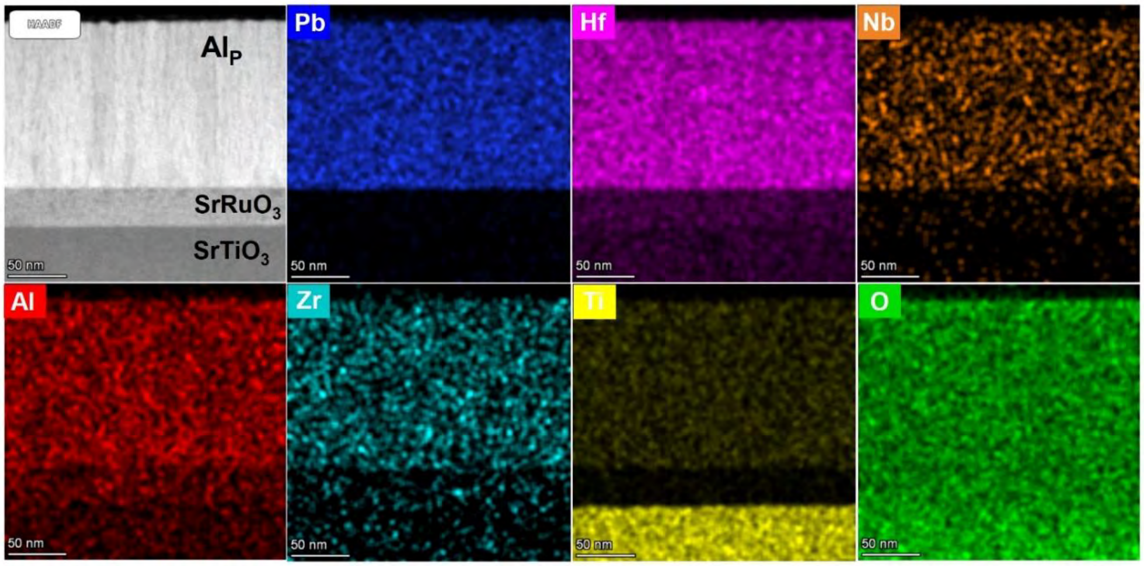

Figure 3.S10. High-Angle-Annular Dark Field Signal (HAADF) and X-ray Energy Dispersive Spectroscopy (XEDS) images of an Al_P film. Please note that the scale bar corresponds to 50 nm, and compositional segregation was not observed for Al_P film at this length scale.

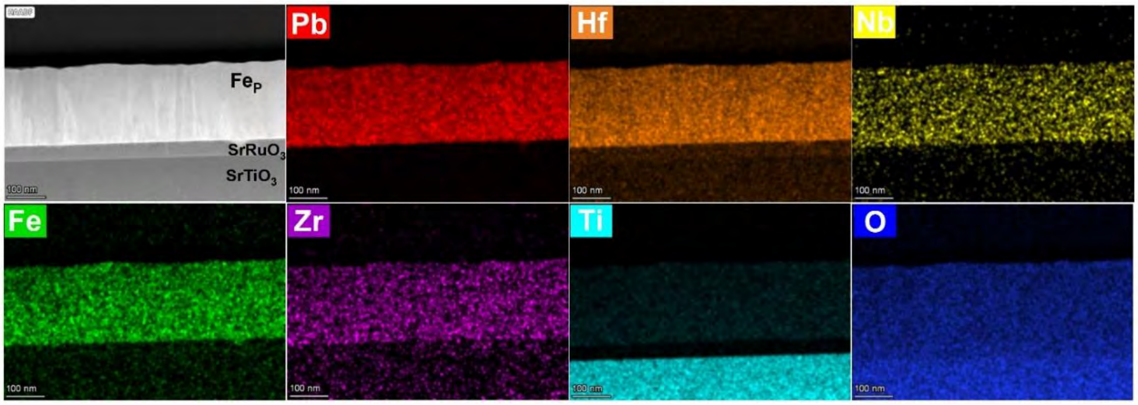

Figure 3.S11. HAADF and XEDS images of an Fe_P film. Please note that the scale bar corresponds to 100 nm and compositional segregation was not observed for Fe_P film at this length scale.

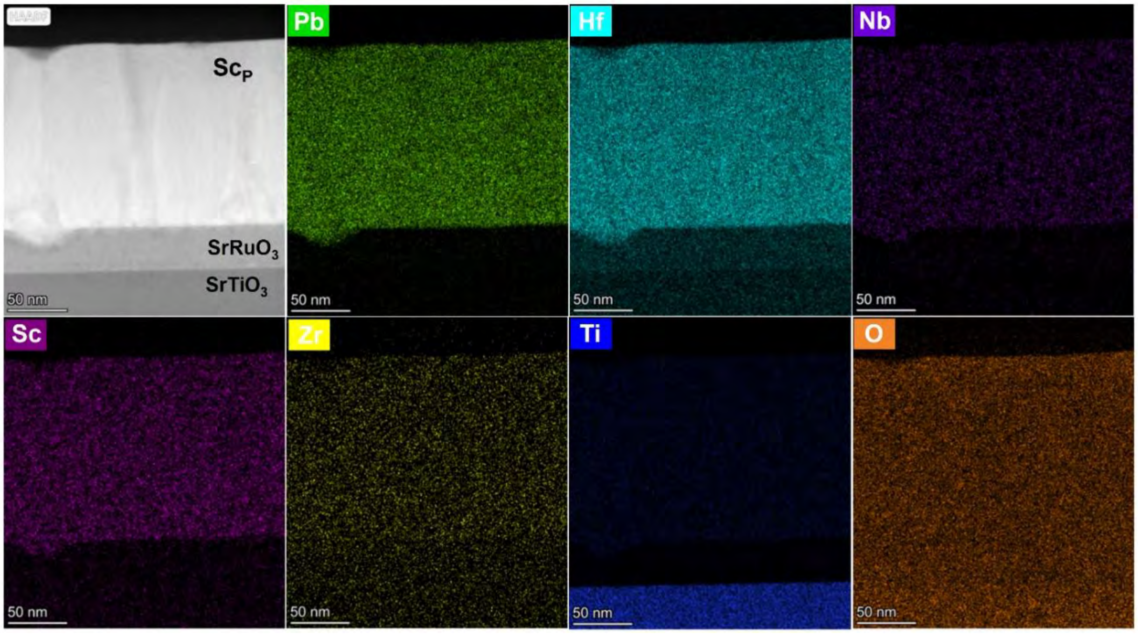

Figure 3.S12. HAADF and XEDS images of an Sc$_P$ film. Please note that the scale bar corresponds to 50 nm and compositional segregation was not observed for Sc$_P$ film at this length scale.

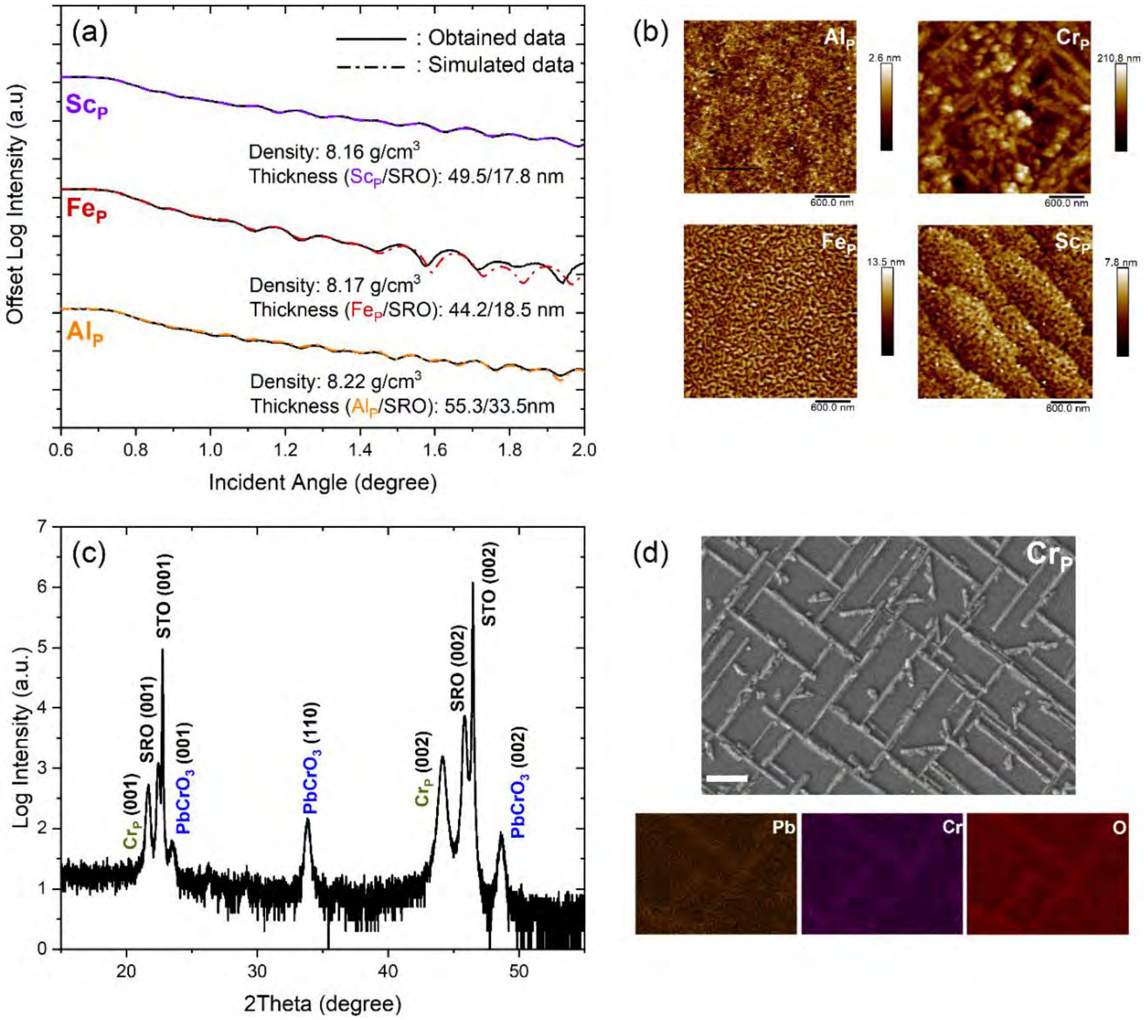

Figure 3.S13. (a) X-ray Reflectivity (XRR) of Al_P, Fe_P, and Sc_P films deposited on SRO/STO. (b) AFM scan of all B-site disordered HEPO films. (c) XRD 2theta scan of Cr_P film to show phase segregation of $PbCrO_3$ from the Cr_P parent composition. (d) (Top) Field Emission Scanning Electron Microscope (FESEM) and (Bottom) compositional mapping by Energy Dispersive Spectroscopy (EDS). Scale bar corresponds to 1 μm. EDS maps support the fact that the surface structure is attributed to chemical segregation of $PbCrO_3$.

In Figure 3.S13(a), thickness of the B-site disordered HEPO films were calibrated based on growth rate/pulse estimated from fitting of X-ray reflectivity (XRR). From the XRR, the growth rates for Al_P, Fe_P, and Sc_P films were estimated to be approximately 0.02 nm/pulse, 0.03 nm/pulse, and 0.02 nm/pulse, respectively.

Figure 3.S13(b) shows Atomic Force Microscope (AFM) images of $\mathrm{Al_P}$, $\mathrm{Cr_P}$, $\mathrm{Fe_P}$, and $\mathrm{Sc_P}$ films. It is clear that the $\mathrm{Cr_P}$ film exhibits a significantly higher surface roughness compared to other films. XRD patterns (Figure 3.S13(c)) for the $\mathrm{Cr_P}$ film indicate formation of $\mathrm{PbCrO_3}$ segregating from the host $\mathrm{Cr_P}$ composition. Top view FESEM image further shows well-organized surface structures on the $\mathrm{Cr_P}$ films. Based on the EDS, the surface structure could be originating from the $\mathrm{PbCrO_3}$ segregation, which is consistent with the XRD results.

Given the existence of more than a 5 % lattice mismatch between HEPO films and the $\mathrm{SrTiO_3}$ substrate, together with HEPO film thicknesses of approximately 300 nm , it is not surprising to observe 3D island features on $\mathrm{Al_P}$ and $\mathrm{Fe_P}$ films. The slightly higher roughness of the $\mathrm{Fe_P}$ film, compared to the $\mathrm{Al_P}$ film could be, at least in part, attributed to the faster growth rate [20,21]. In contrast, the $\mathrm{Sc_P}$ film exhibits a persistent step-flow growth mode with some 3D island features on the step terrace. This could be related to sample-to-sample variation in the miscut angle of the $\mathrm{SrTiO_3}$ substrate because 3D island feature could also be obtained for $\mathrm{Sc_P}$ films under the same processing conditions, as shown in Figure 3.S14(b) [22,23]. Despite the variations in the surface features associated with growth mode, negligible change was observed in crystalline quality of the $\mathrm{Sc_P}$ film at the given processing parameters (see Figure 3.S14(a)).

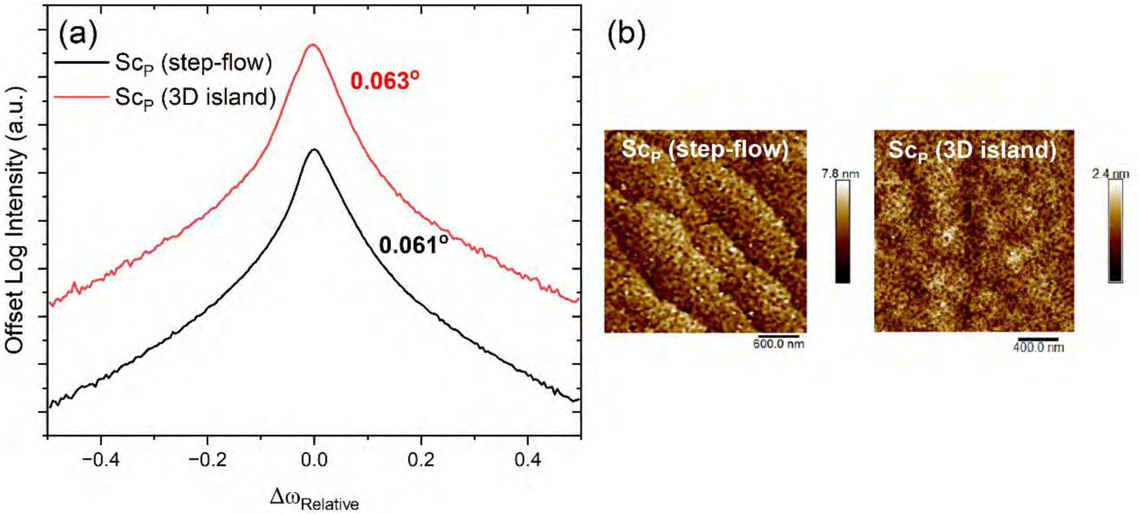

Figure 3.S14. (a) Rocking curve and (b) AFM of Sc_P films with different surface features. Note that negligible difference was obtained for crystalline quality despite different growth mode driven features on the surfaces.

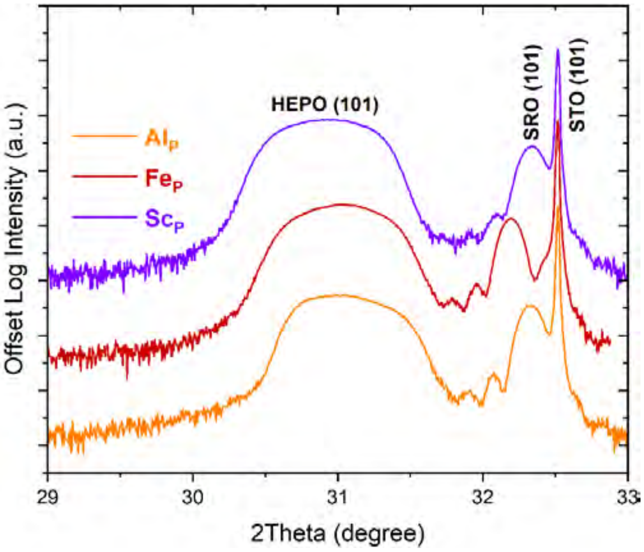

Figure 3.S15. XRD scan along (101) direction for Al_P, Fe_P, and Sc_P films

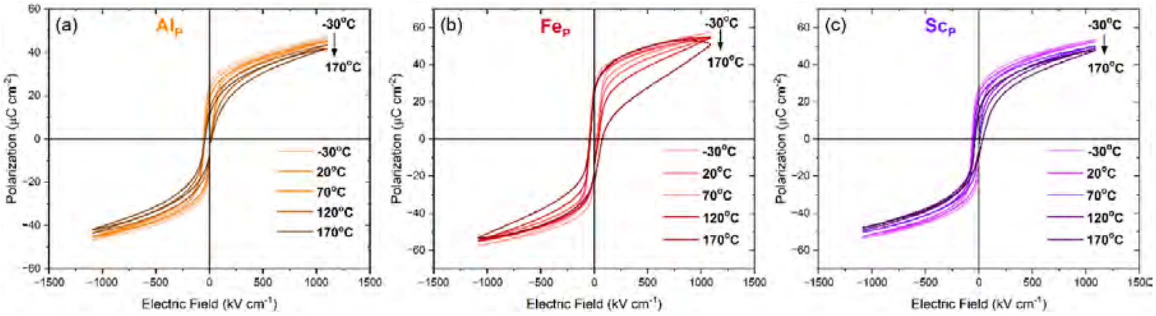

Figure 3.S16. (a) Temperature dependent P-E loops of Al$_P$ films, (b) Temperature dependent P-E loops of Fe$_P$ films, and (c) Temperature dependent P-E loops of Sc$_P$ films from -30℃ to 170℃.

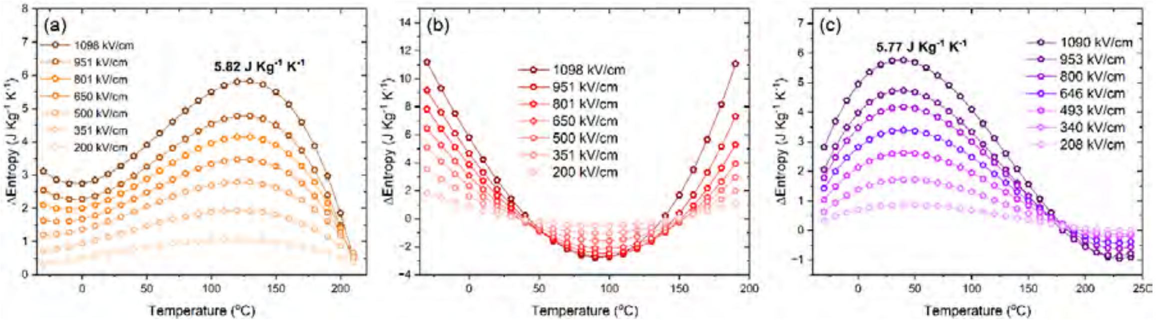

Figure 3.S17. Electrocaloric entropy change of (a) Al$_P$ film, (b) Fe$_P$ film, and (c) Sc$_P$ film deduced from Maxwell relations.

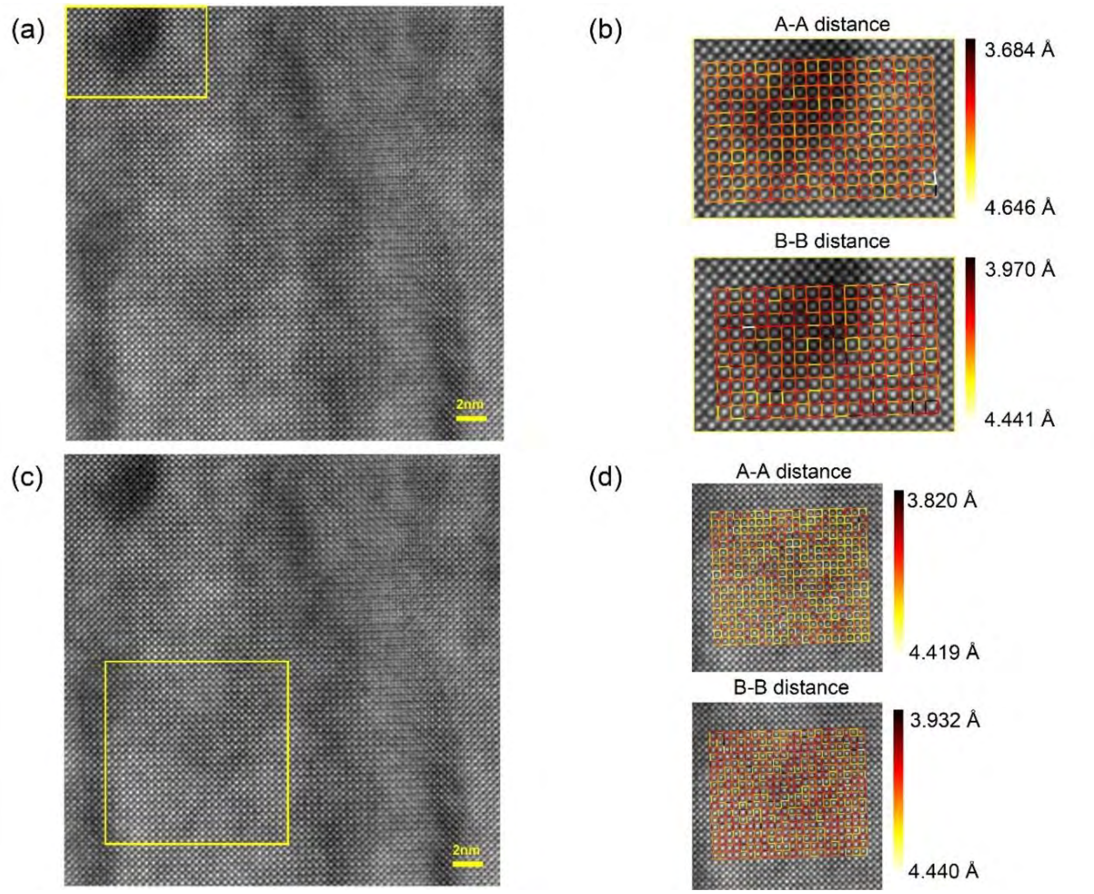

Figure 3.S18. High resolution TEM (HRTEM) image of an Al_P film with different areas of focus (a) a dark region and (c) a lighter region. Corresponding distance estimation (b) for a dark region and (d) for a lighter region. The A-A distance represents the distance between one A-site cation and the adjacent A-site cation; the B-B distance is defined similarly. The image is approximately from the middle of the Al_P film.

Figure 3.S18 shows drift corrected Annular Dark Field-Scanning Transmission Electron Microscope (ADF-STEM) images acquired along the [100] zone axis of the Al_P film. Patchy dark regions were observed distributed uniformly over the entire thickness of the sample. The yellow box highlights the areas selected for the distance estimation. Figure 3.S18(a) is localized on a dark region, while Figure 3.S18(c) is on a lighter region. Figure 3.S18(b) and (d) shows the A-A and B-B distance estimations for the two regions, respectively. It was found that the average A-A and B-B distances corresponding to Figure

3.S18(a) are 4.172±0.09 Å and 4.175±0.069 Å, respectively. Similarly, the average A-A and B-B distance correspond to Figure 3.S18(c) are 4.184±0.092 Å and 4.181±0.078 Å, respectively. A similar value between A-A and B-B distance could be related to pseudo-cubic structure of Al_P, as anticipated by tolerance factor. Similar investigations were reported for normal ferroelectric $Pb(Zr_{0.2}Ti_{0.8})O_3$ (PZT (20/80)) thin films on $SrRuO_3/SrTiO_3$ [24,25]. A gradual decrease in the Pb-Pb spacing was observed near the PZT (20/80) thin film/SRO interface due to strain relaxation caused by lattice mismatch between PZT (20/80) and STO substrate. However, this gradual decrease was confined within a few tens of unit cells. Beyond this region, the Pb-Pb lattice spacing in PZT (20/80) thin films were 4.15±0.02 Å, resulting in less than 0.5 % variation in the lattice spacing [25]. In contrast, the A-A distance (or B-B distance) estimation for the Al_P HEPO film shows no visually gradual decrease in the lattice spacing from interface. Instead, the spacing was spatially random, causing 1.7 % - 2.2 % variations in either the A-A or B-B lattice spacing. Given that significantly smaller substrate strain effect, the ~2 % variation is substantially larger than that of a normal ferroelectric such as PZT (20/80). This variation in the lattice spacing emphasizes the composition-induced structural distortion that induces randomness to the bonding and local elastic fields, giving rise to the relaxor character of the Al_P film. This result is consistent with the large variation in local tolerance factor (Figure 3.S5) in Al_P.

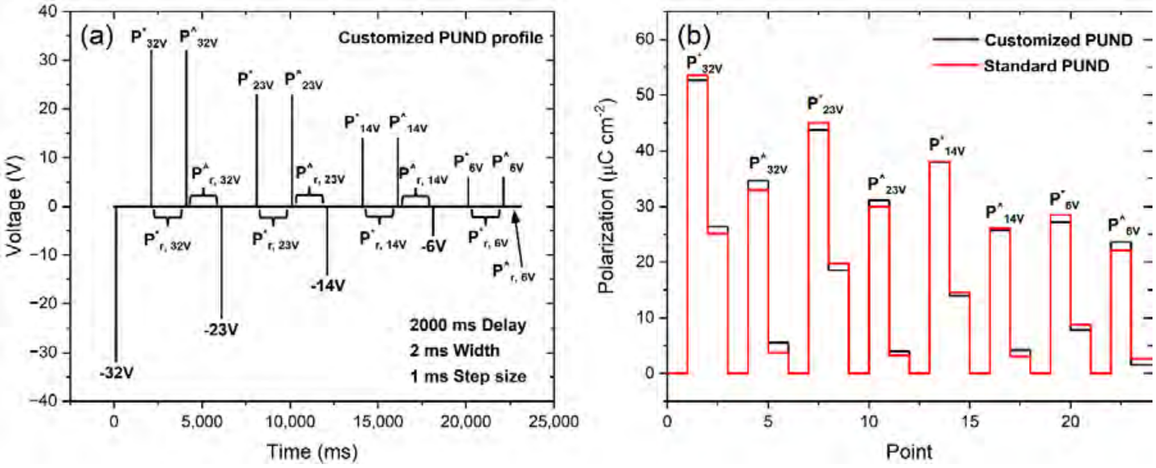

Figure 3.S19 (a) Schematic of customized PUND voltage profile. (b) Comparison between standard PUND profile and customized PUND profile.

To understand the customized PUND profile, the polarization values obtained from Vision software (Radiant Technology, Inc) will be briefly discussed, using the data in Figure 3.S19 (a). The very first pulse in the negative direction, denoted ‘-32V,’ corresponds to a preset voltage to align dipoles in a “known” direction. After a delay time set by the user, the first measurement pulse was applied with the desired voltage, denoted here as ‘$\mathrm{P}^{*}_{32\mathrm{V}}$’. This polarization contains ‘Remanent polarization + Non-Remanent polarization (switching and leakage)’. Another measurement was performed when the voltage = 0, after the delay time. Here, this value is presented as ‘$\mathrm{P}^{*}_{\mathrm{r},32\mathrm{V}}$’. After the delay time, the second measurement pulse was applied at the same voltage as the first, but this polarization contains ‘Non-remanent polarization’ ($\mathrm{P}^{\wedge}_{32\mathrm{V}}$). Then, another measurement at zero voltage was performed ($\mathrm{P}^{\wedge}_{\mathrm{r},32\mathrm{V}}$), after the delay time. The ‘Remanent polarization’ was extracted from dP $= \mathrm{P}^{*}_{32\mathrm{V}} - \mathrm{P}^{\wedge}_{32\mathrm{V}}$ ($\approx \mathrm{P}^{*}_{\mathrm{r},32\mathrm{V}} - \mathrm{P}^{\wedge}_{\mathrm{r},32\mathrm{V}}$). Figure 3.S19 (b) compares customized PUND profile and standard PUND. This comparison validates the customized PUND profile’s effectiveness.

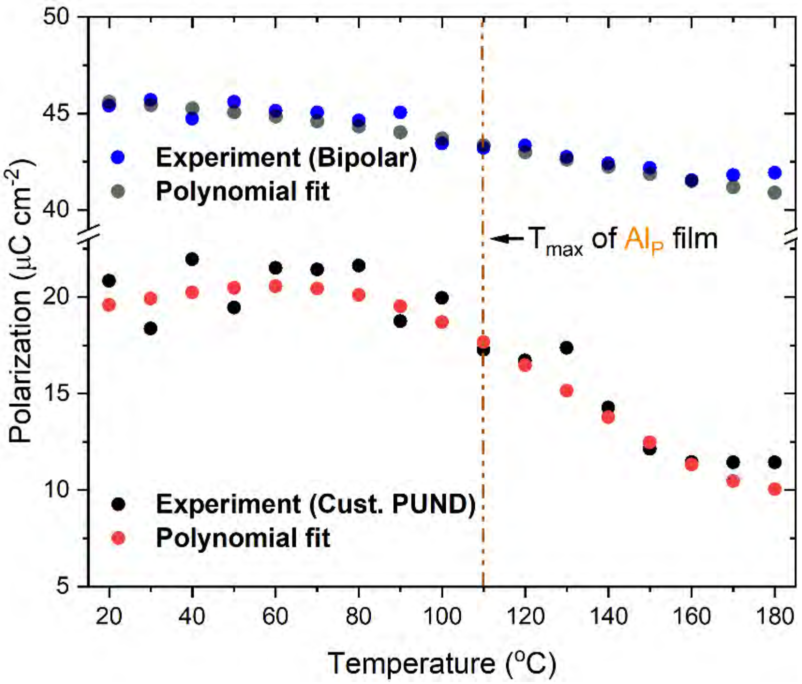

Figure 3.S20. Polarization vs temperature curve from standard bipolar measurement (blue) and from the customized PUND measurement (red). Note that 4th order polynomial fits were applied for both data. T_{max} of Al_P film is shown as dotted line at around 110°C.

Figure 3.S20 shows polarization vs. temperature curve and 4th order polynomial fits for the measurement from standard-bipolar hysteresis loop (blue) and measurement from customized PUND (red). The smaller polarization value for the customized PUND data is seen because it uses the remanent polarization. A larger drop in polarization is apparent in the vicinity of T_{max} of the Al_P film (dotted line) for the customized PUND data in which the polarization was allowed to decay. Thus, the customized PUND generate relatively larger electrocaloric responses, originating from the instability of induced polarization in the Al_P film.

Table 3.S2. Comparison table of HEPOs with other electrocaloric materials

	ΔT (K)	ΔS (J kg^{-1} K^{-1})	ΔE (kV cm^{-1})	ΔT/ΔE (K m kV^{-1})	T_{peak} (K)	T_{span} (K)	T_{max} (°C)	J (A cm^{-2}, ×10^{-9})	T_B (°C)	Ref.
Al_P	7.4	5.8	1100	0.7	413	90	383	8.2	215	This work
Sc_P	5.7	5.8	1100	0.5	323	100	498	6.0	245	This work
Al_P (c)	14.9	11.5	1100	1.4	413	50	383	8.2	215	This work
0.67PMN-0.33PT	14.5	N/A	600	2.4	425	20	425	N/A	N/A	[24]
$(Pb_{0.8}Ba_{0.2})ZrO_3$	45.3	46.9	598	7.6	290	12	404	N/A	N/A	[25]
$Pb(Sc_{0.5}Ta_{0.5})O_3$	15.7	16	287	5.5	288	5	298	N/A	N/A	[26]
$Pb(Zr_{0.95}Ti_{0.05})O_3$/ $Pb(Zr_{0.95}Ti_{0.05})O_3$	24.8	20.5	566	4.4	398	25	363	N/A	N/A	[27]

Table 3.S2 represents a summary of B-site disordered HEPOs with several key parameters for the estimation of electrocaloric performance. For comparison, several other Pb-based perovskite films are also included. Note that Al_P (c) corresponds to data obtained from customized PUND measurement. It is important to note that T_{Peak} is the temperature at which the maximum electrocaloric temperature change occurs and T_{Span} is the temperature range where 80% of ΔT_{ECE} can be achieved. Notably, HEPOs (both Sc_P and Al_P film) exhibit a wide T_{Span}, which could be advantageous for application requiring a wide operating temperature range. For example, $(Pb_{0.8}Ba_{0.2})ZrO_3$ demonstrates a ΔT_{ECE} of 45.3 K near room temperature. Such a high ΔT_{ECE} may facilitate high cooling efficiency. However, its narrow T_{Span} of 12 K limits the full utilization of the good efficiency to a very restricted temperature range. In contrast, although the HEPOs exhibit a relatively smaller ΔT_{ECE}, their much broader T_{Span} provides greater flexibility in operating temperature. In the comparison table, T_{max}, J (current density), T_B (Burn's temperature) are also listed together.

3.6.1 Reference for Supplementary Material

[1] Y. Son, W. Zhu, S.E. Trolier-Mckinstry, Electrocaloric Effect of Perovskite High Entropy Oxide Films, Adv. Electron. Mater., 8 (2022), p. 220352

[2] G. Esteves, C.M. Fancher, LIPRAS: Line-Profile Analysis Software, (2017), pp. 1-4

[3] Z. Liu, S. Xu, T. Li, B. Xie, K. Guo, J. Lu, Microstructure and ferroelectric properties of high-entropy perovskite oxides with A-site disorder, Ceram. Int., 47 (2021), pp. 33039–33046

[4] M. Zhu, X. Shang, G. Chang, M. Li, X. Liu, T. Zhou, Y. He, Pulsed Laser Deposition of Single-Phase Lead-free NKLNST Thin Films with K- and Na-excess Targets, J. Alloys. Compd., 567 (2013), pp. 97–101

[5] A. Hamieh, F. Ponchel, S. Barrau, D. Remiens, Synthesis of Lead-free $(Bi_{0.5}Na_{0.5})TiO_3$ Thin Film by RF Magnetron Sputtering: Impact of Na on the Properties of Film, Ferroelectrics, 556 (2020), pp. 79–86

[6] Y. Wu, X. Wang, C. Zhong, L. Li, Effect of Na/K Excess on the Electrical Properties of $Na_{0.5}Bi_{0.5}TiO_3$–$K_{0.5}Bi_{0.5}TiO_3$ Thin Films Prepared by Sol–gel Processing, Thin Solid Films, 519 (2011), pp. 4798–4803

[7] J. Kim, A. Kumar, Y. Qi, H. Takenaka, P. J. Ryan, D. Meyers, J.W. Kim, A. Fernandez, Z. Tian, A.M. Rappe, J.M. LeBeau, L.W. Martin, Coupled Polarization and Nanodomain Evolution Underpins Large Electromechanical Responses in Relaxors, Nat. Phys. 18, (2022), pp. 1502–1509

[8] S. Saremi, J. Kim, A. Ghosh, D. Meyers, L.W. Martin, Defect-Induced (Dis)Order in Relaxor Ferroelectric Thin Films, Phys. Rev. Lett., 123 (2019), Article 207602

[9] A. Fernandez, J. Kim, D. Meyers, S. Saremi, L.W. Martin, Finite-Size Effects in Lead Scandium Tantalate Relaxor Thin Films, Phys. Rev. B., 101 (2020), Article 094102

[10] R.K. Patel, S.K. Ojha, S. Kumar, A. Saha, P. Mandal, J.W. Freeland, S. Middey, Epitaxial Stabilization of Ultra Thin Films of High Entropy Perovskite, Appl. Phys. Lett., 116 (2020) Article 71601

[11] Y. Sharma, B.L. Musico, X. Gao, C. Hua, A.F. May, A. Herklotz, A. Rastogi, D. Mandrus, J. Yan, H.N. Lee, M.F. Chisholm, V. Keppens, T.Z. Ward, Single-Crystal High Entropy Perovskite Oxide Epitaxial Films, Phys. Rev. Mater., 2 (2018), Article 060404

[12] Z.J. Corey, P. Lu, G. Zhang, Y. Sharma, B.X. Rutherford, S. Dhole, P. Roy, Z. Wang, Y. Wu, H. Wang, A. Chen, Q. Jia, Structural and Optical Properties of High Entropy (La,Lu,Y,Gd,Ce)AlO_3 Perovskite Thin Films, Adv. Sci. 9 (2022), Article 2202671

[13] G. A. Gomez-Iriarte, A. P-Madrigal, L. A. S. Oliveira, J. P. Sinnecker, XPS Study in $BiFeO_3$ Surface Modified by Argon Etching, Materials, 15 (2022), Article 4285

[14] B. Kuo, X. Wang, E. Tian, H. Song, Q. Zhao, Z. Cai, W. Feng, L. Li, Giant Permittivity and Low Dielectric Loss of Fe doped $BaTiO_3$ Ceramics: Experimental and First-Principles Calculations, J. Eur. Ceram. Soc., 38 (2018), pp. 1562-1568

[15] T-C. Lin, G. Seshadri, J. A. Kelber, A Consistent Method for Quantitative XPS Peak Analysis of Thin Oxide Films on Clean Polycrystalline Iron Surfaces, Appl. Surf. Sci., 119 (1997), pp. 83-92

[16] C. R. Brundle, T. J. Chuang, K. Wandelt, Core and Valence Level Photoemission Studies of Iron Oxide Surfaces and The Oxidation of Iron, Surf. Sci., 68 (1977), pp. 459-468

[17] G. Bhargava, I. Gouzman, C. M. Chun, T. A. Ramanarayanan, S. L. Bernasek, Characterization of the “Native” Surface Thin Film on Pure Polycrystalline Iron: A High Resolution XPS and TEM Study, Appl. Surf. Sci., 253 (2007), pp. 4322-4329

[18] C-E. Bejjit, V. Roge, C. Cachonicnlle, C. Hebert, J. Perriere, E. Briand, E. Millon, Iron Oxide Thin Films Grown on (001) Sapphire Substrate by Pulsed Laser Deposition, Thin Solid Films, 745, (2022), Article 139101

[19] G. N. Kotsonis, P. B. Meisenheimer, L. Miao, J. Roth, B. Wang, P. Shafer, R. Engel-Herbert, N. Alem, J. T. Heron, C. M. Rost, J-P. Maria, Property and Cation Valence Engineering in Entropy-Stabilized Oxide Thin Films, Phys. Rev. Mater., 4 (2020), Article 100401

[20] M.D. Nguyen, E.P. Houwman, M. Dekkers, G. Rijnders, Strongly Enhanced Piezoelectric Response in Lead Zirconate Titanate Films with Vertically Aligned Columnar Grains, ACS Appl. Mater. Interfaces, 9 (2017), pp. 9849-9861

[21] L.W. Martin, Y.-H. Chu, R. Ramesh, Advances in the Growth and Characterization of Magnetic, Ferroelectric, and Multiferroic Oxide Thin Films, Mat. Sci. Eng. R Rep., 68 (2010), pp. 89-133

[22] A. Gura, G. Bertino, B. Bein, M. Dawber, Transition Regime from Step-Flow to Step-Bunching in the Growth of Epitaxial $SrRuO_3$ on (001) $SrTiO_3$, Appl. Phys. Lett. 112 (2018), Article 182902

[23] W. Hong, H.N. Lee, M. Yoon, H.M. Christen, D.H. Lowndes, Z. Suo, Z. Zhang, Persistent Step-Flow Growth of Strained Films on Vicinal Substrates, Phys. Rev. Lett. 95 (2005), Article 095501

[24] C-L. Jia, V. Nagarajan, J.Q. He, L. Houben, T. Zhao, R. Ramesh, K. Urban, R. Washer, Unit-Cell Scale Mapping of Ferroelectricity and Tetragonality in Epitaxial Ultrathin Ferroelectric Films, Nat. Mater., 6 (2007), pp. 64-69

[25] C. Huang, Z. Liao, M. Li, C. Guan, F. Jin, M. Ye, X. Zeng, T. Zhang, Z. Chen, Y. Qi, P. Gao, L. Chen, A Highly Strained Phase in $PbZr_{0.2}Ti_{0.8}O_3$ Films with Enhanced Ferroelectric Properties, Adv. Sci., 8 (2021), Article 2003582

[26] Z. Feng, D. Shi, S. Dou, Large Electrocaloric Effect in Highly (001)-Oriented $0.67PbMg_{1/3}Nb_{2/3}O_3$-$0.33PbTiO_3$ Thin Films, Solid State Commun., 151 (2011), pp. 123-126

[27] B. Peng, H. Fan, Q. Zhang A Giant Electrocaloric Effect in Nanoscale Antiferroelectric and Ferroelectric Phases Coexisting in a Relaxor $Pb_{0.8}Ba_{0.2}ZrO_3$ Thin Film at Room Temperature, Adv. Func. Mater., 23 (2013), pp. 2987-2992

[28] V. Kovacova, S. Glinsek, S. Girod, E. Defay, High Electrocaloric Effect in Lead Scandium Tantalate Thin Films with Interdigitated Electrodes, Sensors, 22 (2022), Article 4049

[29] T. Zhang, W. Li, W. Cao, Y. Hou, Y. Yu, W. Fei, Giant Electrocaloric Effect in PZT Bilayer Thin Films by Utilizing the Electric Field Engineering, Appl. Phys. Lett., 108 (2016), Article 162902

Chapter 4

$PbZrO_3$-based Thin Film Capacitor with High Energy Storage Efficiency

4.1 Introduction

Electrical energy storage technology is an enabling technology for portable electronic devices, including cell phones, laptop computers, and electric vehicles. Several different types of energy storage technologies, including mechanical, chemical, electrochemical, and dielectrics are used [1]. Li-ion batteries store energy in a chemical form through a redox reaction that occurs between electrodes separated by electrolytes. Li-ion batteries have large energy densities (75-200 Wh Kg^{-1}) and relatively low power densities (500-2000 W Kg^{-1}) [1,2]. Consequently, these batteries are suitable for application requiring a long-lived stable energy supply [3].

Conversely, dielectric capacitors, which store energy electrostatically, can generate considerable larger power densities ($\sim 10^4$–10^5 W Kg^{-1}) due to their fast charging/discharging rate [4–7]. Moreover, the absence of an electrolyte permits larger voltages (> 5 V) and good reliability, making them strong candidates for power electronics and pulsed power applications [8–11]. However, commercialized dielectric capacitors, such as polypropylene, suffer from energy densities of only a few J cm^{-3} [12]. This makes the capacitors physically bulky, limiting their use in applications requiring compactness and relatively large energy densities.

The discharged-energy density $\mathrm{U_d}$ is given by $\mathrm{U_d} = \int_{\mathrm{P_{rem}}}^{\mathrm{P_{max}}} \mathrm{EdP}$ where $\mathrm{P_{max}}$ is the maximum polarization and $\mathrm{P_{rem}}$ is the remanent polarization. Achieving a high $\mathrm{U_d}$ requires a large induced polarization and a small remanent polarization. Antiferroelectrics have garnered significant attention due to their large polarizations and low remanent polarization [13,14]. The electric-field driven antiferroelectric (AFE) to ferroelectric (FE) phase transition enables large energy storage density, making antiferroelectrics promising candidates for energy storage ceramic capacitors. However, most antiferroelectrics have large hysteresis loss associated with mechanically incompatible AFE/FE interfaces, leading to a deterioration of efficiency [15]. The efficiency, η, can be expressed by $\eta = \mathrm{U_d}/(\mathrm{U_d} + \mathrm{U_{loss}}) \times 100$ (%) where $\mathrm{U_{loss}}$ is the energy loss associated with leakage and hysteresis, extracted from the area inside the polarization-electric field hysteresis loop (P-E loop) [6].

Recently, high efficiency antiferroelectric ceramic compositions was predicted and demonstrated [16]. Specifically, $(\mathrm{Pb_{0.87}Sr_{0.05}Ba_{0.05}La_{0.02}})(\mathrm{Zr_{0.52}Sn_{0.40}Ti_{0.08}})\mathrm{O_3}$ (Modified-PZO or M-PZO), was predicted to have low lattice-mismatch at the AFE/FE interface. In bulk ceramics, this yielded a dielectric energy storage efficiency exceeding 98% with an energy density of ~ 3 J $\mathrm{cm^{-3}}$. Here, thin films of this composition were grown to assess the achievable energy density and efficiency.

4.2 Experimental Procedure

A M-PZO ceramic target with 20 % excess lead oxide was prepared with calcination of mixed powders at 850°C for 4 hours and subsequent low-temperature sintering at 875°C for 2 hours. Single crystal (100) oriented $SrTiO_3$ (STO) substrates (Shinkosha Co. Ltd) were used. For the bottom electrode, a 45 nm of $SrRuO_3$ (SRO) thin film was grown on the STO from a stoichiometric ceramic SRO target (Kojundo Co, Ltd) by Pulsed Laser Deposition (PLD). Deposition was done utilizing a 5 Hz, 1.5 J cm^{-2} energy density, 248 nm KrF excimer laser (102F, Coherent). The chamber oxygen pressure was 120 mTorr, the substrate temperature was 665°C, and 6.7 cm working distance were used. An ~ 280 nm thick M-PZO thin film was grown on the SRO bottom electrode without breaking vacuum using a laser energy density of 1.5 J cm^{-2}, 6 Hz, an oxygen pressure of 85 mTorr, a substrate temperature of 595℃, and a working distance of 6.2 cm.

A capacitor structure was fabricated by conventional double layer photolithography and lift off processing. A 100 nm thick Pt top electrode was sputter-deposited at room temperature on the surface of the M-PZO thin film (CMS-18 Sputter system, K. J. Lesker, Pittsburgh, PA) followed by rapid thermal annealing at 450℃ for 10 min to promote adhesion between the top Pt and the M-PZO layer.

4.3 Results and Discussion

Figure 4.1(a) shows the X-ray diffraction patterns near the {200} perovskite peak; a wider angle range is provided in the Supplemental Materials, Figure 4.S1(a). The films are single phase perovskite. The SRO layer shows good interface quality, as evidenced by thickness fringes. The M-PZO out-of-lattice parameter was determined to be 4.110 ± 0.001 Å, similar to that of its bulk counterpart (~ 4.109 Å) Figure 4.S1(b) shows a phi scan around [101]; a cube-on-cube epitaxial relationship between the M-PZO thin film and the substrate is apparent. Due to the ~ 280 nm thickness (see Figure 4.S2) and ~5 % lattice

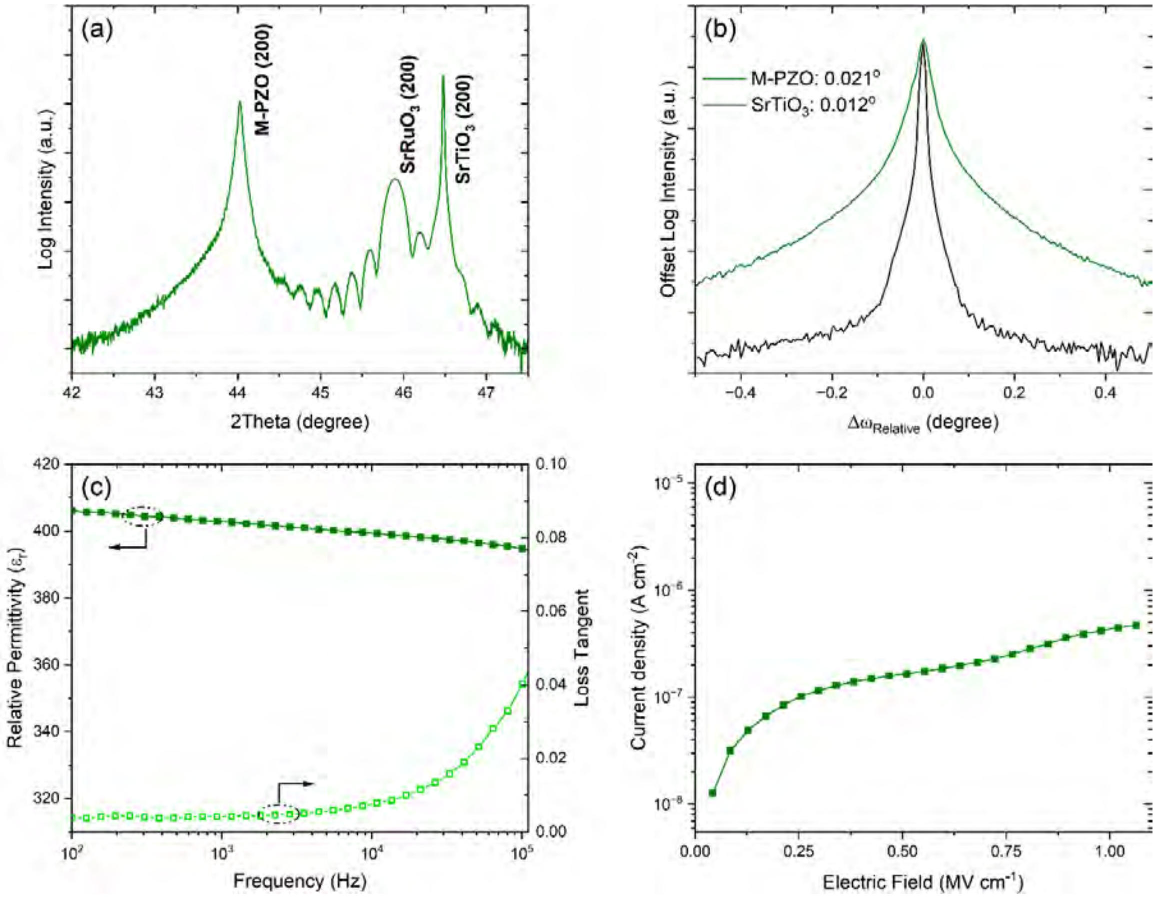

Figure 4.1. (a) X-ray diffraction of M-PZO thin film on (100) SRO/STO, (b) rocking curve of M-PZO thin film, (c) dielectric permittivity and loss tangent at room temperature, and (d) current density measured at room temperature

mismatch, the M-PZO thin film is not fully coherently strained to the underlying substrate. Figure 4.1(b) shows the rocking curve of the M-PZO. The full-width-at-half-maximum (FWHM) of the M-PZO was 0.021°, which is comparable to that of the STO single crystal substrate (0.012°), showing excellent crystalline quality.

Figure 4.1(c) shows the room temperature relative dielectric permittivity of the M-PZO thin film. A relative dielectric permittivity of approximately 405 with a loss tangent < 0.04 from 100 Hz to 100 kHz was observed at an oscillating voltage of 30 mV. This permittivity is comparable to other PZO-derived compositions reported previously [17–

19]. To estimate the leakage current densities, a DC voltage (positive) was driven from the SRO bottom electrode. A wait time of 60 seconds after changing the voltage was employed. The current density was maintained below 10^{-6} A cm^{-2} up to 1.0 MV cm^{-1}.

The polarization-electric field hysteresis loops (P-E loops) of M-PZO thin film were measured using either a bipolar or unipolar triangular waveform; in both cases, the voltage was applied to the SRO bottom electrode and sensing was done from the top electrode. At an electric field of < 0.8 MV cm^{-1} based on bipolar triangular waveform, clear antiferroelectric-like P-E loops were captured, similar to that of the bulk counterpart, as shown in Figure 4.S3 [16]. Similar P-E loops can be obtained with a unipolar triangular waveform, as shown in Figure 4.2. For an applied electric field of 1.0 MV cm^{-1} (Figure 4.2(a), green), a remanent polarization (P_{rem}) of ~ 1 μC cm^{-2} and a maximum polarization (P_{max}) of ~ 48 μC cm^{-2} were measured with a slim P-E loop. Presumably, the large electric field stabilizes a ferroelectric phase with low hysteresis loss, originating from the compatible AFE-FE interface in the system [16,20,21]. Figure 4.2(b) shows P-E loops

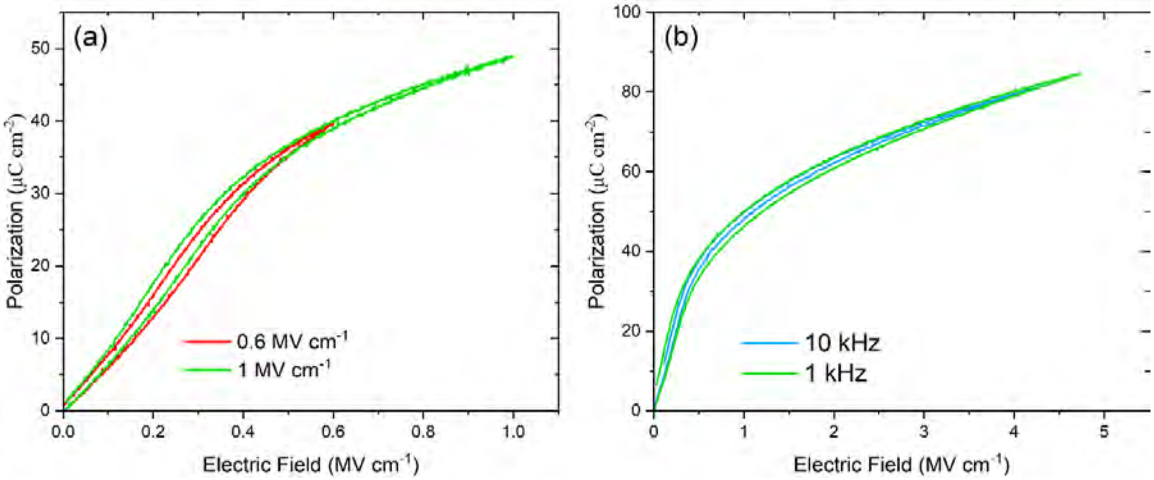

Figure 4.2. (a) Unipolar polarization-electric field hysteresis loop of M-PZO at 1 kHz at electric fields of 0.6 MV cm^{-1} (red) and 1.0 MV cm^{-1} (green). (b) Polarization-electric field hysteresis loops of M-PZO at 1 kHz (green) and 10 kHz (blue) at 4.75 MV cm^{-1} and 4.25 MV cm^{-1}, respectively.

measured at 1 kHz (green) and 10 kHz (blue), up to near their breakdown fields, 4.75 MV cm^{-1} and 4.25 MV cm^{-1} for 1 kHz and 10 kHz, respectively. In both cases, slim P-E loops were maintained until breakdown (Figure 4.S4). A higher frequency (10 kHz) leads to smaller hysteresis loss. The finite P$_{rem}$ could be due to the stabilization of the FE phase induced by kinetic bombardment during deposition or due to the time scale of the measurement [21,22]. It is also notable that the polarization saturation is slow even up to fields of several MVcm^{-1}. (Figure 4.S5)

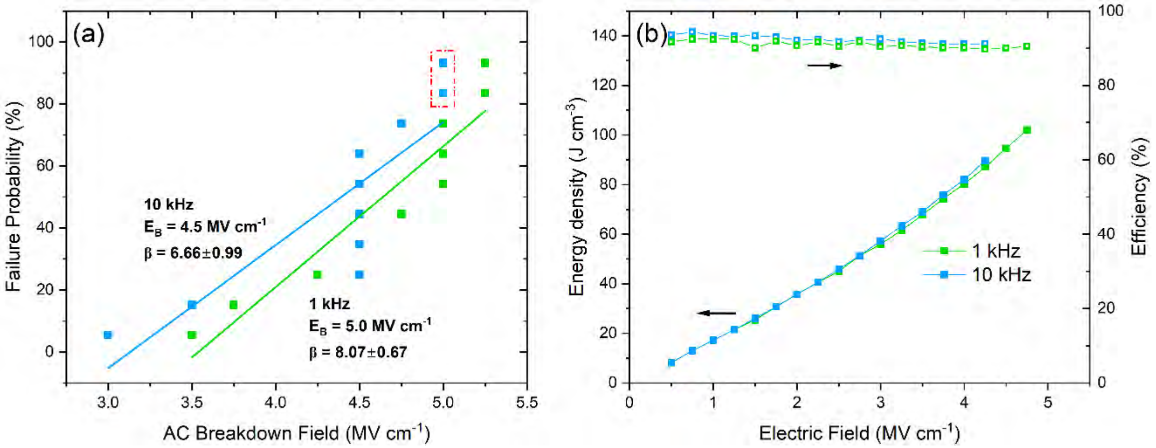

Figure 4.3. (a) Two-parameter Weibull distribution of M-PZO thin film at 1 kHz (green) and 10 kHz (blue). (b) Energy storage density extracted from unipolar P-E hysteresis loops and efficiency at 1 kHz (green) and 10 kHz (blue).

To estimate the breakdown field strength of the M-PZO thin films, a two-parameter Weibull distribution model was used. An increasing AC field unipolar waveform was applied in 0.25 MV cm^{-1} steps at either 1 kHz (green) and 10 kHz (blue), respectively, to an array of electrodes. 10 electrodes with a diameter of 25 µm were used for each frequency. The average maximum recoverable energy storage density was obtained from the average of the 10 electrodes with errors determined by standard deviation. The breakdown field was determined as the field at which the capacitor was shortened. AC breakdown fields of 5.0 MV cm^{-1} for 1 kHz and 4.5 MV cm^{-1} for 10 kHz were found, with a Weibull modulus β of 8.07±0.67 and 6.66±0.99, respectively, as shown in Figure 4.3(a). The smaller breakdown strength at higher frequency is an artifact associated with instrumentation limitations. The data points highlighted by the red box in Figure 4.3(a) indicate where this error can clearly be observed, as shown in Figure 4.S6. To avoid overestimation of the energy storage density and its efficiency, these data were excluded. In the same way, the breakdown strength estimation at 10 kHz was only reliable for fields < 4.75 MV cm^{-1}.

All recoverable energy storage densities and efficiencies were determined from unipolar P-E loops. In Figure 4.3(b), representative maximum energy density and efficiency at two different frequencies are represented. The maximum recoverable energy density was 102 J cm^{-3} with an efficiency of 90 % at 1 kHz and 90 J cm^{-3} with an efficiency of 92 % at 10 kHz, respectively. The average maximum recoverable energy storage density was 88±17 J cm^{-3} at 4.75 MV cm^{-1} with an efficiency of 85±6 % at 1 kHz. An even higher

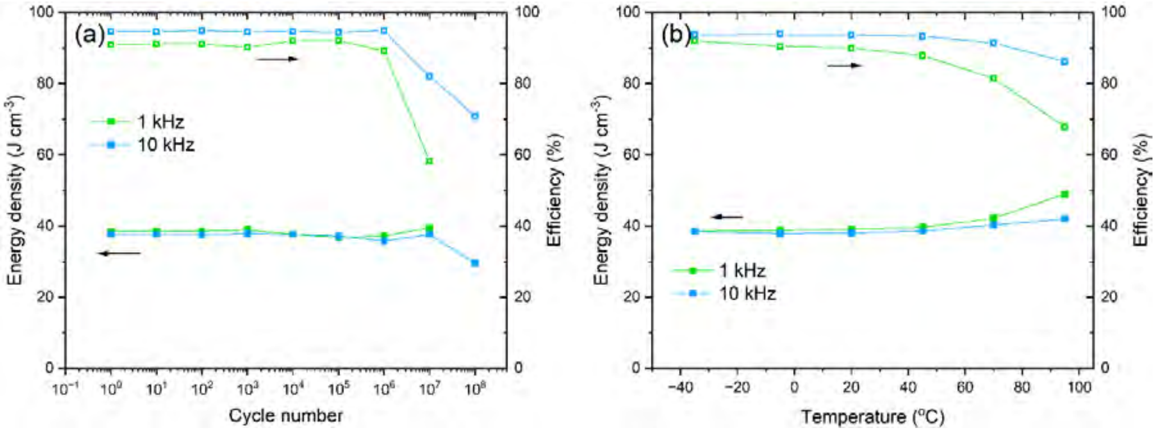

Figure 4.4. Energy storage performance of the M-PZO thin film capacitor against (a) cycle number at room temperature up to 10^8 cycles and (b) temperature from -40°C to 100°C

efficiency of 91±4 % can be realized at 10 kHz with a slightly lower averaged recoverable energy storage density of 80±15 J cm^{-3} at 4.25 MV cm^{-1}.

The reliability and thermal stability of M-PZO capacitors were assessed, as shown in Figure 4.4(a) and 4.4(b), respectively. To test fatigue behavior, the recoverable energy storage density and efficiency were studied by measuring the unipolar P-E loops every 10^x ($x = 1, 2, \ldots, 8$) cycles. A triangular waveform was applied at 1 kHz or 10 kHz at 2 MV cm^{-1}, which is less than half of breakdown field, to avoid catastrophic failure. It was found that efficiency was likely to degrade significantly after 10^7 cycles, despite almost no change in stored energy density. The capacitors broke down after 10^7 cycles at 1 kHz, but survived 10^8 cycles at 10 kHz.

The temperature stability of the capacitor was examined by measuring unipolar P-E loops from -40℃ to 100℃ at an applied field of 2 MV cm^{-1}. The capacitor's efficiency deteriorated with increasing temperature, particularly at 1 kHz. This degradation is consistent with the increasing space charge contributions evident at higher temperatures in the dielectric properties, as shown in Figure 4.S6. It is speculated that the space charge was a consequence of lead deficiency in the film, with the associated introduction of hole carriers. Such a lead deficiency could result from kinetic bombardment during deposition leading to resputtering of PbO [23]. Despite the space charge contribution, the efficiency of the M-PZO thin film is higher than many other PZO-derived thin film capacitors. Data in Figure 4.5 were taken from references [18,20,24–36].

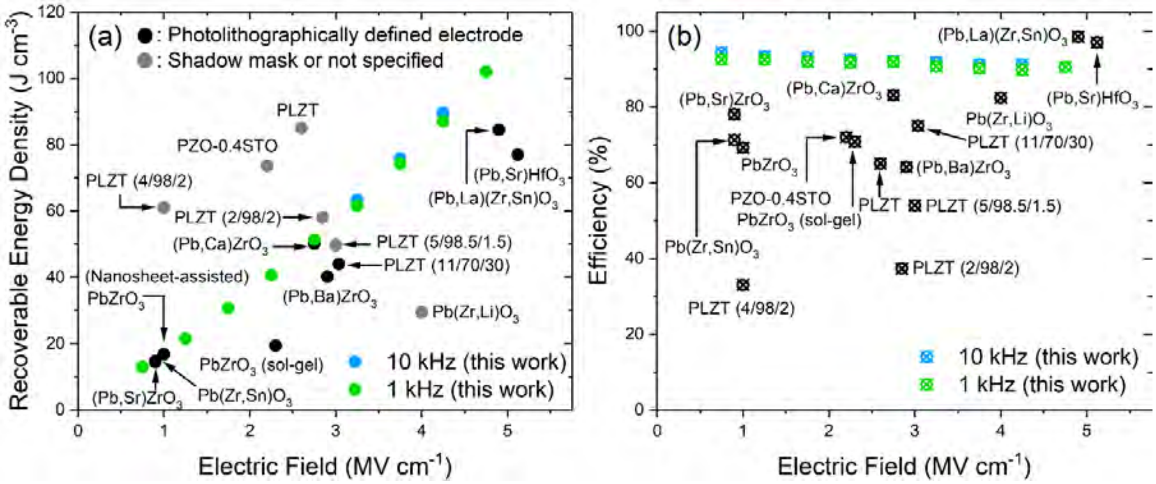

Figure 4.5. Comparison of the M-PZO thin film with other PZO-derived thin film capacitors. (a) Recoverable energy density and (b) efficiency as a function of applied electric field. Note that the highest maximum recoverable energy density and efficiency for the M-PZO films were used for this figure.

4.4 Conclusions

In summary, high crystallinity M-PZO films were prepared by PLD. A current density < 10^{-6} A cm^{-2} was obtained for an applied field of 1.0 MV cm^{-1}. Slim hysteresis P-E loops were observed with breakdown strengths of 5.0 MV cm^{-1} cm and 4.5 MV cm^{-1} at 1 kHz and 10 kHz, respectively. The average recoverable energy storage density and efficiency were 88±17 J cm^{-3} with 85±6 % at 1 kHz, and 80±15 J cm^{-3} with 92±4 % at 10 kHz, respectively. Good cyclability of the capacitor was maintained up to 10^6 cycles at 2 MV cm^{-1} applied field. Relatively poor thermal stability was caused by significant space charge contributions at high temperatures. Nonetheless, the M-PZO films showed greater efficiency than other PZO-based thin film capacitors to date.

4.5 References

[1] M. Aneke, and M. Wang, "Energy Storage Technologies and Real Life Applications – A State of the Art Review," Appl. Energy., 179 (2016), pp. 350–377

[2] M.M. Rahman, A.O. Oni, E. Gemechu, and A. Kumar, "Assessment of Energy Storage Technologies: A Review," Energy Convers. Manag., 223 (2020), Article 113295

[3] V. Etacheri, R. Marom, R. Elazari, G. Salitra, and D. Aurbach, "Challenges in the Development of Advanced Li-Ion Batteries: A Review," Energy. Environ. Sci., 4 (2011), pp. 3243–3262

[4] M.J. Pan, and C. Randall, "A Brief Introduction to Ceramic Capacitors," IEEE Electr. Insul. Mag., 26 (2010), pp. 44–50

[5] I. Husain, B. Ozpineci, M.S. Islam, E. Gurpinar, G.J. Su, W. Yu, S. Chowdhury, L. Xue, D. Rahman, and R. Sahu, "Electric Drive Technology Trends, Challenges, and Opportunities for Future Electric Vehicles," Proc. IEEE., 109 (2021), pp. 1039–1059

[6] H. Palneedi, M. Peddigari, G.T. Hwang, D.Y. Jeong, and J. Ryu, "High-Performance Dielectric Ceramic Films for Energy Storage Capacitors: Progress and Outlook," Adv. Funct. Mater., 28 (2018), Article 1803665

[7] G. Wang, Z. Lu, Y. Li, L. Li, H. Ji, A. Feteira, D. Zhou, D. Wang, S. Zhang, and I.M. Reaney, "Electroceramics for High-Energy Density Capacitors: Current Status and Future Perspectives," Chem. Rev., 121 (2021), pp. 6124–6172

[8] H. Pan, J. Ma, J. Ma, Q. Zhang, X. Liu, B. Guan, L. Gu, X. Zhang, Y.-J. Zhang, L. Li, Y. Shen, Y. H. Lin, and C. W. Nan, "Giant Energy Density and High Efficiency Achieved in Bismuth Ferrite-Based Film Capacitors via Domain Engineering," Nat. Com., 9 (2018), Article 1813

[9] X. Xu, A. S. Gurav, P. M. Lessner, and C. A. Randall, “Robust BME Class-I MLCCs for Harsh-Environment Applications,” IEEE Trans. Ind. Electron., 58 (2011), pp. 2636-2643

[10] Q. Li, J. Chen, L. Fan, X. Kong, and Y. Lu, “Progress in Electrolytes for Rechargeable Li-Based Batteries and Beyond,” Green Energy Environ., 1 (2016), pp. 18-42

[11] M.K. Aslam, Y. Niu, T. Hussain, H. Tabassum, W. Tang, M. Xu, and R. Ahuja, “How to Avoid Dendrite Formation in Metal Batteries: Innovative Strategies for Dendrite Suppression,” Nano Energy, 86 (2021), Article 106142

[12] H. Luo, X. Zhou, C. Ellingford, Y. Zhang, S. Chen, K. Zhou, D. Zhang, C.R. Bowen, and C. Wan, “Interface Design for High Energy Density Polymer Nanocomposites,” Chem. Soc. Rev., 48 (2019), pp. 4424–4465

[13] B. Xu, J. Íñiguez, and L. Bellaiche, “Designing Lead-Free Antiferroelectrics for Energy Storage,” Nat. Com., 8 (2017), pp. 1–8

[14] Z. Liu, T. Lu, J. M. Ye, G. S. Wang, X. L. Dong, R. Withers, and Y. Liu, “Antiferroelectrics for Energy Storage Applications: A Review,” Adv. Mater. Technol., 3 (2018), Article 1800111

[15] B. Liu, X. Tian, L. Zhou, and X. Tan, “Motion of Phase Boundary during Antiferroelectric-Ferroelectric Transition in a $PbZrO_3$-Based Ceramic,” Phys. Rev. Mater., 4 (2020), Article 104417

[16] A.P.S. Gaur, R. Choudhary, B. Liu, Y. Mudryk, D. D. Johnson, J. Cui, and X. Tan, “Antiferroelectric Ceramics for Energy-Efficient Capacitors by Theory-Guided Discovery,” Adv. Mater., 36 (2024), Article 2312856

[17] S.K. Thatikonda, W. Huang, X. Du, C. Yao, Y. Ke, J. Wu, N. Qin, and D. Bao, “Sm-Doping Induced Large Enhancement of Antiferroelectric and Energy Storage Performances of (111) Oriented $PbZrO_3$ Thin Films,” Ceram. Int., 45 (2019), pp. 23586–23591

[18] T. Zhang, Y. Si, S. Deng, H. Wang, T. Wang, J. Shao, Y. Li, X. Li, Q. Chen, C. Liu, G. Zhong, Y. Huang, J. Wei, L. Chen, S. Das, and Z. Chen, “Superior Energy Storage Performance in Antiferroelectric Epitaxial Thin Films via Structural Heterogeneity and Orientation Control,” Adv. Funct. Mater., 34 (2024), Article 2311160

[19] Y.Z. Li, Z.J. Wang, Y. Bai, W. Liu, and Z.D. Zhang, “Enhancement of Energy Storage Density in Antiferroelectric $PbZrO_3$ Films via the Incorporation of Gold Nanoparticles,” J. Am. Ceram. Soc., 102 (2019), pp. 5253–5261

[20] Z. Hu, B. Ma, R.E. Koritala, and U. Balachandran, “Temperature-Dependent Energy Storage Properties of Antiferroelectric $Pb_{0.96}La_{0.04}Zr_{0.98}Ti_{0.02}O_3$ Thin Films,” Appl. Phys. Lett., 104 (2014), Article 263902

[21] L. Pintilie, K. Boldyreva, M. Alexe, and D. Hesse, “Coexistence of Ferroelectricity and Antiferroelectricity in Epitaxial $PbZrO_3$ Films with Different Orientations,” J. Appl. Phys., 103 (2008), Article 48

[22] H. Pan, Z. Tian, M. Acharya, X. Huang, P. Kavle, H. Zhang, L. Wu, D. Chen, J. Carroll, R. Scales, C.J.G. Meyers, K. Coleman, B. Hanrahan, J.E. Spanier, and L.W. Martin, “Defect-Induced, Ferroelectric-Like Switching and Adjustable Dielectric Tunability in Antiferroelectrics,” Adv. Mater., 35 (2023), Article 2300257

[23] S.K. Hau, K.H. Wong, P.W. Chan, C.L. Choy, “Intrinsic Resputtering in Pulsed-Laser Deposition of Lead-Zriconate-Titanate Thin Films.”, Apply. Phys. Lett., 66 (1995), pp. 245-247

[24] M. Acharya, E. Banyas, M. Ramesh, Y. Jiang, A. Fernandez, A. Dasgupta, H. Ling, B. Hanrahan, K. Persson, J.B. Neaton, and L.W. Martin, “Exploring the $Pb_{1-x}Sr_xHfO_3$ System and Potential for High Capacitive Energy Storage Density and Efficiency,” Adv. Mater., 34 (2022), Article 2105967

[25] Y Y.Z. Li, Z.J. Wang, Y. Bai, and Z.D. Zhang, “High Energy Storage Performance in Ca-Doped $PbZrO_3$ Antiferroelectric Films,” J. Eur. Ceram. Soc., 40 (2020), pp. 1285–1292

[26] X. Hao, J. Zhai, and X. Yao, “Improved Energy Storage Performance and Fatigue Endurance of Sr-Doped $PbZrO_3$ Antiferroelectric Thin Films,” J. Am. Ceram. Soc., 92 (2009), pp. 1133–1135

[27] B. Shen, F. Huang, L. Lei, Z. Wu, X. Hu, Z. Xu, L. Liu, Y. Ye, and X. Lu, “Large Recoverable Energy Storage Density and Efficiency in $PbZrO_3$-x$SrTiO_3$ Thin Films with Polymorphic Nanodomains,” Appl. Phys. Lett., 123 (2023), Article 72905

[28] M.D. Nguyen, T.T. Trinh, H.T. Dang, and H.N. Vu, “Understanding the Effects of Electric-Field-Induced Phase Transition and Polarization Loop Behavior on the Energy Storage Performance of Antiferroelectric $PbZrO_3$ Thin Films,” Thin Solid Films, 697 (2020), Article 137794

[29] M.D. Nguyen, and G. Rijnders, “Electric Field-induced Phase Transition and Energy Storage Performance of Highly-Textured $PbZrO_3$ Antiferroelectric Films with a Deposition Temperature Dependence,” J. Eur. Ceram. Soc., 38 (2018), pp. 4953–4961

[30] Q. Chen, Y. Zhang, J. Zhang, H. Shen, R. Qi, X. Chen, Z. Fu, G. Wang, J. Yang, W. Bai, X. Tang, “Effects of Ti-doping on Energy Storage Properties and Cycling Stability of $Pb_{0.925}La_{0.05}ZrO_3$ Antiferroelectric Thin Films,” Mater. Sci. Eng. B., 286 (2022), Article 116024

[31] B. Ma, Z. Hu, R.E. Koritala, T.H. Lee, S.E. Dorris, and U. Balachandran, “PLZT Film Capacitors for Power Electronics and Energy Storage Applications,” J. Mater. Sci. Mater. Electron., 26 (2015), pp. 9279–9287

[32] B. Peng, Q. Zhang, X. Li, T. Sun, H. Fan, S. Ke, M. Ye, Y. Wang, W. Lu, H. Niu, X. Zeng, and H. Huang, “Large Energy Storage Density and High Thermal Stability in a Highly Textured (111)-Oriented $Pb_{0.8}Ba_{0.2}ZrO_3$ Relaxor Thin Film with the Coexistence of Antiferroelectric and Ferroelectric Phases,” ACS Appl. Mater. Interfaces., 7 (2015), pp. 13512–13517

[33] Y. Wang, X. Hao, J. Yang, J. Xu, and D. Zhao, “Fabrication and Energy-Storage Performance of $(Pb,La)(Zr,Ti)O_3$ Antiferroelectric Thick Films Derived from Polyvinylpyrrolidone-Modified Chemical Solution,” J. Appl. Phys., 112 (2012), Article 34105

[34] X. Guo, J. Ge, F. Ponchel, D. Rémiens, Y. Chen, X. Dong, and G. Wang, “Effect of Sn Substitution on the Energy Storage Properties of High (001)-Oriented $PbZrO_3$ Thin Films,” Thin Solid Films, 632 (2017), pp. 93–96

[35] C. Zhang, X. Zhang, B. Zhang, C. Yin, Y. Zhang, Y. Zhang, T. Zhang, Y. Cui, and Q. Chi, “High-Energy Storage Performance Achieved in $PbZrO_3$ Thin Films via Li+ Doping and Low-Temperature Annealing,” Thin Solid Films, 794 (2024), Article 140289

[36] A. Kumar, S.H. Kim, A. Thakre, G. Lee, Y.G. Chae, and J. Ryu, “Increased Energy-Storage Density and Superior Electric Field and Thermally Stable Energy Efficiency of Aerosol-Deposited Relaxor $(Pb_{0.89}La_{0.11})(Zr_{0.70}Ti_{0.30})O_3$ Films,” J. Therm. Spray Technol., 30 (2021), pp. 591–602

4.6 Supplementary Materials for Chapter 4

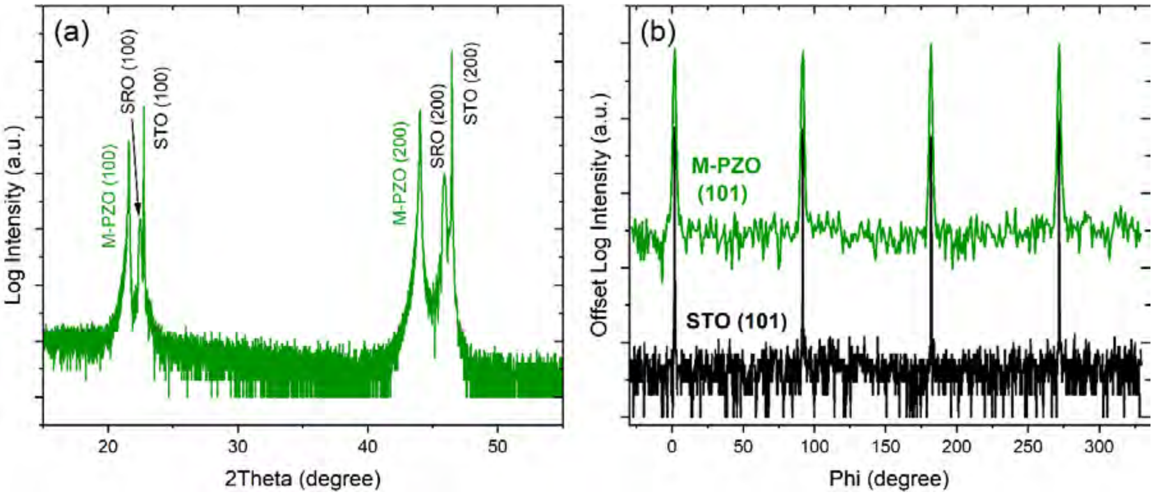

Figure 4.S1. X-ray diffraction pattern of M-PZO thin film deposited on (100) SRO/STO and (b) phi scan around [101] to show the in-plane relationship between the M-PZO and STO substrates.

Figure 4.S1(a) shows the X-ray diffraction (XRD) pattern of a $(Pb_{0.87}Sr_{0.05}Ba_{0.05}La_{0.02})(Zr_{0.52}Sn_{0.40}Ti_{0.08})O_3$ (M-PZO) thin film deposited on a $SrRuO_3/SrTiO_3$ substrate. The film shows a single perovskite phase with no detectable secondary phases. A cube-on-cube epitaxial relationship between M-PZO and STO can be observed from the phi scan, as shown in Figure 4.S1(b).

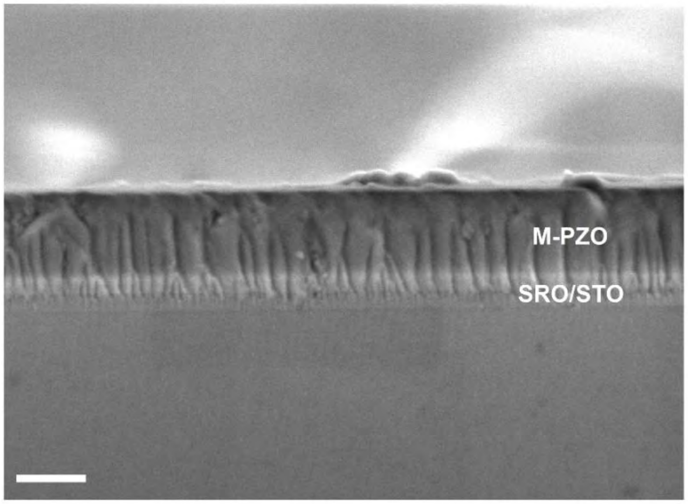

Figure 4.S2. A Field Emission Secondary Electron Microscope cross-section of an M-PZO film on SRO/STO. The scale bar (bottom left) corresponds to 200 nm.

A cross-section view of M-PZO thin film is shown in Figure 4.S2. A dense columnar microstructure is observed with a thickness of approximately 280 nm under the given processing conditions.

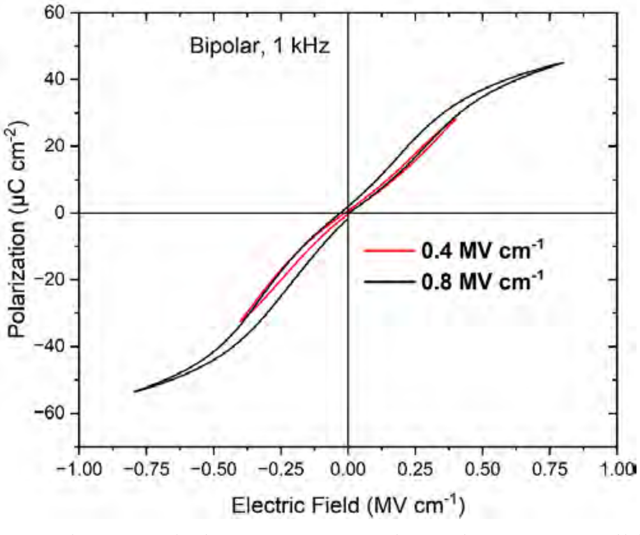

Figure 4.S3. Bipolar P-E hysteresis loops measured at 1 kHz at two different electric fields

In Figure 4.S3, bipolar P-E hysteresis loops of the M-PZO films measured at 1 kHz are shown. Antiferroelectric-like P-E loops are observed with slightly larger hysteresis loss at an electric field of 0.8 MV cm^{-1} (black), compared to that measured at an electric field of 0.4 MV cm^{-1} (red).

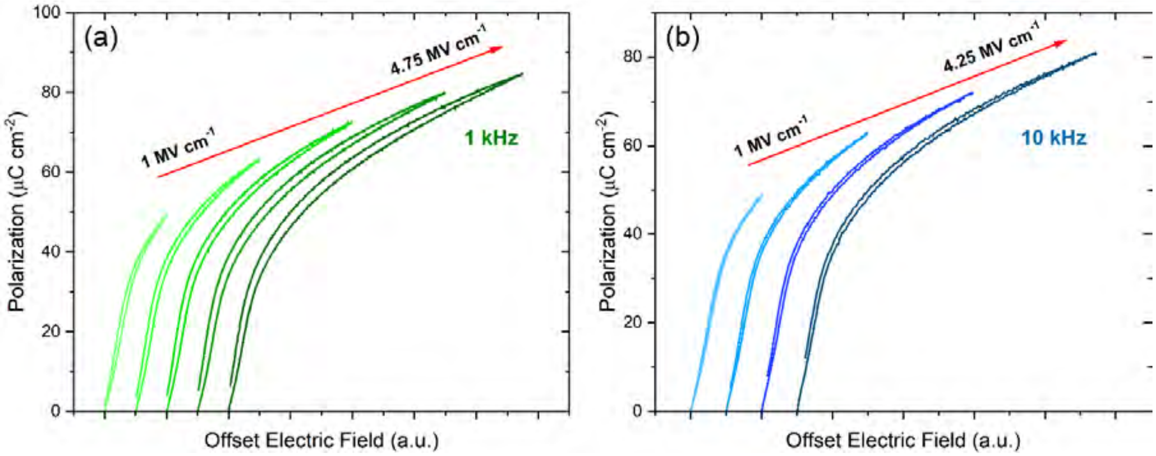

Figure 4.S4. Unipolar P-E hysteresis loops at (a) 1 kHz and (b) 10 kHz, with the field increased until dielectric breakdown. Note that the x-axis is an offset electric field, so that the hysteresis is more readily detectable.

A triangular waveform was applied at measurement frequencies of 1 kHz and 10 kHz. Notably, M-PZO films do not exhibit significant hysteresis loss until dielectric breakdown.

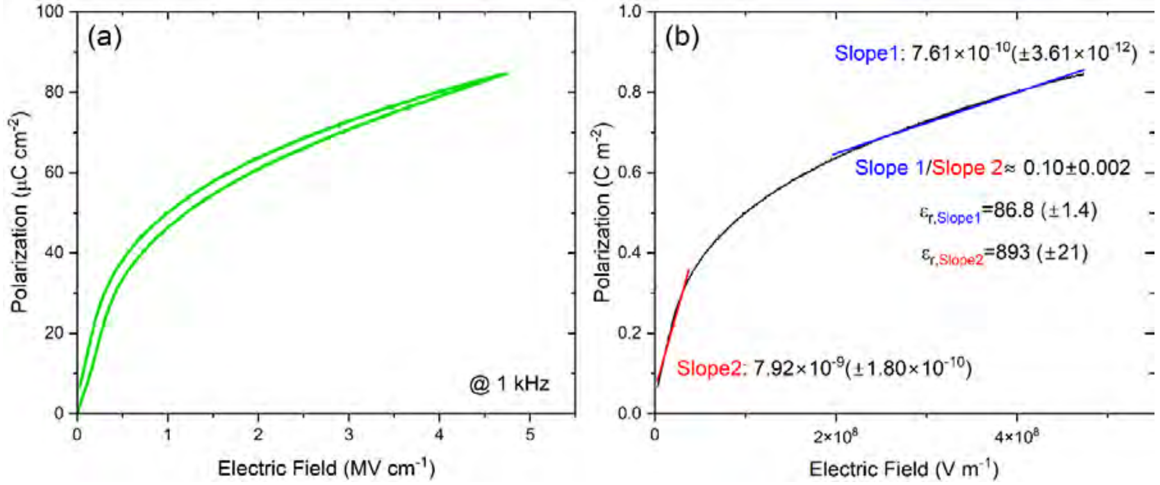

Figure 4.S5. (a) Unipolar P-E hysteresis loop at 1 kHz for an applied field of 4.75 MV cm^{-1}. (b) Unipolar P-E hysteresis response upon decreasing electric field.

Figure 4.S5(b) shows the dielectric susceptibility (χ) calculated from the P-E loop. The black line corresponds to data points obtained upon decreasing electric field from 4.75 MV cm^{-1}. Slope 1 (blue) and slope 2 (red) were extracted by linear fitting of the data points. The susceptibility was estimated from the equation of $\chi = (\varepsilon_r - 1)$ where ε_r is the relative permittivity. The decrease in slope above 1 MV cm^{-1} is attributed to completion of the FE-AFE transition. Importantly, the saturation of polarization in M-PZO is slow and delayed up to the electrical breakdown field.

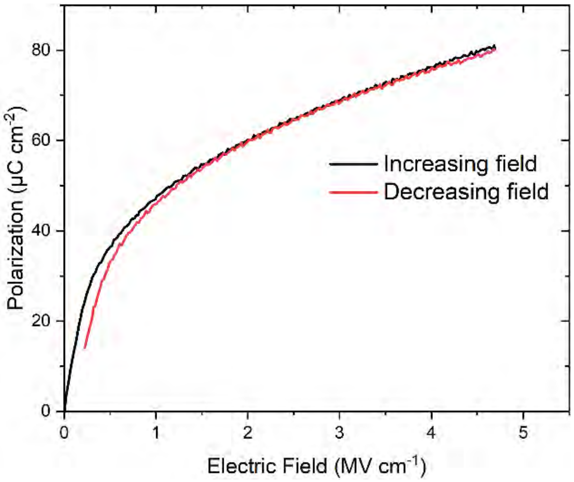

Figure 4.S6. P-E loop of M-PZO at 10 kHz for an applied field of 4.75 MV cm^{-1}. Note the unphysical polarization response upon decreasing field (red).

Figure 4.S6 shows the P-E loop of M-PZO at 10 kHz. The black line corresponds to data points acquired on increasing electric field and the red line corresponds to the decreasing electric field. It is unphysical that the decreasing field signal shows a smaller polarization than the increasing field data. Due to this instrumentation limitation, the energy storage density and efficiency can be overestimated. Thus, neither energy density nor efficiency were calculated from the P-E loop showing this instrumentation error.

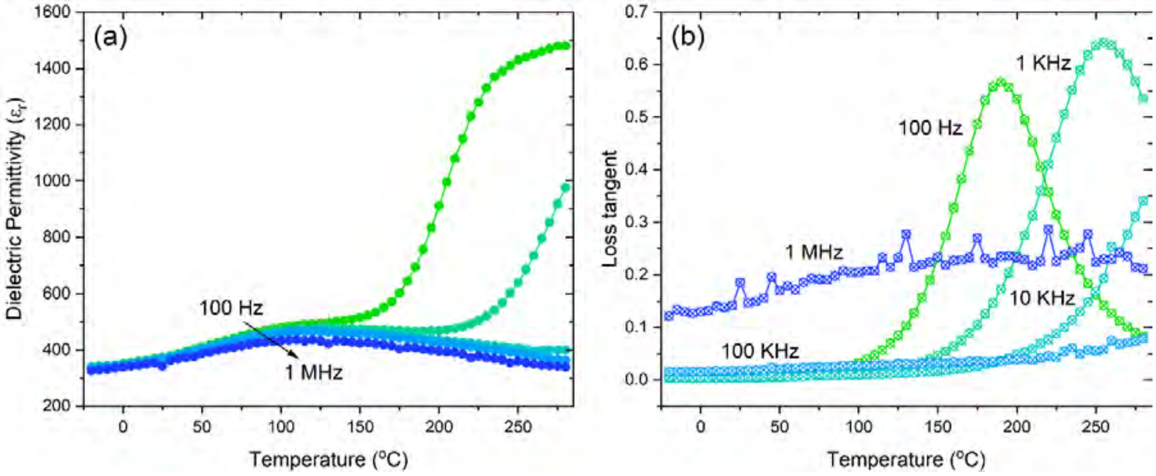

Figure 4.S7. Temperature dependent (a) relative dielectric permittivity and (b) loss tangent of the M-PZO thin film capacitor

To study the film's temperature dependent dielectric properties from -25°C to 285°C, 30 mV was driven from the SRO bottom electrode. The maxima in the loss at temperatures exceeding 150°C were attributed to the space charge contribution.

Chapter 5

Conclusions and Future Work

5.1 Conclusions

This dissertation discussed synthesizability, structural, dielectric, ferroelectric, polarization stability, electrocaloric, and energy storage properties of HEO-like formulations with the perovskite crystal structure.

In chapter 2, starting from a base compositions of perovskite PZT, two different compositions with disorder on the B-site of perovskite were examined. It was demonstrated that the columbite-like approach of pre-calcination plays a very important role in powder processing. Through cyclic heat treatment on Mn-containing powders (Mn_P), a reversible phase transformation was observed, suggesting the potential of entropy-stabilized structural evolution. Configurational entropy promotes the formation of a single-phase, but does not guarantee it. High effective temperatures from the high kinetic energy of adatoms in PLD was utilized to synthesize single-phase HEPO film that did not form a single-phase as powders.

Due to the multivalency of Mn, the Mn_P films were electrically leaky. On the other hand, Al_P films exhibited a dielectric constant of ~ 2000 with a loss tangent < 0.05 at room temperature. Slim relaxor-like hysteresis loops were observed. A P_{max} of 47.7 μC cm^{-2} and P_{rem} of 8.2 of μC cm^{-2} were achieved at ~ 1200 kV cm^{-1} and 10 kHz. Clear temperature-dependent dispersion of dielectric permittivity was observed below the T_{max} of 105°C. The electrocaloric temperature change derived from Maxwell relations for the Al_P film was 8.4 K at 180°C and 1190 kV cm^{-1}.

In chapter 3, more HEO-like formulations were explored with an aim of engineering electrocaloric effects. As expected, the perovskite tolerance factor controls the ferroelectric distortion observed; a rhombohedral distortion appeared with an average tolerance factor < 0.99, a pseudo-cubic perovskite between 0.99 and 1.01, and a tetragonal distortion with tolerance factor > 1.01. The Fe_P film revealed high leakage, presumably due to charge hopping, while Al_P and Sc_P films displayed relaxor-like and ferroelectric- like behaviors, respectively, based on the temperature-dependent dielectric properties. Indirect measurement using Maxwell-relations were utilized to calculate the ECE of Al_P and Sc_P films. Maximum values of 7.39 K at 135℃ for the Al_P film and 5.74 K at 50℃ for Sc_P film were achieved. The polarization stability was examined by PUND measurements; rapid polarization decay was apparent for Al_P films due to relaxor-like responses. A field induced phase transition for Sc_P film was observed, which could be a useful source of ECE. The activation energy for the depolarization of the Al_P film was determined to be ≈ 87 meV. An enhanced ECE temperature change of 14.9 K was observed for the Al_P film via a customized-PUND that allowed 2 s of rest between measurement pulses to promote dipole randomization.

Energy storage properties of PZO-derived thin film were discussed in chapter 4. High structural quality M-PZO thin films (FWHM of 0.021°) can be prepared by PLD with a lattice parameter of 4.110 ± 0.001 Å. The average recoverable energy storage density and efficiency were 88 ± 17 J cm^{-3} and 85 ± 6 % at 1 kHz, and 80 ± 15 J cm^{-3} and 92 ± 4 % at 10 kHz, respectively. The capacitor exhibited good cyclability up to 10^6 cycles at 2 MV cm^{-1}

applied field. This study demonstrated fabrication and energy storage performance of a ceramic thin film capacitor with high efficiency.

5.2 Future Work

5.2.1 Solubility Limit of High Entropy Perovskite Oxides

It is widely recognized that interesting properties and phenomena can be manifested near phase boundaries, as is demonstrated for the $Pb(Zr_{1-x}Ti_x)O_3$ (PZT), (1-x)$Pb(Mg_{1/3}Nb_{2/3})O_3$ - x$PbTiO_3$ (PMN-PT), and (1-x)$Pb(Zn_{1/3}Nb_{2/3})O_3$-x$PbTiO_3$ (PZN-PT) solid solutions, for example [1–3]. In chapters 2 and 3, it was shown that Al_P exhibits relaxor ferroelectricity. In order to establish deeper understanding on how the phase of the HEO-like formulations evolves and to exploit their properties, it is essential to investigate the solubility limit for Al in this system. For this purpose, two different new Al_P formulations should be prepared: an Al-rich composition of $Pb(Hf_{0.1}Zr_{0.1}Ti_{0.1}Nb_{0.35}Al_{0.35})O_3$ (Al-rich) and an Al-deficient composition of $Pb(Hf_{0.25}Zr_{0.25}Ti_{0.25}Nb_{0.125}Al_{0.125})O_3$ (Al-deficient) to systematically quantify their enhancement in relaxor character and electrocaloric responses.

Furthermore, in Al_P, $Pb(Nb,Al)_{1/2}O_3$ (PNA) is speculated to be responsible for the relaxor ferroelectricity. To explore the processability and phase development, $Pb(Hf,Zr,Ti)_{1/3}O_3$ and PNA powders can be separately prepared. Some preliminary experimental data will be discussed below based on the powder processing.

For the processing of the powders, a columbite-like approach was employed to bypass pyrochlore phase and maximize perovskite. B-site precursors with compositions of $(Hf_{1/3}Zr_{1/3}Ti_{1/3})O_2$ and $(Al_{1/2}Nb_{1/2})O_2$ for PHZT and PNA, respectively, were ball milled

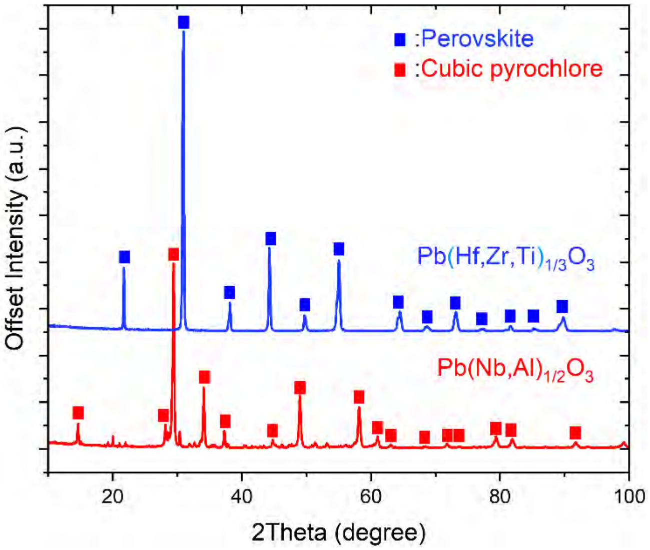

Figure 5.1. Powder XRD of PHZT (blue) and PNA (red).

with ethanol for 24 hours. After drying at 80°C, the B-site precursor powders were calcined at 1300°C for 4 hours. Then, lead oxide power was added and ball milled again with ethanol for 24 hours, followed by drying at 80°C. The same approach can be applied for the Al-rich and Al-deficient compositions.

Figure 5.1(a) shows XRD scans of PHZT and PNA powders calcined at 850°C and 900°C for 4 hours, respectively. It should be noted that PHZT powder formed single perovskite phase at 850°C. In contrast, PNA powder was unlikely to stabilize in the perovskite structure even at higher temperature (up to 1100°C), but preferentially formed a pyrochlore phase. Presumably, successful transformation of pyrochlore phase of PNA into the perovskite phase was not feasible due to sluggish kinetics at the given processing conditions [4,5]. To overcome the sluggish kinetics, higher temperature calcination with excess $PbZrO_3$ (PZO) powder (or excess PNA powder) source can be considered. The excess PZO or PNA powder source should compensate for Pb volatility at relatively higher temperatures. Table 5.1 shows the specific mole fractions of Al-based HEPO compositions for this study.

Table 5.1. Al-based HEPO compositions with different mole fractions

	Pb	Hf	Zr	Ti	Nb	Al	O
Al-rich	1	0.1	0.1	0.1	0.35	0.35	3
Al-equal	1	0.2	0.2	0.2	0.2	0.2	3
Al-def.	1	0.25	0.25	0.25	0.125	0.125	3

In designing high entropy-based electrocaloric materials (or relaxor materials), it is important to consider several contributing factors. Investigations on the Mn_P and Fe_P suggest that it is beneficial to avoid the use of multivalent element, as they give rise to significant leakage by charge hopping. Another consideration that should be factored in is thermal conductivity. For instance, J14 (the first ESO) or its derivative compositions exhibit low thermal conductivities of less than 3 W m^{-1} K^{-1} due to photon scattering [6]. Even lower conductivities of 0.7 W m^{-1} K^{-1} can be realized in high entropy perovskite compounds [7]. Thus, it is expected that fabricated electrocaloric material will possess low thermal conductivity. A low thermal conductivity for the electrocaloric material will increase the response time for heat release/absorption to or from the heat sink/source. Furthermore, in direct measurement of ECE in thin film, thermal conductivity could greatly influence on the boundary conditions, despite the diminished contributions at frequency higher than 3×10^5 Hz [8].

5.2.5. Structural Origin of Relaxor Ferroelectricity in High Entropy Perovskite Oxides

Relaxor ferroelectrics, such as $Pb(Mg_{1/3}Nb_{2/3})O_3$ (PMN), are characterized by polar nano regions (PNRs). PNRs are often associated with local random fields caused by cations with different sizes and charges, such as Mg^{2+} and Nb^{5+} in PMN, on the B-site of perovskite, resulting in perturbation of long range polar order [9,10].

In PMN, two distinct B-site sublattices (β' and β'') are present [11]. Charge neutrality is maintained by mixing Nb and Mg with a ratio of 2:1 on the β' site, while only Nb populates the β'' site. The coexistence of such ordered regions with disordered regions is a structural origin of relaxor ferroelectricity in PMN [12]. The chemical ordering in PMN was recently shown to be graded, rather than fully ordered/fully disordered [13].

In $Al_{P,}$ relaxor ferroelectricity is observed in the dielectric and ferroelectric responses. To better understand the influence of the HEO formulation in the development of relaxor ferroelectricity, a study on the structural origin of relaxor ferroelectricity in HEPO is proposed. This is described in the context of some preliminary results based on transmission electron microscopy (TEM) and X-ray energy dispersive spectroscopy (XEDS).

Al$_P$ and Sc$_P$ HEPO films were used. The Sc$_P$ film exhibited normal ferroelectricity based on its dielectric and ferroelectric properties.

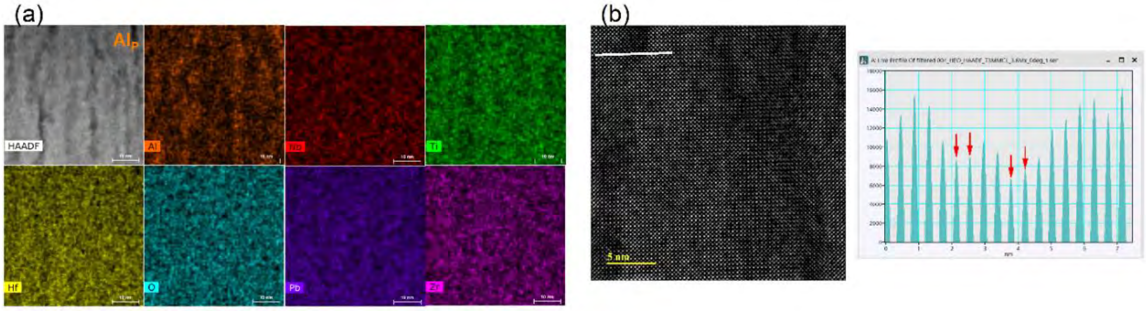

Figure 5.2. (a) High-angle annular dark-field scanning (HAADF) image and X-ray energy dispersive spectroscopy (XEDS) of Al$_P$ and (b) line scan (white line) across dark regions for intensity profile. Note that “dark” structural features are observed in the HAADF image. Al might be responsible for the features based on XEDS image, but the interpretation is ambiguous due to the absence of correlation with either the Nb or Pb signals. A line scan across a dark region shows a consistent drop in the intensity.

Figure 5.2(a) shows HAADF image with corresponding XEDS map of all elements in Al$_P$ film. Patchy dark regions were observed in the HAADF image. These regions were uniformly distributed over the entire thickness of the films. These corresponded to Al-deficiency in the XEDS maps. Line scans were performed across the dark region as shown in Figure 5.2(b). However, there is not a clear visual correlation with either the Nb or Pb signals, as would be expected based on charge balance. Figure 5.3 shows HRTEM image

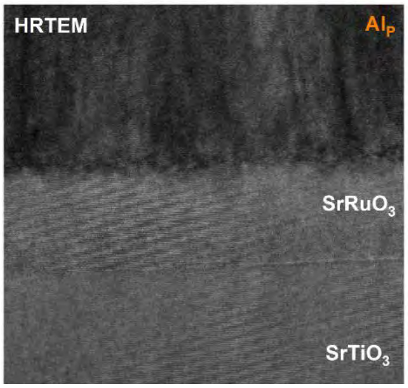

Figure 5.3. High Resolution TEM (HRTEM) image of Al$_P$

of Al_P film along the [110] zone axis. It shows the cube-on-cube epitaxial relationship between Al_P film and substrate, consistent with previous XRD results.

Electron scattering images of the Al_P film along the [100] and [110] zone axes are shown in Figure 5.4 (a) and (b), respectively. In general, the existence of short range ordering in relaxor ferroelectrics such as PMN can be investigated by observation of diffuse scattering and superlattice reflections in electron diffraction patterns. However, neither diffuse scattering correlated with Pb displacements or superlattice reflections associated with short range cation ordering were observed along either the [100] or [110] zone axis [13, 14]. This is unusual in a material that clearly shows evidence for PNR based on the electrical data and suggests that HEPO materials may demonstrate relaxor characteristics without unambiguous evidence for local chemical ordering.

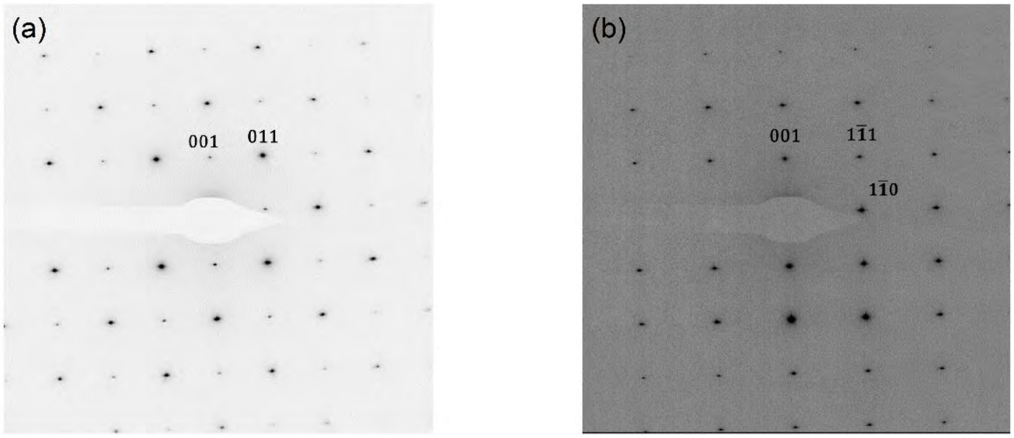

Figure 5.4. Electron scattering patterns of the Al_P film along the (a) [100] and (b) [110] zone axes. Note that absence of diffuse scattering and superlattice reflection for Al_P film.

In contrast, the Sc_P film reveals neither dark features in the HAADF image nor segregation in the EDS maps, as shown in Figure 5.4. Likewise, these films showed no evidence of superlattice spots, and electrically, they behaved more like normal ferroelectrics. More work is clearly needed to establish the presence of PNR and their correlation (if any) with local compositional ordering. In particular, working with the hypothesis that Al or $Pb(Al_{1/2}Nb_{1/2})O_3$ is responsible for the relaxor ferroelectricity, new samples with higher Al-content may be beneficial to this study.

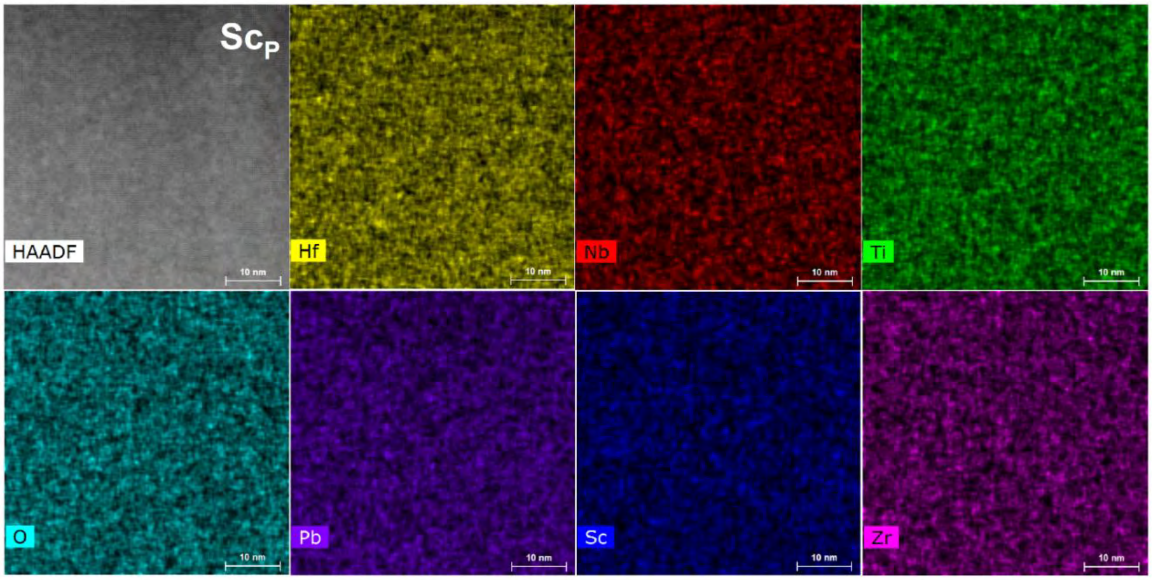

Figure 5.5. HADDAF image and XEDS map of Sc_P. Unlike Al_P, no detectable segregation or structural features are shown at the given length scale.

To further evidence of differences in the ferroelectric character of Al_P and Sc_P films, low temperature-based measurement should be undertaken. In particular, field-cooled dielectric measurement can provide another strong electrical evidence for the relaxor character (glassy nature) of Al_P films. Specifically, by measuring differences between the field-cooled and the zero-field-cooled dielectric permittivity, the freezing temperature can be estimated [15].

Furthermore, a phenomenological approach known as the Kohlrausch-Williams-Watts (KWW) function should be applied to study the polarization relaxation, as has been described elsewhere for relaxor ferroelectrics [16-18]. Polarization relaxation in the time domain (*t*) can be fitted with the following function:

$$P\ (t) \propto \exp\left[-({}^{t}\!/_{\tau})^{\beta}\right]$$

where β is the stretched exponent coefficient (0< β<1), and τ is a characteristic relaxation time. This investigation can be performed by measuring the time dependent current response of material as a voltage is removed. The two parameters can be extracted from the fitting. In general, larger the β, the narrower the distribution in time constant (less stretched) and the smaller the τ, the faster the polarization relaxation. It is anticipated that the Al_P film would have a smaller τ and potentially a smaller β compared to the Sc_P film. Of interest is whether the KWW model could be utilized not only to study the relaxation kinetics of depolarization, but also to correlate the results with the degree of relaxor character.

5.2.3 High Entropy Fluorite and Electrocaloric Effects

Over the last decade, ferroelectricity in the fluorite structure has garnered significant attention [19,20]. Since the discovery of the first entropy-stabilized oxides, many different crystal structures with high entropy formulations have been investigated, such as rocksalt, perovskite, pyrochlore, fluorite, Mxenes, etc [21-25].

Here, exploration of ferroelectricity and electrocaloric effects in high entropy fluorites (HEF) is proposed with some preliminary results on powder processing. The model system of $(Hf_{0.2}Zr_{0.2}Ce_{0.2}Ti_{0.2}Sn_{0.2})O_2$ was chosen [26]. All powders were acquired from Sigma Aldrich. HfO_2 (98%), ZrO_2 (99%), CeO_2 (99.9%), TiO_2 (99.8%), and SnO_2 (99.99%) raw powders were ball-milled for 24 hours and dried at 80°C in an oven. Pre-calcination at 1300°C for 6 hours was performed. It should be noted that the powder was likely to evaporate significantly at temperature higher than 1300°C. Two different ceramic pellets were prepared. The first pellet was prepared using a 13 mm diameter die with a uniaxial 167 MPa followed by heat treatment at 1500°C for 6 hours. The second sample was prepared using a 1 inch diameter die with a uniaxial pressure 44 MPa followed by cold isostatic CIP at 207 MPa. XRD patterns (Figure 5.5) show mostly one phase with a small secondary phase peak near ~ 30° for the first sample (black), while the second sample (blue-green) is multiphase. Figure 5.6 and Figure 5.8 displays the EDS results. Clearly, Ce segregation was observed in both samples. From the EDS map spectrum of the multi-phase sample (Table 5.2 and Figure 5.7), a near equiatomic composition was preserved. However, the nearly single-phase sample (Table 5.3 and Figure 5.9) shows significant levels of Sn and Ti deficiency. The results of XRD and EDS suggest that single-phase HEF could be promoted at the expense of Ti and Sn deficiency presumably due to evaporation during sintering. The TiO_2-SnO_2 solid solution is likely to be volatile when temperatures approach ~ 1400°C [27]. This result is different from original work for the same composition published elsewhere [26]. It can be speculated that higher pressure applied for the second sample led to a higher green density. If this is true, then evaporation of Ti and Sn could be suppressed as the surface area decreased.

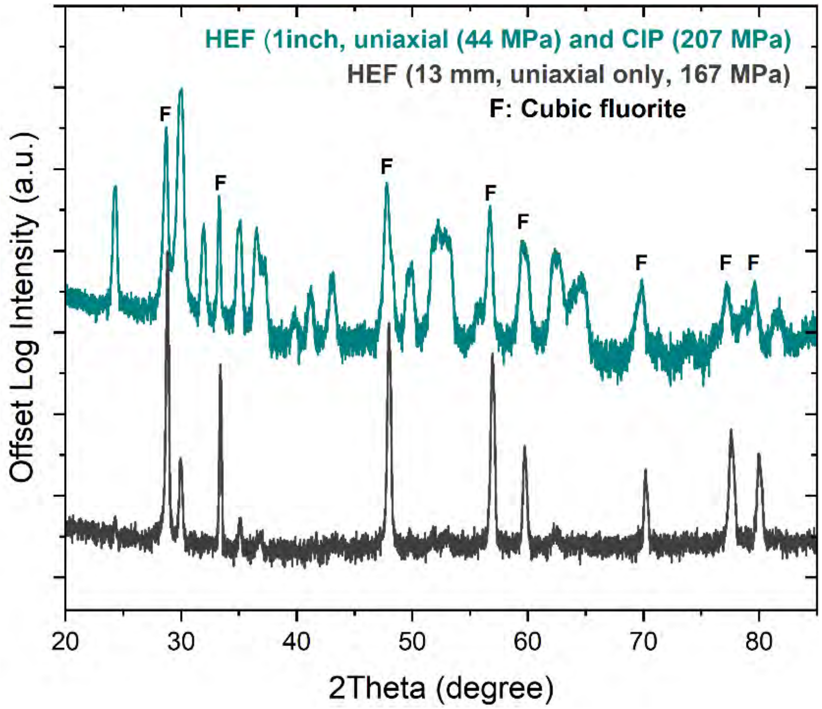

Figure 5.6. XRD of High Entropy Fluorite (HEF) powders processed using two different procedures.

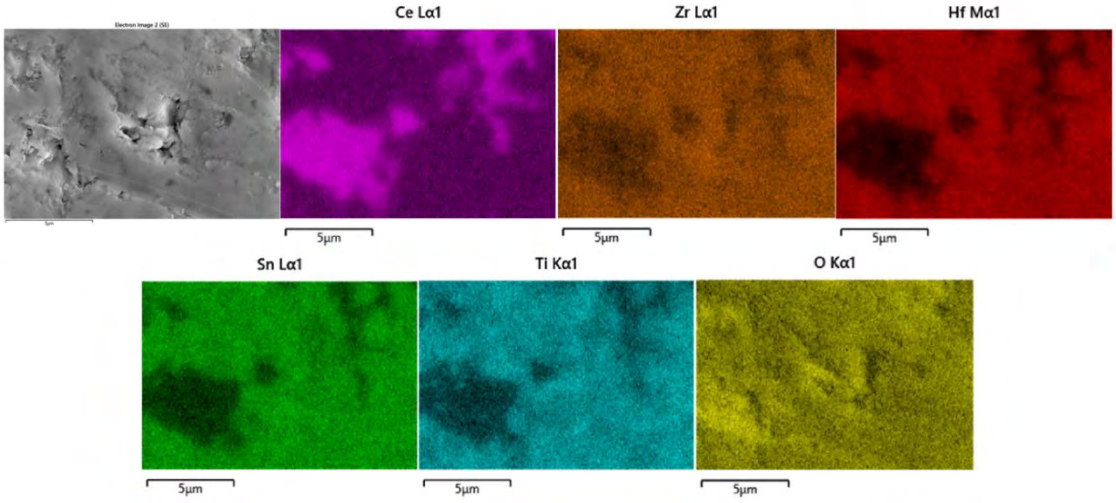

Figure 5.7. EDS mapping of multi-phase sample

Table 5.2. Atomic % of multi-phase sample from the EDS map.

	Hf	Ce	Sn	Zr	Ti	O
Atomic %	6.0	5.2	5.3	5.2	6.0	55.4

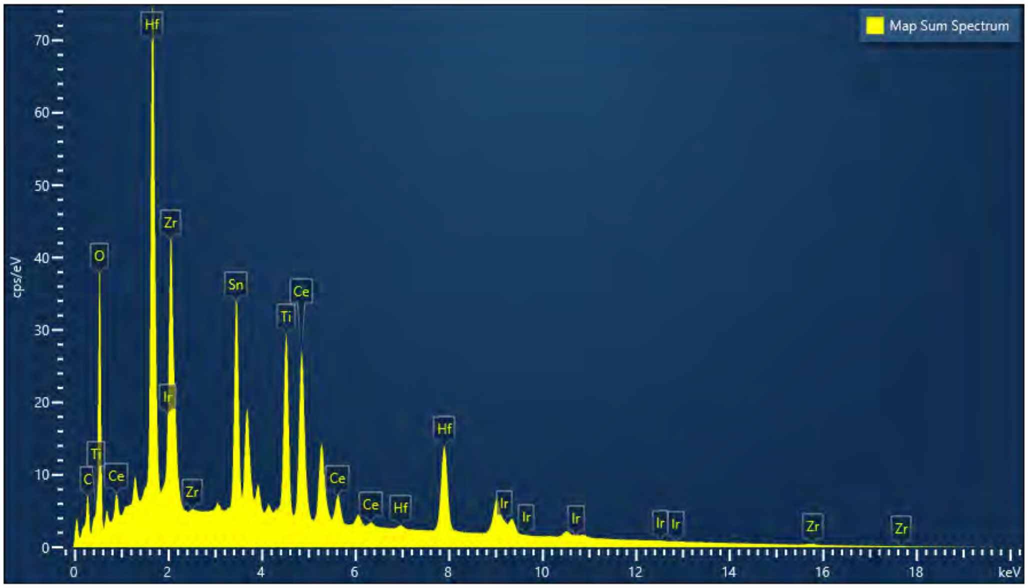

Figure 5.8. EDS spectrum of multi-phase sample. Note that Sn and Ti peaks can be clearly observed.

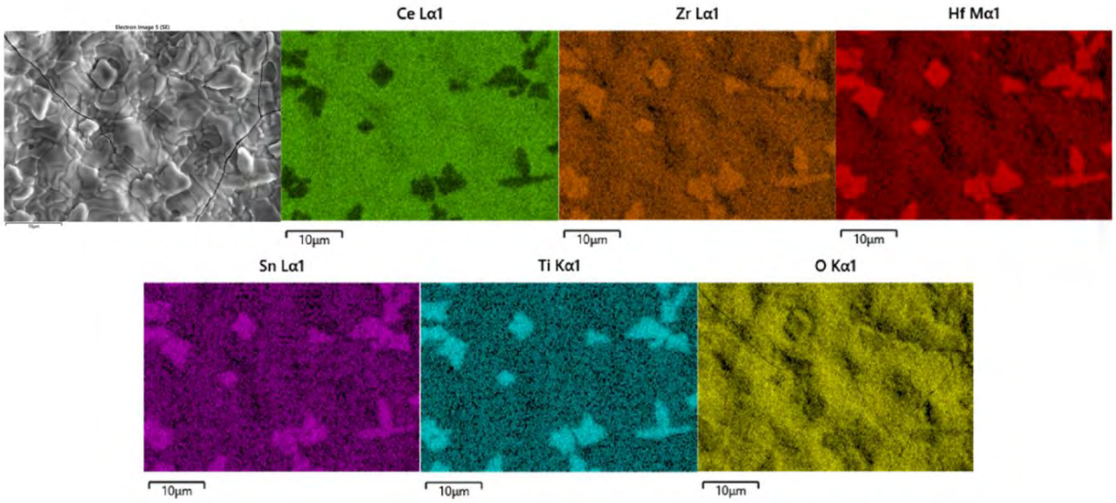

Figure 5.9. EDS mapping of predominantly single-phase sample.

Table 5.3. Atomic % of predominantly single-phase sample from EDS map spectrum.

	Hf	Ce	Sn	Zr	Ti	O
Atomic %	2.8	20.3	0.5	3.7	1.2	54.1

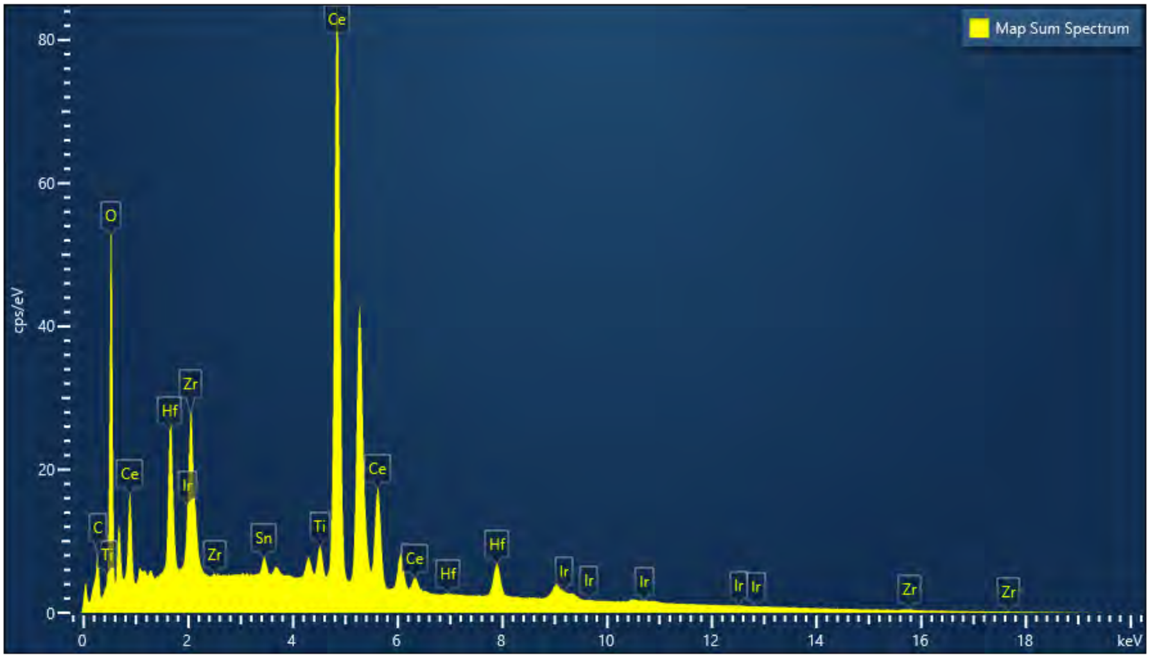

Figure 5.10. EDS map spectrum of predominantly single-phase sample. Note that relatively smaller signal of Sn and Ti, compared to that of the multi-phase target

5.3 References

[1] N. Zhang, H. Yokota, A.M. Glazer, Z. Ren, D.A. Keen, D.S. Keeble, P.A. Thomas, Z.G. Ye, The Missing Boundary in the Phase Diagram of $PbZr_{1-x}Ti_xO_3$, Nat. Commun., 5 (2014), Article 5231

[2] B. Noheda, D.E. Cox, G. Shirane, Phase Diagram of the Ferroelectric Relaxor (1-x)$PbMg_{1/3}Nb_{2/3}O_3$-x$PbTiO_3$, Phys. Rev. B, (2002), Article 054104

[3] D.E. Cox, B. Noheda, G. Shirane, Y. Uesu, K. Fujishiro, Y. Yamada, Universal Phase Diagram for High-Piezoelectric Perovskite Systems, Appl. Phys. Lett., 79 (2001), pp. 400–402

[4] O. Bouquin, M. Lejeune, J. P. Boilot, Formation of the Perovskite Phase in the $PbMg_{1/3}Nb_{2/3}O_3$─$PbTiO_3$ System, J. Am. Ceram. Soc., 74 (1991), pp. 1152–1156

[5] S.L. Swartz, T.R. Shrout, Fabrication of Perovskite Lead Magnesium Niobate, Mater. Res. Bull., 17 (1982), pp. 1245–1250

[6] J.L. Braun, C.M. Rost, M. Lim, A. Giri, D.H. Olson, G.N. Kotsonis, G. Stan, D.W. Brenner, J.P. Maria, P.E. Hopkins, Charge-induced Disorder Controls the Thermal Conductivity of Entropy-Stabilized Oxides, Adv. Mater., 30 (2018), Article 1805004

[7] T. Maiti, R. Banerjee, S. Chatterjee, M. Ranjan, T. Bhattacharya, S. Mukherjee, S.S. Jana, A. Dwivedi, High-Entropy Perovskites: An Emergent class of Oxide Thermoelectrics with Ultralow Thermal Conductivity, ACS Sustain. Chem. Eng., 8 (2020), pp. 17022-17032

[8] S. Pandya, J.D. Wilbur, B. Bhatia, A.R. Damodaran, C. Monachon, A. Dasgupta, W.P. King, C. Dames, L.W. Martin, Direct Measurement of Pyroelectric and Electrocaloric Effects in Thin Films, Phys. Rev. Appl., 7 (2017), Article 034025

[9] F. Li, S. Zhang, D. Damjanovic, L-Q. C, T. R. Shrout, Local Structural Heterogeneity and Electromechanical Responses of Ferroelectrics: Learning from Relaxor Ferroelectrics, Adc. Func. Mater., 27 (2018), Article 1801504

[10] D. Viehland, S. J. Jang, L. E. Cross, Freezing of the Polarization Fluctuation in Lead Magnesium Niobate Relaxors, J. Appl. Phys., 68 (1990), pp. 2916-2921

[11] A. A. Bokov, Z-G. Ye, Recent Progress in Relaxor Ferroelectrics with Perovskite Structure, J. Mater. Sci., 41 (2006), pp. 31-52

[12] Z. Xu, S. M. Gupta, D. Viehland, Direct Imaging of Atomic Ordering in Undoped and La-Doped $Pb(Mg_{1/3}Nb_{2/3})O_3$, J. Am. Ceram. Soc., 83 (2000), pp. 181-188

[13] M. J. Cabral, S. Zhang, E. C. Dickey, J. M. Lebeau, Gradient Chemical Order in the Relaxor $Pb(Mb_{1/3}Nb_{2/3})O_3$, Appl. Phys. Lett., 112 (2018), Article 082901

[14] A. D. Hilton, D. J. Barber, C. A. Randall, T. R Shrout, On Short Rnage Ordering in the Perovskite Lead Magnesium Niobate, J. Mater. Sci., 25 (1990), pp. 3461-3466

[15] A. Levstik, Z. Kutnjak, C. Filipic, R. Pirc, Glassy Freezing in Relaxor Ferroelectric Lead Magnesium Niobate, Phys. Rev. B., 57 (1998), Article 11204

[16] G. Williams, D.C. Watts, Non-Symmetrical Dielectric Relaxation Behavior Arising from a Simple Empirical Decay Function, Trans. Faraday Soc., 66 (1970), pp. 80-85

[17] M. Ozgul, E. Furman, S. Trolier-McKinstry, C.A. Randall, Polarization Relaxation Anisotropy in Pb($Zn_{1/3}Nb_{2/3}$)O_3-$PbTiO_3$ Single-Crystal Ferroelectric as a Function of Fatigue History, J. Appl. Phys. 95 (2004), pp. 2631-2638

[18] A.A. Bokov, Z.-G. Ye, Double Freezing of Dielectric Response in Relaxor Pb($Mg_{1/3}Nb_{2/3}$)O_3 crystals, Phys. Rev. B., 74 (2006), Article 132102

[19] J. Müller, T.S. Böscke, U. Schröder, S. Mueller, D. Bräuhaus, U. Böttger, L. Frey, T. Mikolajick, Ferroelectricity in Simple Binary ZrO_2 and HfO_2, Nano Lett., 12 (2012), pp. 4318–4323

[20] T.S. Böscke, J. Müller, D. Bräuhaus, U. Schröder, U. Böttger, Ferroelectricity in Hafnium Oxide Thin Films, Appl. Phys. Lett., 99 (2011), Article 102903

[21] Z. Teng, L. Zhu, Y. Tan, S. Zeng, Y. Xia, Y. Wang, H. Zhang, Synthesis and Structures of High-Entropy Pyrochlore Oxides, J. Eur. Ceram. Soc., 40 (2020), pp. 1639–1643

[22] J. Gild, M. Samiee, J.L. Braun, T. Harrington, H. Vega, P.E. Hopkins, K. Vecchio, J. Luo, High-Entropy Fluorite oxides, J. Eur. Ceram. Soc., 38 (2018), pp. 3578–3584

[23] S. Jiang, T. Hu, J. Gild, N. Zhou, J. Nie, M. Qin, T. Harrington, K. Vecchio, J. Luo, A New Class of High-Entropy Perovskite Oxides, Scr. Mater., 142 (2018), pp. 116–120

[24] K. Khan, A.K. Tareen, M. Iqbal, I. Hussain, A. Mahmood, U. Khan, M.F. Khan, H. Zhang, Z. Xie, Recent Advances in MXenes: A Future of Nanotechnologies, J. Mater. Chem. A. Mater., 11 (2023), pp. 19764–19811

[25] C.M. Rost, E. Sachet, T. Borman, A. Moballegh, E.C. Dickey, D. Hou, J.L. Jones, S. Curtarolo, J.P. Maria, Entropy-Stabilized Oxides, Nat. Commun., 6 (2015), Article 8485

[26] K. Chen, X. Pei, L. Tang, H. Cheng, Z. Li, C. Li, X. Zhang, L. An, A Five-Component Entropy-Stabilized Fluorite Oxide, J. Eur. Ceram. Soc., 38 (2018), pp. 4161–4164

[27] M. Park, T.E. Mitchell, A.H. Heuer, Subsolidus Equilibria in the TiO_2-SnO_2 System, J. Am. Ceram. Soc., 58 (1975), pp. 43–47

Appendix A

Schematics of Pulsed Laser Deposition Systems

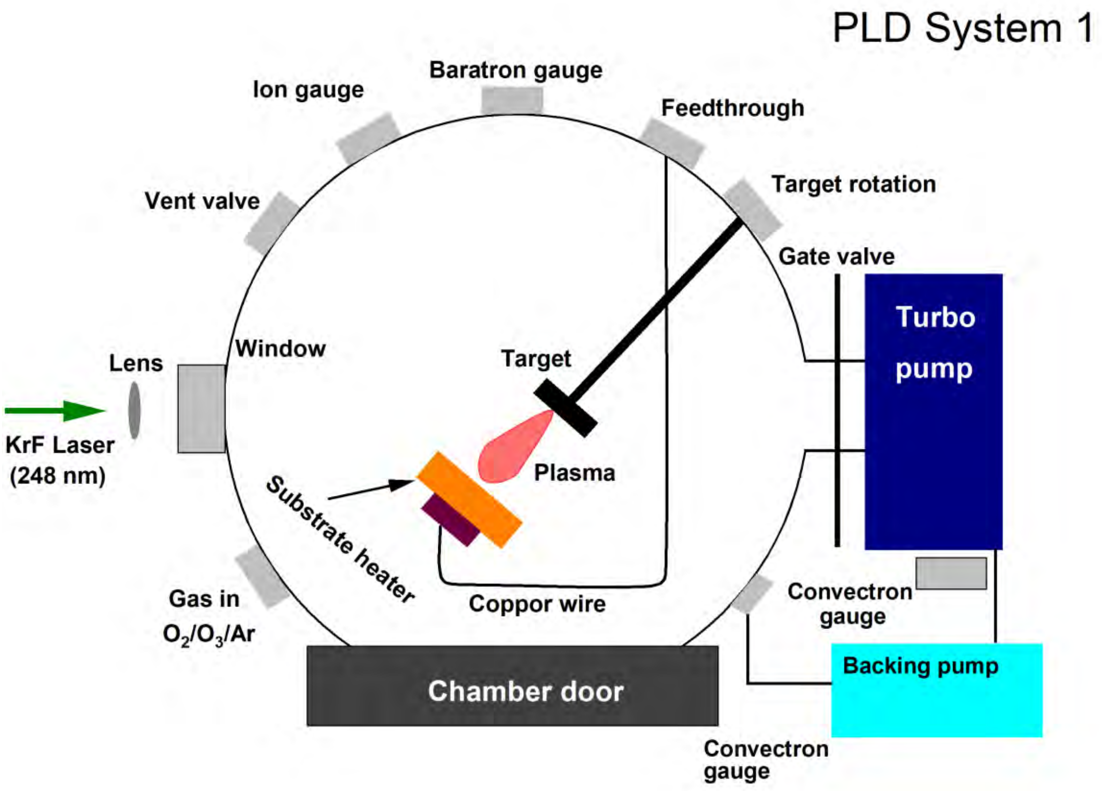

Figure A.1. Schematic of pulsed laser deposition system without load-lock chamber. Please note that this figure illustrates the system from a top-view.

Figure. A.1 depicts the original STM group pulsed laser deposition (PLD) system with no load-lock (LL) chamber. A 248 nm wavelength KrF excimer laser (Compex pro 102F, Coherent) is directed into the process chamber through a silica lens and chamber window (fused quartz laser port). The laser energy density can be adjusted either via changing the laser energy (maximum of 400 mJ) or changing the position of the lens. This system has single target system connected to rotary feedthrough for target rotation. A ceramic target can be mounted on stainless steel target holder. Substrate can be cured down on resistive heating stage (SU-200-HH, MeiVac) that can go up to 950°C. The heater is connected to power feedthrough by copper wire protected by ceramic blocks and the temperature can be controlled by external AC controller (SU-A750, VTAC) based on the sensing feedback from K-type thermocouple inserted underneath the heater. Base pressure of ~ 10^{-7} Torr can be achievable within 2 hours by virtue of turbo molecular pump (Shimadzu, TMP-1003 LM) backed by dry-scroll pump (Edward nXDS10i). Three different types of gas, oxygen, ozone, and argon, can be used. Gas flow can be controlled and monitored by MKS type 247 4 channel readout. Deposition pressure can be monitored by baratron capacitance manometer (MKS) and type 660 (MKS) display or by Pirani/capacitance diaphragm gauge (PCM301, Busy Bee). Deposition pressure can be controlled via manually controlling gate valve between process chamber and turbo pump. During deposition, turbo speed has to be lowered down to ~ 40% of normal operation speed due to too high pumping speed at normal speed (> 1000 liters/second). Upon completion of deposition, the gate valve is completely closed and power supply to heating stage is shut off. Oxygen vent valve is then manually opened and oxygen flow into process chamber allow reaching 100 Torr within 30 seconds, thus sample is cooled under high oxygen pressure to suppress volatility of Pb or any other volatile species. Temperature can be lowered below 400°C from 630°C within 1 min 30 seconds to minimize Pb volatilization.

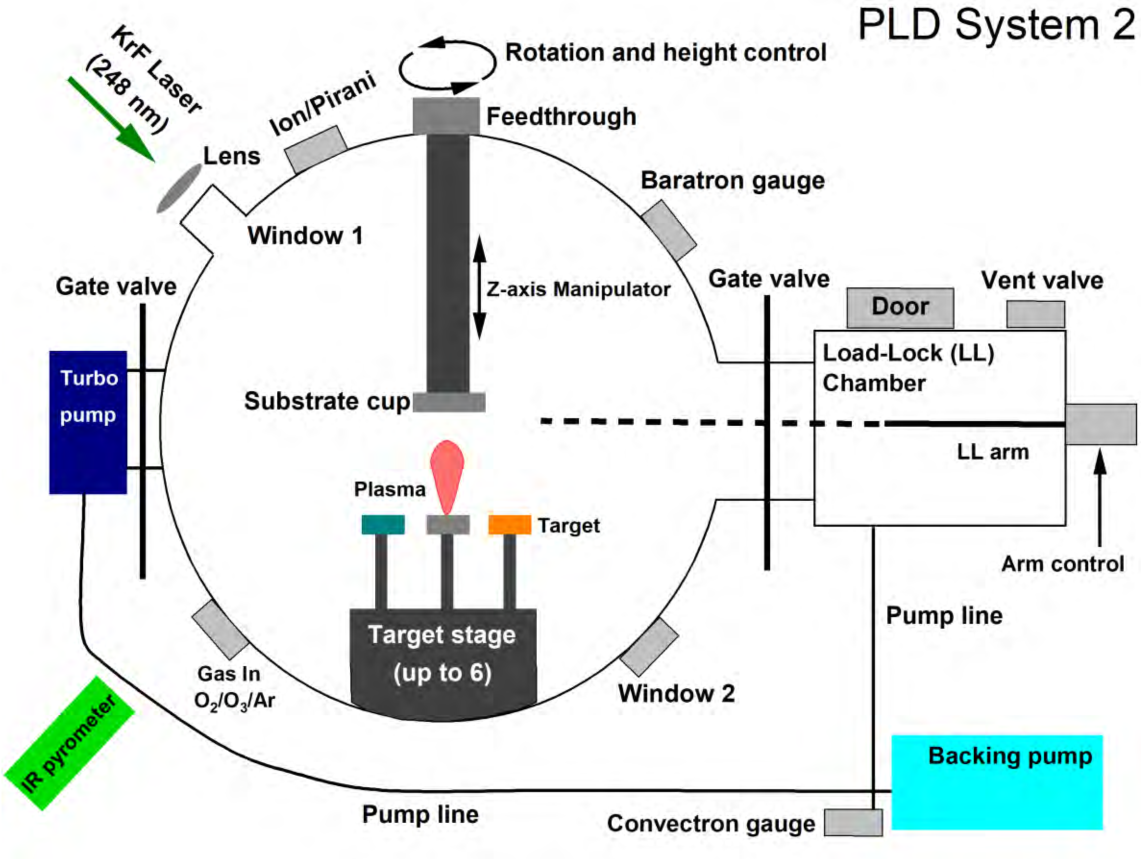

Figure A.2. Schematic of pulsed laser deposition system with a load-lock chamber. Please note that this figure illustrates the system from a side-view.

Figure. A.2 describes PLD system with the load lock chamber. This chamber is configured in a bottom target – substrate up configuration. Up to 6 targets can be installed in the target stage, so multilayers can be easily fabricated without breaking vacuum. The KrF excimer laser (Compex pro 120F, Coherent) is directed to the process chamber through a silica lens and the chamber window. The Z-axis manipulator is configured in an on-axis geometry. A resistive heating element is placed at the end of the manipulator and a K-type thermocouple is welded to the heating element. The maximum temperature is 950°C; both the temperature and the ramp rate are controllable using a temperature controller

(Eurotherm 3216) and a DC power supply (TDK lambda). The temperature readout monitors the temperature of the heating element, rather than the substrate.

The substrate can be mounted on the substrate carrier using silver paste (Sigma-Aldrich) and cured on a hotplate. After that, the substrate carrier can be mounted on a substrate cup and transferred using the load lock arm through the gate valve between the process chamber and the load lock chamber. It should be noted that due to the gap between the heating element and the substrate cup, the substrate temperature differs from the temperature readout on the temperature controller. For this reason, an infrared pyrometer (Fluke, Endurance series) placed outside of chamber is aimed at the substrate surface to assess the surface temperature. Based on the IR pyrometer, the maximum temperature achievable when the heating element temperature is set to 950°C is approximately 680°C. Approximately 25°C of temperature compensation has to be taken into account when reading the IR pyrometer due to the angle-dependence of the IR pyrometer. For example, an IR pyrometer temperature of 600°C approximately corresponds to 625°C of real temperature (substrate).

This chamber is equipped with turbo molecular pump (Agilent, TwisTorr 305 FS) backed by dry-scroll pump (Edwards XDS10). Approximately 20 hours are required to achieve a base pressure of 10^{-7} Torr from atmosphere pressure. Similar to PLD system 1, three different types of gases, oxygen, ozone, and argon, are available and the flow rate can be controlled via a mass flow controller (Omega engineering, FMA 5504A). The base pressure is monitored by an ion gauge (InstruTech, IGM-400). The deposition pressure is monitored using a baratron capacitance monometer and type 660 display (MKS) or by a Pirani/capacitance diaphragm gauge (PCM301, Busy Bee).

The deposition pressure can be controlled by manually closing the gate valve between the turbo pump and the process chamber. There is no need to lower the rotation speed of the turbo during deposition, unlike PLD system 1.

In order to cool the sample, when the deposition process is completed, the gate valve between process chamber and the load lock chamber is opened and the load lock arm is transferred into the process chamber. The substrate cup is removed from the manipulator using the load lock arm and transferred back to the load lock chamber. The load lock chamber then can be vented, usually with in-house nitrogen or air. This process can be completed within 90 seconds to minimize volatility of Pb or any other volatile species.

For target change or chamber cleaning, access to the process chamber can be made through the 8-inch view port. To vent the entire system, the gate valve between the load lock chamber and the process chamber is opened and the vent valve attached to the load lock chamber is opened before unscrewing the 8-inch view port.

Appendix B

Energy Storage Properties of $SrHfO_3$ Thin Film Capacitor

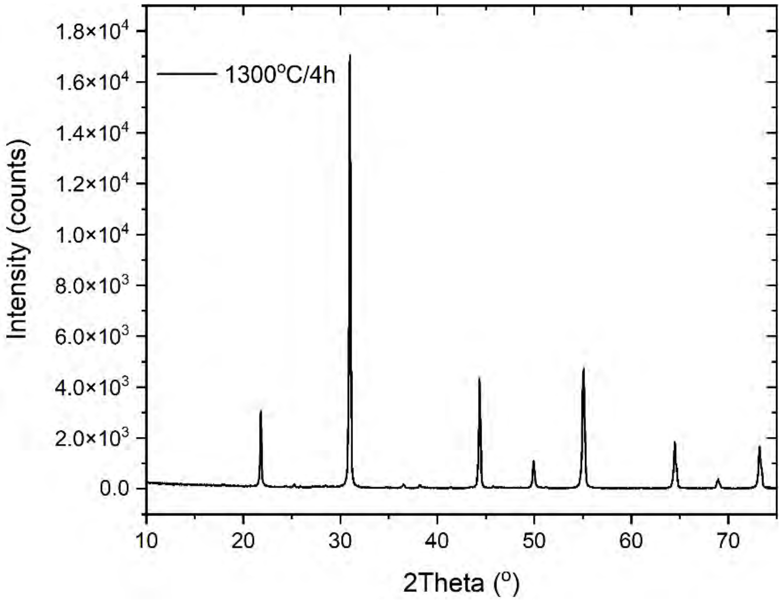

Figure B.1. X-ray diffraction of $SrHfO_3$ powder calcined at 1300°C for 4 hours

$SrHfO_3$ has recently garnered increasing attention as a next generation high *k* dielectric in electronics [1,2]. Low leakage current, large breakdown field strength, and a reasonable permittivity may trigger exploration of $SrHfO_3$ as a dielectric thin film for energy storage applications. The data below shows some preliminary work regarding structure, dielectric, ferroelectric, and energy storage properties of $SrHfO_3$ thin films.

To make an in-house $SrHfO_3$ PLD target, $SrCO_3$ (Sigma Aldrich, 99.9%) and HfO_2 (Sigma Aldrich, 98%) powders were ball milled with ethanol for 24 hours. After drying at 80°C in an oven, the powder was calcined at 1300°C for 4 hours. Figure B.1 shows X-ray diffraction (XRD) patterns of the $SrHfO_3$ powders; formation of the perovskite phase is exhibited. Calcined powder was then uniaxially pressed into a 1 inch diameter pellet, followed by cold isostatic pressing (CIP). The pressed pellet was sintered at 1650°C for 4 hours.

Deposition of $SrHfO_3$ thin film was carried out by pulsed laser deposition (PLD) using $SrRuO_3$ on $SrTiO_3$ substrates. For the growth of $SrHfO_3$ thin films, 1.5 J cm^{-2} laser energy, 4 Hz laser frequency, a deposition temperature of 630°C, and an oxygen deposition pressure of 50-85 mTorr were used. In Figure B.2, two different XRD patterns are revealed. $SrHfO_3$ film sample deposited under low deposition pressure (50 mTorr, black) promote better structural quality, compared to that of higher deposition pressures (85 mTorr, red). As seen in Figure B.2, the rocking curve for the film fabricated under low deposition pressure also exhibits better crystalline quality, presumably due to increased mobility of adatoms.

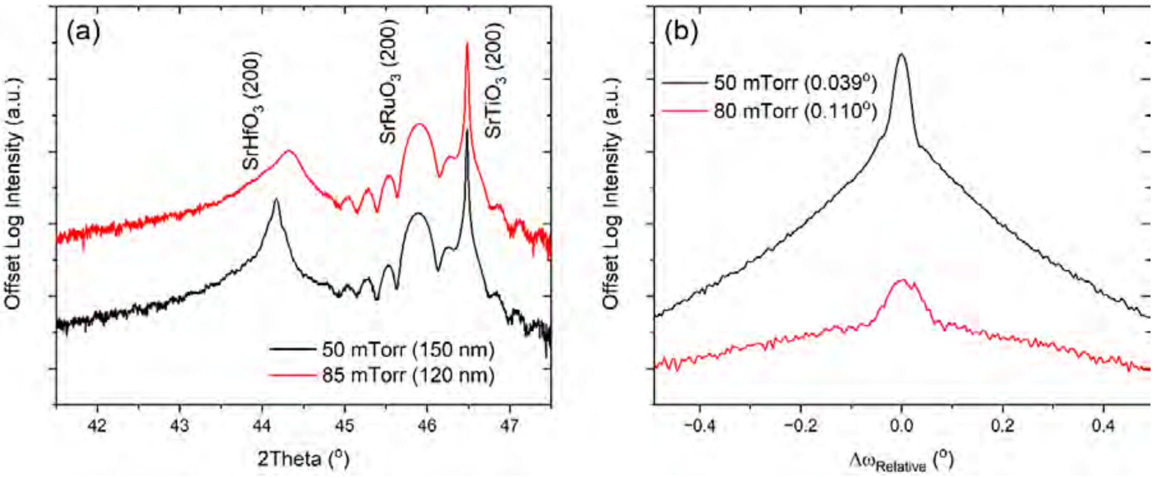

Figure B.2. (a) XRD of $SrHfO_3$ thin film deposited on $SrRuO_3$ (45nm)/$SrTiO_3$ substrate under two different deposition pressure and (b) corresponding rocking curve

The dielectric permittivity and loss tangent of the film grown at 50 mTorr is presented in Figure B.3(a). A relative dielectric permittivity of 25 with a loss tangent below 0.02 was measured at room temperature. The high loss tangent below 1 kHz is associated with space charge, probably due to non-stoichiometry in the film (possibly from the kinetic bombardment during PLD processing). The polarization-electric field loop (P-E loop) exhibits linear dielectric-like behavior (Figure B.3(b)). The voltage was driven from the bottom electrode and the electric field was varied from 500 kV cm^{-1} to 3000 kV cm^{-1}. The film broke down at applied electric fields of 3250 kV cm^{-1}. The energy storage properties were estimated from the P-E loops; the maximum recoverable energy storage density was 12.7 J cm^{-3}, with an efficiency of 93.3% for an applied electric field of 3000 kV cm^{-1}.

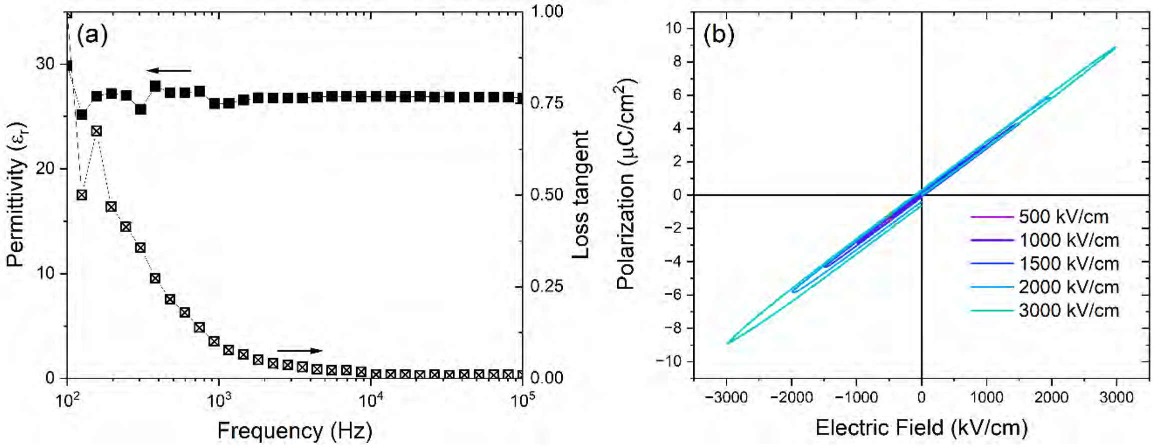

Figure B.3. (a) Dielectric permittivity and loss tangent of 50 mTorr-grown sample measured at room temperature. (b) Hysteresis loops measured at electric fields from 500 kV cm^{-1} to 3000 kV cm^{-1} and a frequency of 1 kHz.

Appendix C

Summary of Target Preparation

A conventional solid-state reaction process was utilized for powder processing. It is important to estimate the weight loss of volatile species, including lead oxide. To estimate the weight loss, the alumina crucible was pre-heated to 120°C to remove moisture. The powders were accurately weighed (1 g or less should be enough) and the pre-heated alumina crucible was used to transfer the powder into furnace. The furnace temperature was set at 500°C for 30 min. Before the furnace cooled to 100°C, the powder was removed from the alumina crucible and weighed again to calculate the weight loss.

For milling, yttria-stabilized zirconia balls were used as milling media. Milling was typically done in ethanol using the desired powder composition in plastic bottles. After ball milling for 24 hours, the slurry was then dried at 80°C.

The dried powder was then calcined at the desired temperature. The ramp rate during calcination was 10℃ per min. Excess lead oxide powder (or any other volatile elements) was added after the calcination and the powder was ball-milled again with ethanol for 24 hours. The powder was then dried as described above.

All pellets were uniaxially pressed (Carver) using a 1 inch diameter stainless steel die (PPDS, USA). The uniaxially pressed green body was vacuum sealed using a latex glove before Cold Isostatic Pressing (CIP) for 1 min at 207 MPa.

For sintering, a powder bed (of same composition) was placed under the pressed green body to prevent strong adhesion to the alumina crucible. The ramp rate during sintering was 10℃ per min. All targets were mechanically polished after sintering. All targets used are summarized in the table below.

	Pre-calcination	Calcination	Pressing method	Sintering	Note
Al_P	Yes (1300°C/4 h)	800°C/4 h	Uniaxial (44 MPa) and CIP (207 MPa)	1050°C/2 h	20 % excess Pb, no single phase
Fe_P	Yes (1300°C/4 h)	800°C/4 h	Uniaxial (44 MPa) and CIP (207 MPa)	950°C/2 h	20 % excess Pb
Sc_P	Yes (1300°C/4 h)	800°C/4 h	Uniaxial (44 MPa) and CIP (207 MPa)	950°C/2 h	20 % excess Pb
Cr_P	Yes (1300°C/4 h)	800°C/4 h	Uniaxial (44 MPa) and CIP (207 MPa)	1150°C/2 h	20 % excess Pb, no single phase
Mn_P	Yes (1300°C/4 h)	800°C/4 h	Uniaxial (44 MPa) and CIP (207 MPa)	950°C/2 h	20 % excess Pb
Na_P	No	1200°C/4 h	Uniaxial (44 MPa) and CIP (207 MPa)	1400°C/2 h	1 % excess Bi and Na
K_P	No	1200°C/4 h	Uniaxial (44 MPa) and CIP (207 MPa)	1400°C/2 h	1 % excess Bi and K
Pb_P	No	1050°C/4 h	Uniaxial (44 MPa) and CIP (207 MPa)	1350°C/2 h	1 % excess Bi and 20 % Pb
HEF	No	1300°C/6 h	Uniaxial (44 MPa) and CIP (207 MPa)	1500°C/6 h	See future work
$(HfZrCe)_{1/3}O_2$	No	1300°C/6 h	Uniaxial (44 MPa) and CIP (207 MPa)	1650°C/6 h	

References

[1] M.D. McDaniel, C. Hu, S. Lu, T.Q. Ngo, A. Posadas, A. Jiang, D.J. Smith, E.T. Yu, A.A. Demkov, J.G. Ekerdt, Atomic Layer Deposition of Crystalline $SrHfO_3$ Directly on Ge (001) for High-k Dielectric Applications, J. Appl. Phys., 117 (2015), Article 054101

[2] J. Kim, D. Song, H. Yun, J. Lee, J.H. Kim, J.H. Kim, B. Kim, K. Char, Low Leakage in High-k Perovskite Gate Oxide $SrHfO_3$, Adv. Electron. Mater., 9 (2023), Article 2201341.

VITA

Yeongwoo Son

Yeongwoo Son was born and raised in Busan, South Korea. Prior to begin his doctoral degree at the Pennsylvania State University, he earned a B.E degree at Pukyong National University in Metallurgical Engineering in 2016. He attended the University of Florida in 2017 for a research internship, before he moved to State College in August 2018 for graduate study. In January 2021, he joined Prof. Susan Trolier-McKinstry's research group for his doctoral degree.